ESPOO 2004 VTT PUBLICATIONS 529

Janne K. Aikio

Extremely short external cavity (ESEC) laser devices

Wavelength tuning and related optical characteristics

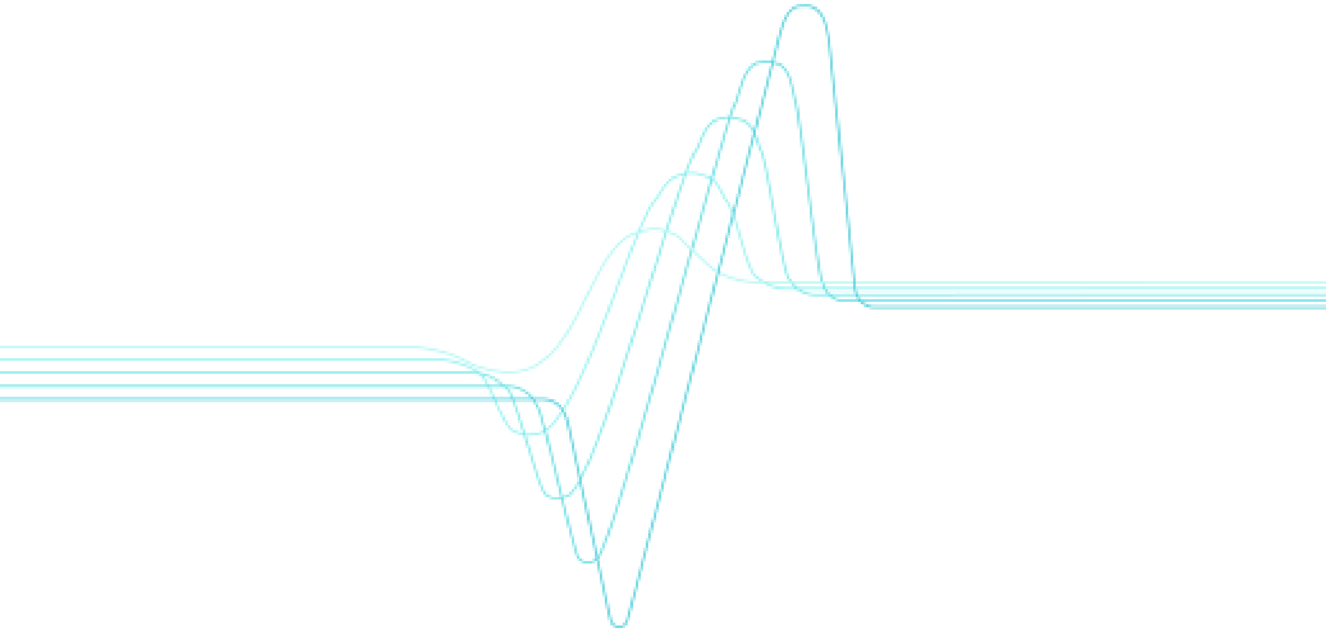

VTT PUBLICATIONS 529

Extremely short external cavity (ESEC) laser devices

Wavelength tuning and related optical characteristics

Janne K. Aikio

VTT Electronics

Academic Dissertation to be presented with the assent of the Faculty of Science, University of Oulu, for public discussion in the Auditorium L10, Linnanmaa, on June 18th, 2004, at 12 o´clock noon.

ISBN 951–38–6377–8 (soft back ed.)
ISSN 1235–0621 (soft back ed.)

ISBN 951–38–6378–6 (URL: http://www.vtt.fi/inf/pdf/)
ISSN 1455–0849 (URL: http://www.vtt.fi/inf/pdf/)

JULKAISIJA – UTGIVARE – PUBLISHER

VTT, Vuorimiehentie 5, PL 2000, 02044 VTT
puh. vaihde (09) 4561, faksi (09) 456 4374

VTT, Bergsmansvägen 5, PB 2000, 02044 VTT
tel. växel (09) 4561, fax (09) 456 4374

VTT Technical Research Centre of Finland, Vuorimiehentie 5, P.O.Box 2000, FIN–02044 VTT, Finland
phone internat. + 358 9 4561, fax + 358 9 456 4374

VTT Elektroniikka, Kaitoväylä 1, PL 1100, 90571 OULU
puh. vaihde (08) 551 2111, faksi (08) 551 2320

VTT Elektronik, Kaitoväylä 1, PB 1100, 90571 ULEÅBORG
tel. växel (08) 551 2111, fax (08) 551 2320

VTT Electronics, Kaitoväylä 1, P.O.Box 1100, FIN–90571 OULU, Finland
phone internat. + 358 8 551 2111, fax + 358 8 551 2320

Technical editing Leena Ukskoski

Otamedia Oy, Espoo 2004

Aikio, Janne K. Extremely short external cavity (ESEC) laser devices. Wavelength tuning and related optical characteristics. Espoo 2004. VTT Publications 529. 162 p.

Keywords external cavity lasers, effective reflectance, semiconductor lasers

Abstract

In this work, we have developed ways to model and use extremely short external cavity (ESEC) semiconductor lasers. We have used modeling and experiments to analyze the wavelength tuning and other related optical characteristics of various ESEC laser devices. A brief overview is given on the physics related to semiconductor lasers. A simple phenomenological laser model is presented for the efficient calculation of the multi-mode output spectrum of a Fabry–Perot semiconductor laser. The effective reflectance model is used to simulate the influence of the ESEC on the laser operation. Several ways to calculate the effective reflectance from various kinds of ESEC structures are presented, including the Gaussian beam method, Fourier optics methods, and finite-difference time-domain (FDTD) method. We give an overview of the ESEC laser devices. The wavelength tuning and optical power characteristics of the planar-mirror (PM) ESEC laser are analyzed and compared to the measurements. The wavelength tuning of a laser using a micromachined tunable Fabry–Perot etalon in the ESEC configuration is analyzed. A method of wavelength tuning profilometry in the ESEC laser configuration is introduced, and the proof-of-principle experiments are presented and analyzed. The direct semiconductor laser readout systems for optical data storage are analyzed via modeling. Various types of playback signals are constructed, and a wavelength tuning enhanced readout method is introduced. The performance of a conventional Fabry–Perot laser and a very small aperture laser (VSAL) in the direct semiconductor laser readout system are modeled and compared using the novel FDTD laser-end model.

Preface

The work presented in this thesis was carried out in the Technical Research Center of Finland, VTT Electronics, and in the Optical Sciences Center, University of Arizona, during the years 1998–2004.

My greatest thanks to Dr. Pentti Karioja (VTT) and Prof. Dennis Howe (Optical Sciences Center, University of Arizona) who introduced me to this interesting research field and continuously guided, supported, advised and encouraged me during the course of this research. Great thanks also to my supervisors Prof. Harri Kopola (VTT), Prof. Rauno Anttila (Department of Physical Sciences, University of Oulu) and Prof. Seppo Alanko (VTT and Department of Physical Sciences, University of Oulu) for their encouragement and support in the various phases of the work.

I greatly acknowledge the financial support that has enabled this research. The largest part of the work was done in the research program Optical Technologies for Wireless Communications (OTECO), funded by the Technology Development Center of Finland (Tekes), VTT, and Finnish industry. The thesis was finalized within the VTT Key Technology Action: Micro and Nanotechnologies 2003–2004 (MINARES). I would like to warmly thank all that funding and all the people involved in these projects. In addition, the Graduate School of Modern Optics and Photonics (Prof. Timo Jääskeläinen) is greatly acknowledged for financing and supporting my post-graduate studies.

I wish to express my gratitude to my co-researchers that have contributed to this work: Mr. K. Kataja, Mr. J. Olkkonen, Mr. V. Heikkinen, Mr. A.-J. Mattila, Mr. T. Alajoki, Mr. J. Hiltunen, Mr. J. Ollila, Dr. M. Blomberg, Mr. P. Weetman, Prof. M. Wartak, and Dr. Y. Sidorin. I would also thank all the staff and co-workers in VTT Electronics and the Optical Sciences Center, University of Arizona, who have helped me in my work in dozens of ways.

I would like to thank my friends and family for being there; special thanks to my brother and co-worker Mauri for your support and encouragement, and to my parents-in-law, Mauri and Anne, for taking care of my loved ones during the writing process. Finally, I wish to express my greatest love and gratitude to my wife Sanna and my little daughter Aino.

Oulu, April 2004

Janne Aikio

Contents

Lists of symbols and abbreviations

List of symbols

$A(\mathbf{r})$	Amplitude of the vector potential
A, B	Einstein's coefficients
a, b, c, A	Coefficients for the ellipse and corresponding vector $A = [a\ b\ c]^{\mathrm{T}}$
A, C	Coefficients for nonradiative recombination model
A, D	Constant parameters for the simple effective reflectivity models
A_i	Sub-areas of the path of the data mark
$a_{x,y}, b_{x,y}$	Parameters in the definition of Gaussian coupling coefficient
B, D	Coefficient for the spontaneous emission model
C	Coupling coefficient
c	Speed of light in vacuum
C_{BG}	Coupling coefficient from the background area of the optical disk
C_G	Gaussian coupling coefficient
C_I	Coupling coefficient of the incident field
C_{mark}	Coupling coefficient from the mark area of the optical disk
C_r	Coupling coefficient of the reflected field
D, B	Aid matrices for determining r_{eff} from FDTD calculations
E	Electric field distribution
E	Energy
$\hat{E}$	Fourier transform of an electric field distribution
e	Napier's number
$\mathbf{e}$	Unit polarization vector
E^*	Complex conjugate of an electric field distribution
E'	Propagated electric field distribution
E_{21}	Energy of a resonant photon
E_c	Energy of the electrons in the conduction band
E_{ext}	Field distribution of the externally reflected field
E_f	Fermi energy, Fermi level
E_g	Energy gap between conduction and valence bands
E_g	Transversal field distribution of the waveguide mode
E_R	Field distribution of the reflected field
E_v	Energy of the holes in the valence band
E_x, E_y, E_z	Electric field components

F	Envelope function of electronic state
F	Filtering function
$\mathbf{F}$	Fourier transform operator
$f(z_{EC})$	Functional dependence of the coupling amplitude
f_1, f_2	Occupation probabilities
f_x, f_y	Spatial frequency in x and y directions
g	Material gain
g_0	Fitting parameter in gain model
g_m	Material gain of longitudinal mode m
g_{max}	Maximal material gain
g_{peak}	The peak gain in gain model
h	Planck's constant
$\hbar$	Reduced Planck's constant ($\hbar = h/2\pi$)
H'	Perturbation part of the Hamiltonian operator
H'_{21}	Perturbation matrix element
H_x, H_y, H_z	Magnetic field components
I	Injection current
I_{th}	Threshold current
k	Momentum
K	Normalizing factor for the field distribution of the waveguide mode
K_B	Boltzmann's constant
l	FP etalon length
L	Length of the internal laser cavity
M	Modulation
m	Order of a longitudinal mode
M	Order of external cavity mode
M	Summation index
$\|M\|^2$	Momentum matrix element
$\|M_T\|^2$	Transition matrix element
m^*	Effective mass
m_0	Free electron mass
m_c	Effective mass in the conduction band
m_r^*	Reduced mass
m_v	Effective mass in the valence band
N	Number density of carriers
n	Refractive index
n_g	Group index

N_{ph}	Number density of photons
$N_{ph,\mathrm{m}}$	Number density of photons in mode m
N_{th}	Threshold carrier density
N_{tr}, N_s	Fitting parameters in gain model
$\boldsymbol{p}$	Momentum operator
P	Number density of holes
p	Order of the principal lasing mode
P_a	Absorbed optical power
$P_{b,m}$, $P_{f,m}$	Optical power from the back and front facets for mode m
P_I	Optical power incident on the internal laser facet
P_m	Optical power on longitudinal mode m
P_R	Reflected optical power
P_s	Scattered optical power
P_t	Transmitted optical power
P_{tot}	Total optical output power
q	Unit charge
$\boldsymbol{r}$	Position vector
r	Reflectivity or reflectance (of electric field amplitude)
R	Intensity reflectivity (intensity reflectance)
$R'_{sp,m}$	Spontaneous emission rate into mode m
R_{ABS}	Absorption rate
$r_{b/f}$	Ratio of optical powers from the back and front facets
r_{BG}	Reflectivity of the background area of the optical disk
r_{eff}	Effective reflectance
R_{er}	Intensity reflectivity of external reflector
r_{er}	Reflectivity of the external reflector
r_{ext}	External reflectance
R_f, R_b	Intensity reflectivities of the front and back facets
$r_{f,m}$, $r_{b,m}$	Amplitude reflectivities of the front and back facets for mode m
R_{FP}	Intensity reflectivity of the FP mirrors
r_{FP}	Reflectivity of the mirrors of the FP etalon
R_{int}	Internal (laser facet) intensity reflectivity
r_{int}	Internal (laser facet) reflectivity
R_{loss}	Photon loss rate
$R_{loss,m}$	Photon loss rate for mode m
r_m	Ratio of peaks and valleys for mode m
r_{mark}	Reflectivity of the mark area of the optical disk

R_{nr}	Non-radiative recombination rate
R_{ph}	Photon emission rate
R_{pump}	Pump rate
R_R	Recombination rate
R_r	Transition rate
R_{rad}	Radiative recombination rate
R_{SP}	Spontaneous emission rate
R_{ST}	Stimulated emission rate
$R_{st,m}$	Stimulated emission rate for mode m
R_x	Wavefront radius of a Gaussian beam on x direction
T	Length of the time-frame in modulation coding
T	Propagation transfer function
t	Time
t_{int}	Internal (laser facet) transmittivity
u	Bloch function of electronic state
V	Volume of the active laser cavity
v_g	Group velocity
V_m	Optical power of valley next to mode m
X	Matrix containing the squared values of x_n and y_n
x, y, z	Coordinate for lateral, transversal and longitudinal directions
X^+	Pseudo inverse (Moore–Penrose inverse) of matrix X
x_n, y_n	Real and imaginary parts of coupling coeff. sampled in the FDTD grid
z_0	Parameter related to Gaussian beams
z_0	Reference plane (x, y, z_0) for the effective reflectivity
z_{EC}	External cavity length
Δ	'Delta term', the difference between gain and loss for mode p
Δg_m	Gain difference to principal lasing mode for mode m
$\Delta g_{m,max}$	Gain difference to peak gain for mode m
Δz	Pixel pitch in FDTD simulations
$\Delta \alpha_m$	Loss difference to principal lasing mode for mode m
$\Delta \lambda$	Wavelength tuning range
$\Delta \lambda_g$	Width of the gain band in wavelengths
Γ_m	Confinement factor of photons in mode m
Ψ_c, Ψ_v	Wave functions of electronic states in cond. and val. bands
α_I	Internal loss term
α_m	Loss term for mode m
$\alpha_{M,m}$	Mirror loss term for mode m

$\delta(,)$	Delta-function
ε_0	Dielectric constant
$\phi_{b,m}$, $\phi_{f,m}$	Phase of the back and front facet reflectivity for mode m
ϕ_{eff}	Phase of the effective reflectance
η_x	Additional Gaussian phase
η_I	Internal quantum efficiency
λ	Wavelength
$\lambda_{EC,M}$	Wavelength of external cavity mode M
λ_f	Wavelength of the free-running laser
λ_m	Wavelength of longitudinal mode m
λ_p	Wavelength of the principal lasing mode, principal lasing wavelength
ν_{21}	Photon frequency
ρ	Density of states
ρ_c, ρ_v	Density of states for conduction and valence bands
ρ_r	Reduced density of states
ω	Angular frequency of photon
ω_x, ω_y	Beam width of Gaussian beam in x and y directions
ω_{x0}, ω_{y0}	Beam width of Gaussian beam on beam waist in x and y directions

List of abbreviations

ABC	Absorbing boundary condition
AR	Anti-reflection (coating)
ASE	Amplified spontaneous emission
CAD	Central aperture detection
CD	Compact disk
DSLR	Direct semiconductor laser readout
EC	External cavity
EM	Electromagnetic
ER	External reflector
ESEC	Extremely short external cavity
FDTD	Finite-difference time-domain method
FP, FPI	Fabry-Perot (etalon)
µFP	Micromachined Fabry–Perot etalon
FWHM	Full width half maximum
HR	High-reflection (coating)
LASER	Light amplification by stimulated emission radiation

LD	Laser diode
LEC	Long external cavity
LTCC	Low-temperature co-fired ceramics
PC	Phase change
PM	Planar mirror
PML	Perfect matched layer
QW	Quantum well
RSD	Rectified split detection
SEC	Short external cavity
TE	Transverse electric field
TM	Transverse magnetic field
VCSEL	Vertical cavity surface emitting laser
VSAL	Very small aperture laser
WTER	Wavelength tuning enhanced readout

1. Introduction

Almost as soon as the semiconductor lasers were invented in the 1960's, it was noted that the laser operation was sensitive to the external reflections that couple light back into the laser cavity. This was mostly considered to impair the laser operation. Very quickly, however, scientists learned to use the optical feedback in controlling the lasers [1, 2]. This was the beginning of the genre of *external cavity* (EC) semiconductor lasers.

After that EC lasers have been recognized as a distinct type of semiconductor lasers. Thousands of scientific papers have been written on them over the years, a large number of patents have been applied, and the EC lasers have been used in various commercial products. The applications range from chaotic laser sources to highly stabilized wavelength tunable lasers and from delicate scientific instruments to various kinds of sensors and devices, robust enough to be used in mass-manufactured industrial products.

As the understanding of semiconductor laser physics evolved, the methods for modeling the operation of the EC laser were developed. The effective reflectance model was adopted to include the influence of the EC on the laser models [3, 4]. Dynamical models were built to study and explain the delayed feedback effects and the relaxation oscillations of the EC laser [5]. Various regimes of the EC laser operation related to the external cavity length and the strength of the feedback were found [6] and several applications were developed for the EC lasers.

In this work, we will concentrate on one of the operational regimes, the *extremely short external cavity* (ESEC) semiconductor lasers. The ESEC laser can be defined as an EC laser whose external cavity length is less than about 100 μm. The most characteristic feature of the ESEC lasers compared to the other EC lasers is the importance of the diffraction and interference effects in the ESEC in the prediction of the laser's behavior. For conventional, longer EC lasers, it is relatively easy to describe the influence of the EC on the laser operation using some simplified approximations of strength and phase of the optical feedback. However, in many of the applications of ESEC lasers, the diffraction effects and the coupling efficiency back into the laser waveguide play major roles. A large part of the work shown in this thesis concentrates on the use of diffraction calculations to predict the effective reflectivity of the ESEC.

In this thesis, we have used the combination of a phenomenological semiconductor laser model and various effective reflectance models to predict the operational optical characteristics of ESEC lasers. We have developed novel ways to model various kinds of ESEC structures. Experimental work has been done to verify the results. The purpose of all this work has been to analyze and enhance the performance of the devices based on the ESEC lasers.

1.1 Organization of the thesis

The bulk of the thesis is divided into three parts: the ‘background’ part in Section 2, the ‘ESEC laser modeling’ part in Section 3 and the ‘ESEC laser devices’ part in Section 4. In Section 2, we will give some background information on the operation and realization of semiconductor lasers. We will also briefly review the use of the external cavity lasers. Especially, we describe the basic theory and measurements of semiconductor gain spectrum, which is an important part of the modeling of the operation of the ESEC semiconductor lasers, but which will not be re-considered in the rest of the work.

Section 3 describes the models that we use for the modeling of the ESEC laser operation. We present the phenomenological laser model customized for an efficient calculation of the multi mode spectrum of a semiconductor laser. We describe the effective reflectance model used to include the ESEC in the laser model and review the various ways to calculate the effective reflectance. To our knowledge, some methods presented here have been described for the first time in this context.

Section 4 presents the analysis of some devices based on the ESEC laser technology. The basic idea and possibilities of ESEC laser sensors and other devices is described. The planar-mirror ESEC laser is deeply analyzed. This analysis gives a solid basis for the understanding of the operation of the other devices based on ESEC lasers. Wavelength tuning of a semiconductor laser with an external micromachined Fabry–Perot etalon is described and the tuning range is analyzed. A method of wavelength tuning profilometry is described and the experimental results have been analyzed via modeling. The direct semiconductor laser readout for optical data storage is modeled. Several enhancements for the system are proposed, including the wavelength tuning enhanced readout and various types of playback signals. The operation of a conventional edge-emitting

Fabry–Perot laser and a very small aperture laser in the direct semiconductor laser readout systems is compared using a combined FDTD and laser model. Section 5 is the summary of the work done in this thesis.

1.2 Author's contribution

The contribution of the author includes the development and programming of the phenomenological laser model and the various ways to calculate the effective reflectance. Also, the analysis and the measurements of the various ESEC laser devices were mainly done by the author. ***Mr. V. Heikkinen*** has done the experiments and the prototype building for the tunable laser in Section 4.3 together with ***Mr. K. Keränen, Mr. J. Ollila, Mr. J. Hiltunen***, ***Mr. T. Alajoki***, the author, and several other people in VTT. ***Mr. A.-J. Mattila***, ***Mr. P. Weetman*** and ***Prof. M. Wartak*** have helped the author in the modeling of the tunable laser and in the understanding of the physics related to the semiconductor laser gain. ***Mr. K. Kataja*** has done the FDTD simulations and FDTD code development for Sections 3.3.5.1 and 4.5.2.2 together with the author, ***Mrs. S. Aikio***, ***Mr. J. Olkkonen*** and several people in the University of Arizona. ***Prof. D. Howe*** and ***Dr. P. Karioja*** have coordinated the work and guided the author in the process.

In the course of the work, the author has contributed to the following publications that are also mentioned in the reference listing:

1. Aikio, J. K., Kataja, K. J., Alajoki, T., Karioja, P., Howe, D. G. Extremely short external cavity lasers: The use of wavelength tuning effects in near field sensing. Proceedings of SPIE – The International Society for Optical Engineering, v. 4640. 2002. Pp. 235–245. (Ref [7]).

2. Aikio, J. K., Kataja, K. J., Olkkonen, J., Howe, D. G. Two dimensional FDTD modeling of direct semiconductor laser read/write systems. Proceedings of SPIE – The International Society for Optical Engineering, v. 4647. 2002. Pp. 43–51. (Ref. [8]).

3. Aikio, J., Howe, D. Extremely short external cavity semiconductor laser: Profilometry via wavelength tuning. Conference on Lasers and Electro-Optics Europe – Technical Digest. 2001. Pp. 484–485. (Ref. [9]).

4. Aikio, J., Howe, D. G. Direct semiconductor laser readout in optical data storage. Proceedings of SPIE – The International Society for Optical Engineering, v. 4090. 2000. Pp. 56–65. (Ref. [10]).

5. Aikio, J., Karioja, P. Wavelength tuning of a laser diode by using a micromechanical Fabry–Perot interferometer. IEEE Photonics Technology Letters, v. 11. 1999. Pp. 1220–1222. (Ref. [11]).

6. Aikio, J., Sidorin, Y., Blomberg, M., Karioja, P. Wavelength tunable hybrid laser diode realized by using an electrostatically tuned silicon micromachined Fabry–Perot interferometer. Proceedings of SPIE – The International Society for Optical Engineering, v. 3625. 1999. Pp. 588–597. (Ref. [12]).

7. Aikio, J. K., Kataja, K. J., Howe, D. G. Extremely short external cavity lasers: Direct semiconductor laser readout modeling by using finite difference time domain calculations. Proceedings of SPIE – The International Society for Optical Engineering, v. 4595. 2001. Pp. 163–173. (Ref. [13]).

8. Heikkinen, V., Aikio, J., Alajoki, T., Hiltunen, J., Mattila, A.-J., Ollila, J., Karioja, P. Single-mode tuning of a 1540-nm diode laser using a Fabry–Perot interferometer. IEEE Photonics Technology Letters, Accepted for publication. 2004. (Ref. [14]).

9. Kataja, K., Aikio, J., Howe, D. G. Numerical study of near-field writing on a phase-change optical disk, Applied optics, v. 41. 2002. Pp. 4181–4187. (Ref. [15]).

10. Wartak, M. S., Weetman, P., Alajoki, T., Aikio, J., Heikkinen, V. Extraction of rate-equation parameters from optical modal gain measurements for multiple-quantum-well semiconductor lasers. Microwave and Optical Technology Letters, v. 35. 2002. Pp. 55–56. (Ref. [16]).

2. External cavity lasers overview

Before picking up our main subject, *extremely short external cavity* (ESEC) lasers, we will briefly go through the basics of the semiconductor lasers and the EC lasers. We will describe the semiconductor laser operation itself in Section 2.1. The laser operation in general is described in Section 2.1.1. The physics related to the gain properties of the semiconductor laser are briefly described in 2.1.2 and a typical semiconductor laser cavity structure is described in 2.1.3. After that, in Section 2.2, we take a short look at EC lasers.

2.1 Semiconductor lasers

The word 'laser' was originally an abbreviation for light amplification by stimulated emission radiation (LASER), which is a certain technique for producing coherent light. The first LASER devices were built in the late 1950’s. Later on, 'laser' has become a word in general language meaning devices in which the LASER technique is used, or sometimes meaning the coherent beam of light produced by this technique. The verb 'to lase' has been adopted to describe the operation of LASER.

The purpose of this Section is to describe what makes the semiconductor lasers lase. We will first give a short introduction to the laser operation in general, and then look at the specifics of the operation of the semiconductor lasers. The theory presented here can be found from several sources in literature. In Section 2.1, (unless otherwise specified) references [17, 18] and [19] have been mainly used.

2.1.1 Laser operation

The LASER operation requires a material with at least two electronic energy levels with an energy gap in the order of 1 eV, corresponding to the energies of photons in the optical region. The lifetime of the upper level should be relatively long to enable the *population inversion*. The population inversion means that the electronic states are more populated in the upper energy level than in the lower level. The population inversion can be achieved by optical excitation via a third, higher energy level, or by direct pumping of electrons to the upper energy level, while simultaneously pumping electrons away from the lower level. The population inversion enables the material to emit more photons via stimulated emission induced by incoming photons (or spontaneously emitted photons), than it is able to absorb. The light can thus be amplified inside the material.

The rates of absorption, R_{abs}, stimulated emission, R_{st}, and spontaneous emission, R_{sp}, are usually described by using *Einstein's coefficients*, A and B. The emission rates (both stimulated and spontaneous emission) increase, and the absorption rate decreases with increasing population inversion. Both, absorption and stimulated emission rates also increase with increasing photon density (of resonant photons). With Einstein's coefficients, the emission and absorption rates can be written as:

$$R_{sp} = Af_2(1-f_1), \tag{1}$$

$$R_{st} = Bf_2(1-f_1)N_{ph}, \tag{2}$$

$$R_{abs} = Bf_1(1-f_2)N_{ph}, \tag{3}$$

where f_1 and f_2 are the occupation probabilities of the lower (1) and upper (2) energy levels, and N_{ph} is the number density of photons. The importance of the population inversion for the generation of the optical gain is explained by noting that the absorption and stimulated emission rates are (anti-) symmetrical with respect to the occupation probabilities. The total photon emission rate, R_{ph}, is given by:

$$R_{ph} = R_{sp} + (R_{st} - R_{abs}) = Af_2(1-f_1) + B(f_2 - f_1)N_{ph}, \tag{4}$$

where the population inversion term ($f_2 - f_1$) is explicitly shown.

The actual photon emission rate for a given material (i.e. if A and B are fixed) thus depends on two factors, 1) the electron population of the two energy levels and 2) the photon density. The electron population in the upper energy level is determined by the balance between the pumping rate, R_{pump}, that tends to increase the population inversion and the electron recombination rate, R_R, that tends to decrease the population inversion. The electron recombination rate determines how fast the electrons are transferred from the upper energy level to the lower level. The electron recombination rate is the sum of the radiative transition rate, R_{rad}, that equals the photon emission rate, $R_{ph} = R_{rad}$, and a non-radiative transition rate, R_{nr}. The balance is thus given as:

$$R_{pump} = R_R = R_{rad} + R_{nr} = R_{ph} + R_{nr} \,. \tag{5}$$

Similarly, the photon density is determined by balancing the photon emission rate, $R_{ph,}$ and the photon loss rate, R_{loss}:

$$R_{ph} = R_{loss} \,. \tag{6}$$

The photon loss rate includes the photon absorptions, for example due to impurities in the material, and the photon flow out of the system. These two equations are known as the *rate equations* for the laser in the steady state. If the rates are unbalanced, we can write the rate equations as differential equations for the densities of excited electrons, N, and photons:

$$dN/dt = R_{pump} - R_{rad} - R_{nr} \tag{7}$$

and

$$dN_{ph}/dt = R_{ph} - R_{loss} \,, \tag{8}$$

where t is time.

We can define a laser as a device in which the spontaneously emitted (or otherwise incident) photons get copied via stimulated emissions over and over again. Due to this copying process, a macroscopic number of photons will eventually occupy one (or few) photon states in the surrounding space and thereby the coherent behavior of these photons can be observed in macroscopic scale. The condition for lasing can be defined as a state where the stimulated emission rate exceeds the spontaneous emission rate, bringing out the coherent behavior of the multiple photons that occupy a single (or few) photon state.

To fulfill the lasing condition, the population inversion must be strong and the photon density must be high (cf. Equation (4)). The population inversion can be increased by strong pumping. The photon density is kept high by not letting the photons get out of the material. Lasers therefore usually consist of a resonant cavity enclosed by mirrors, inside which the light amplifying material resides. The photons must go through numerous round trips in the laser cavity before they can escape from it.

The structure of the resonant cavity significantly affects the laser operation and the characteristics of the output beam of light. Actually, most of this thesis considers one example of laser cavity design, namely the ESEC lasers. The pumping methods and the amplifying materials play the other major roles in the laser designing. A review of the continuously expanding field of laser technologies is far out of the scope of this introduction. Instead, we will consider a narrow, though in the modern data-transfer oriented society, extremely important, subsection of this field, the semiconductor lasers.

2.1.2 Gain spectrum of a semiconductor laser

The gain spectrum of a semiconductor laser is an important parameter for the operation of ESEC lasers. The gain spectrum means the amplification of light per unit propagation distance as the function of wavelength. To understand where the distribution of the gain spectrum originates, we will briefly describe the basics of the effective mass theory of the semiconductor laser gain.

2.1.2.1 Bulk lasers

The electronic band structure of a semiconductor material consists of a nearly fully occupied *valence band* at lower electronic energies and an almost unoccupied *conduction band* at somewhat higher electronic energies. For many semiconductor materials, the gap between these two energy bands corresponds to photon energies in visible and near-infrared regions. The electrons at the conduction band can move rather freely, obeying, at low values of the momentum k, the parabolic dispersion relation familiar for kinetic energy of free particles:

$$E_c = E_g + \frac{k^2\hbar^2}{2m_c}, \tag{9}$$

where E_c is the energy of an electron at the conduction band, E_g is the energy level at the bottom of the conduction band and $\hbar$ is the reduced Planck's constant. In this equation, the free-electron mass, m_0, has been replaced by the *effective mass* of the conduction band electrons, m_c. This change is needed due to the interaction between the electron and the crystal lattice. A similar dispersion relation applies to the *holes*, i.e., the unoccupied electronic states, in the valence band,

$$E_v = -\frac{k^2\hbar^2}{2m_h}, \tag{10}$$

where E_v is the energy of the hole in the valence band. The effective mass for holes, m_h, has now been used. The negative sign refers to the *missing* electron at the electronic state. Only the relative energies of the electronic states are important in the following analysis. Therefore, the zero energy level has been customarily chosen to be at the top of the valence band. These two bands are the basis of the lasing in semiconductors.

Now, the problem is that instead of two separate energy levels, we have two *bands* of energies. Therefore we have to use the concept of the *density of states* to describe the electron populations in the energy bands. For the parabolic bands in the bulk material, the density of states is given as

$$\rho(E) = \frac{1}{2\pi^2}\left(\frac{2m^*}{\hbar^2}\right)^{\frac{3}{2}} E^{1/2}, \tag{11}$$

where m^* is either m_c or m_h, and E equals either $E_c - E_g$ or E_v for conduction and valence bands, correspondingly. Let us define a transition rate $R_r = (R_{st} - R_{abs}) / (f_2 - f_1)$. For harmonic disturbances, like photons, with energy E_{21}, *Fermi's golden rule* states that

$$R_r(E_{21}) = \frac{2\pi}{\hbar} |H'_{21}|^2 \rho_r(E_{21}), \qquad (12)$$

where $\rho_r(E_{21})$ is the *reduced density of states*,

$$\frac{1}{\rho_r(E_{21}(k))} = \frac{1}{\rho_v(E_v(k))} + \frac{1}{\rho_c(E_c(k) - E_g)}, \qquad (13)$$

where $E_{21}(k) = E_c(k) – E_v(k)$. (The index 21 refers to the transition from the energy level 2, i.e. the conduction band, to energy level 1, i.e. the valence band.) The terms ρ_v and ρ_c are the densities of state for the valence band and the conduction band, correspondingly. For a material with parabolic energy bands, the reduced density of states can be expressed with Equation (11) by replacing E with $E_{21}–E_g$ and m^* with the *reduced mass* m_r^*, where $m_r^{*-1} = m_c^{-1} + m_v^{-1}$. The interaction between the electronic states in the valence band, Ψ_v, and in the conduction band, Ψ_c, is determined by the *perturbation matrix element* $H'_{21} = <\Psi_c|H'|\Psi_v>$, where $H'(\boldsymbol{r}) = q/(2m_0)\, A(\boldsymbol{r})\, \boldsymbol{e} \cdot \boldsymbol{p}$ describes the time-dependent electromagnetic perturbation in the Hamiltonian operator. Here q is the electron charge, $A(\boldsymbol{r})$ is the amplitude of the vector potential of the electric perturbation (photon), $\boldsymbol{e}$ is a unit polarization vector of the field, and $\boldsymbol{p}$ is the momentum operator. To calculate the integral $<\Psi_c|H'|\Psi_v>$, the electronic wave functions, Ψ, can be separated to *envelope* functions, F, and *Bloch* functions, u, $\Psi = Fu$, where the envelope function satisfies the macroscopic potential of the system and the Bloch function satisfies the atomic level periodic potential of the crystal lattice. The envelope function for a bulk material is a plane wave of a particle with the effective mass m^*. The integration of the perturbation matrix element gives

$$|H'_{21}|^2 = N_{ph} \frac{q^2 \hbar}{2 n n_g \varepsilon_0 m_0^2 \omega} |M_T|^2, \qquad (14)$$

where n is the refractive index, n_g is the group index, ε_0 is the dielectric constant, and ω is the angular frequency of the time-harmonic electric field of the photon. The term $|M_T|^2$,

$$|M_T|^2 = 1/3|M|^2 \delta(k,k'), \tag{15}$$

is called the *transition matrix element*. The *momentum matrix element*, $|M|^2$, is a constant for a given material. The delta function defines the *k-selection rule*, which states that the transitions are only possible from one k-state in the conduction band (k) to the same k-state in the valence band (k'). (Actually, the k-selection rule was already used in Equation (13) for the *reduced density of states*.)

The optical gain, g, for the semiconductor material is given as

$$g = \frac{(R_{st} - R_{abs})}{N_{ph} v_g} = R_r \frac{(f_2 - f_1)}{N_{ph} v_g}, \tag{16}$$

where v_g is the group velocity of light in the material. Inserting the Equations (12) and (14) to Equation (16) results in

$$g(E_{21}) = g_{\max}(E_{21})(f_2 - f_1), \tag{17}$$

where

$$g_{\max}(E_{21}) = \frac{\pi q^2 \hbar}{\pi \varepsilon_0 c m_0^2} \frac{1}{h\nu_{21}} |M_T(E_{21})|^2 \rho_r(E_{21}), \tag{18}$$

where c is the speed of light, h is the Planck's constant, and ν_{21} is the frequency of light corresponding to the energy E_{21}.

Now, the only terms left to be determined are the occupation probabilities f_1 and f_2. These terms obey the Fermi–Dirac statistics:

$$f(E,E_f) = \left[e^{(E-E_f)/K_BT} + 1\right]^{-1}, \tag{19}$$

where E_f is the *Fermi level,* K_B is the Boltzmann's constant and T is the temperature. To relate the Fermi level to the electron and hole densities, N and P, i.e. to get the relations $E_f(N)$ and $E_f(P)$, we must solve the integral equations

$$N = \int_0^\infty \rho_c(E) f(E, E_f) dE, \tag{20}$$

$$P = \int_0^\infty \rho(E)\left[1 - f(E, E_f)\right] dE. \tag{21}$$

For bulk materials, these equations lead to so called inverse Fermi–Dirac integrals that are solved either numerically or by using approximated solutions (see e.g. [17], pp. 415–420).

Figure 1 shows how two parameters affect the gain. The first parameter, shown on the left panel of Figure 1, is the carrier density, i.e. the density of conduction band electrons and valence band holes in the semiconductor material. The increase in the carrier density increases the gain and shifts the gain peak towards the shorter wavelengths. For very high current densities, the gain curve approaches the maximal gain, g_{max}, drawn in Figure 1 with a dashed line. Another important factor is the temperature. As shown on the right panel of Figure 1, the increasing temperature weakens the gain and shifts the gain peak towards the longer wavelengths. Both of these effects reflect the changes in the Fermi–Dirac distribution in the two energy bands: The increasing carrier density makes the Fermi levels go up, therefore allowing the transitions of higher photon energies, i.e. shorter wavelengths. The increasing temperature widens the transition zone from occupied to unoccupied electronic states and therefore smoothens the gain curve.

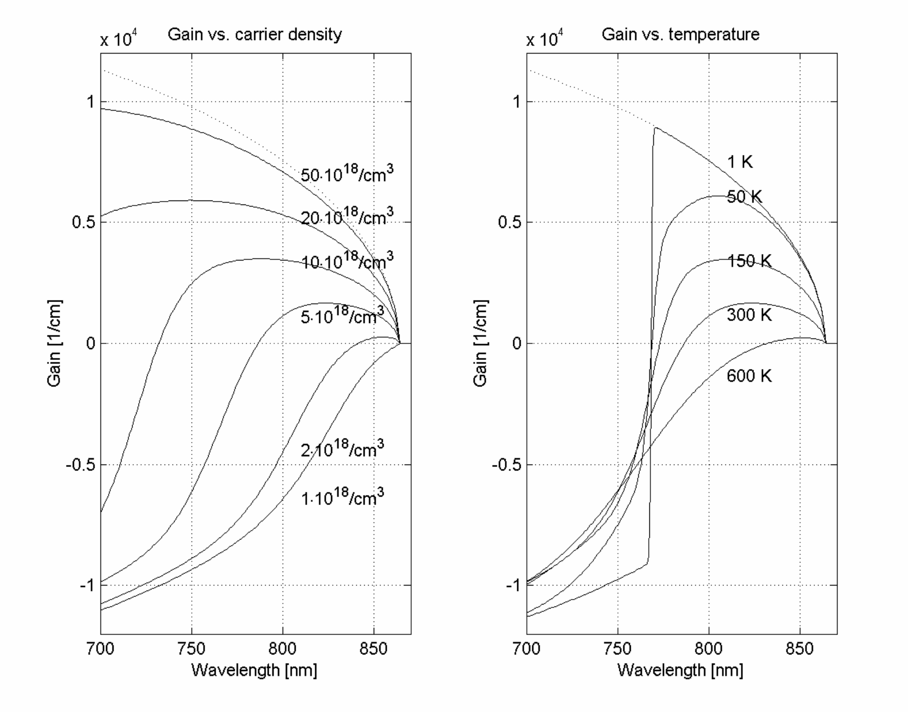

Figure 1. Material gain spectrum as the function of the carrier density N (left) and temperature T (right) for a bulk material (GaAs).

The relation between the Fermi–Dirac distributions and the gain spectrum (taking into account these two factors, N and T) explains much of the semiconductor laser behavior, especially when the lasing wavelength is considered. The rest is explained by the laser cavity design, which will be considered in Section 2.1.3. Even though the analysis shown above was made for bulk materials, most of it applies to quantum well (QW) lasers as well. We will next briefly consider the special properties of the quantum well lasers.

2.1.2.2 Quantum well lasers

Most of the current commercial semiconductor lasers are using quantum well (QW) structures instead of bulk gain layers. The analysis shown for the bulk semiconductors applies to the QW lasers as well, if some changes are made in the functional form of the terms.

The QW confines the electrons' movement in one dimension. The result is that the envelope part of the wave function, describing the electronic state, will change from a plane wave to a standing wave in the bounded direction. The standing wave has only a discrete set of possible k-states (in the bounded direction). This will cause the energy bands to split into several sub-bands. This splitting is seen as steps in the density of states function, ρ. The change in the density of states will directly affect the shape of the maximal gain, g_{max}, versus the wavelength, where the steps will appear too, as demonstrated in Figure 2. The change in the envelope functions will also affect the transition rate via the perturbation matrix element, where it affects the relation between the transition matrix and the momentum matrix elements, $|M_T|^2$ and $|M|^2$.

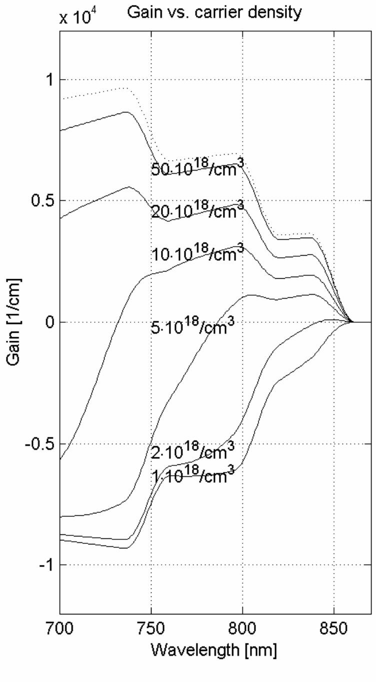

Figure 2. Material gain as the function of the carrier density N for a quantum well structure.

Without going into the details, the result of all of this is that the maximum gain, g_{max}, of the QW structure will have a different functionality of wavelength compared to the bulk material. This will directly affect the actual gain. In addition to this, the relation between the Fermi level and the carrier density will change because of the change in the density of states in Equations (20) and (21). The stepped curve of the maximal gain produces more peaked gain curves than the bulk material and thereby gives better lasing characteristics for the QW semiconductor lasers.

This analysis has given only the basic lines of the physics behind the semiconductor laser gain. Very detailed work has been done in calculating the gain for both bulk and QW lasers, see for example [19, 20, 16].

2.1.2.3 Measuring the gain spectrum

The gain spectrum of an edge emitting Fabry–Perot semiconductor laser can be measured by using a method introduced by Hakki and Paoli [21], which is based on the linear amplifier theory. In this method, the amplified spontaneous emission (ASE) spectrum of the laser, i.e. the emission spectrum of the laser operating below or close to the lasing threshold, is measured. The modulation depths, r_m, of the longitudinal Fabry–Perot modes are determined from the spectrum by dividing the average peak power of each pair of two adjacent modes, $(P_m+P_{m+1})/2$, with the power value of the valley between these modes, V_m:

$$r_m = \frac{P_m + P_{m+1}}{2V_m}. \tag{22}$$

This is visualized in Figure 3, where an ASE spectrum of a 1550-nm InGaAsP/InP 4-QW laser (Laser 1 in Table 1) is shown. The material gain at the longitudinal mode m is given as

$$g_{mi} = \left(\frac{1}{L} \ln\left(\frac{r_m^{1/2} - 1}{r_m^{1/2} + 1} \right) - \frac{1}{L} \ln(R_b R_f) \right) + \alpha_I , \tag{23}$$

where L is the length of the Fabry–Perot laser cavity, α_I represents the internal losses in the laser cavity, and R_b and R_f are the intensity reflectances of the back and the front facets of the laser.

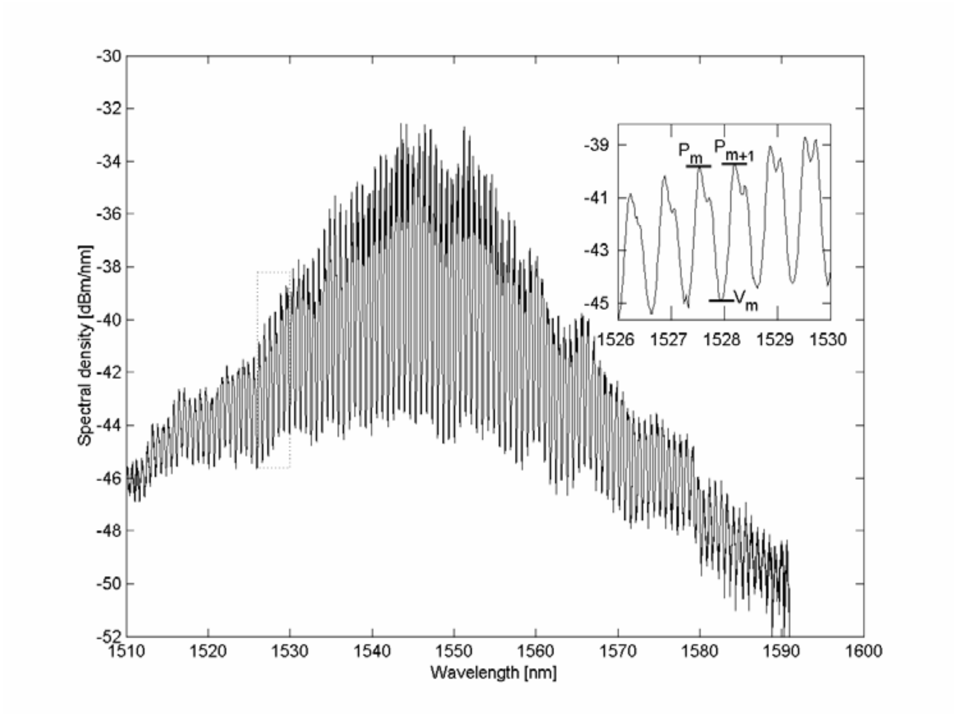

Figure 3. Amplified spontaneous emission (ASE) spectrum for an InGaAsP/InP 4-QW laser. The inset shows the definitions of the peak and the valley powers.

Table 1. Specifications of the lasers used in the work.

Code	**Laser 1**	**Laser 2**	**Laser 3**
Manufacturer	Ioffe	Mitsubishi	*model*
Type	Custom	CD laser	
Material	InGaAsP/InP, 4-QW	GaAs	GaAs
Wavelength	1550 nm	790 nm	850 nm
Threshold current	25 mA	25 mA	25 mA
Operating current (typical)	50 … 100 mA	50 … 100 mA	70 … 100 mA
Power	30 mW	-	-
Cavity length	500 μm (or 700 μm)	500 μm	400 μm
Emitting aperture	5 μm × 1 μm	3 μm × 1 μm	3 μm × 1 μm
Front facet reflectivity	AR, R = 5 % (or 15 %)	AR, R = 5 %	R = 50 %
Back facet reflectivity	AR, R = 90 % (or 70 %)	AR, R = 90 %	R = 50 %

Figure 4 shows an example of the modal gains for an InGaAsP/InP 4-QW laser measured for various injection current levels just below the threshold by using the Hakki–Paoli method. The gain for the injection current of 23 mA corresponds to the ASE spectrum shown in Figure 3. These measured curves will be used in some of the analysis in Sections 4.2 and 4.3.

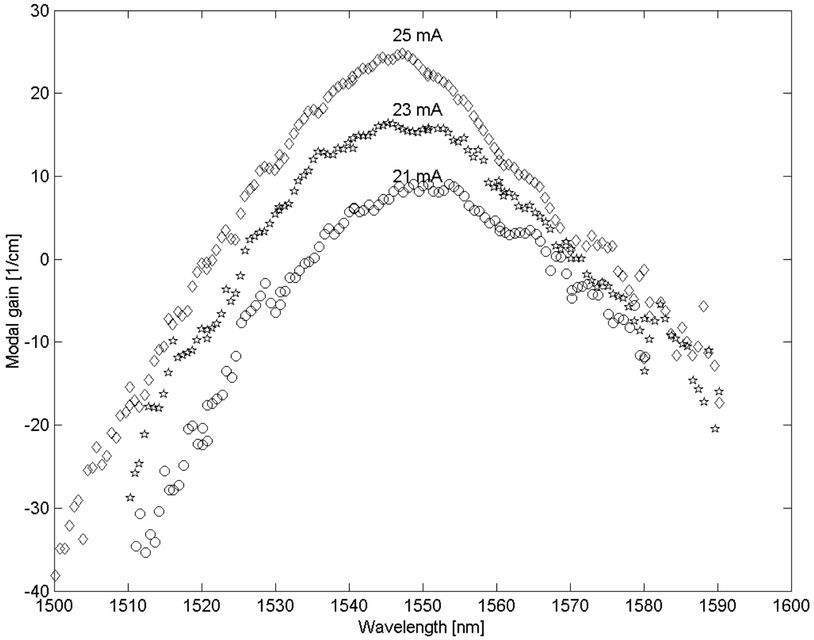

Figure 4. Modal gain for an InGaAsP/InP 4-QW laser measured with several injection current levels using the Hakki–Paoli method.

2.1.3 Semiconductor laser cavity

Most of the work presented in this thesis will consider the design, modeling and use of the resonant cavity of the semiconductor laser to control the laser operation. The main purpose of the laser cavity is to force the light to propagate a long distance in the gain medium before getting out of the laser. That dramatically increases the number of stimulated emissions per one spontaneous emission and thus enables the laser operation. The secondary purpose of the resonant cavity is to shape the spectrum of the light emitted by the laser by modifying the modal gain spectrum and the resonance conditions of the laser. The resonant cavity can also be used to shape the wavefront of the output beam of light.

The review of all the cavity structures used with the semiconductor lasers is far out of the scope of this work. Some of the most important types of semiconductor laser cavities are shown in Figure 5. In this thesis, we concentrate on the edge emitting Fabry–Perot lasers working in the external cavity configuration.

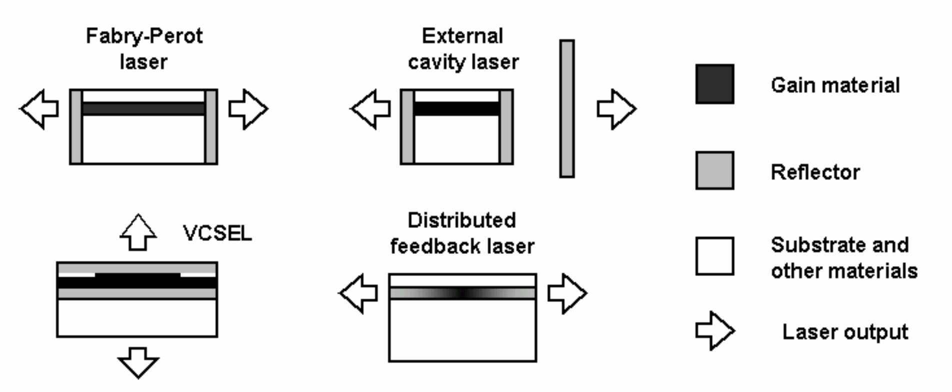

Figure 5. Various types of semiconductor laser cavities. VCSEL stands for vertical cavity surface emitting laser.

The cavity of the Fabry–Perot semiconductor laser consists of the gain material and the mirrors at the two ends of the gain material. The gain material is formed in an epitaxially grown multilayer structure providing the confinement for both the charge carriers (electrons and holes) and the photons. This structure is called a double heterostructure. The heterostructure provides the confinement in the vertical direction (see Figure 6). The optical and electrical confinement in the lateral direction can be provided by etching a stripe to the multilayer structure on the surface of the substrate. This stripe forms a waveguide for the light oscillating in the laser cavity. For a semiconductor laser with a single transversal mode, the effective size of the waveguide is usually about 1 μm in the vertical direction and 3…5 μm in the lateral direction. The semiconductor materials used in the heterostructue are often combinations of materials such as GaAs, AlGaAs, InGaAs, or InP, tailored for the needed electronic band energies. Figure 6 shows a schematic picture of the stripe geometry called buried double heterostructure [22], which is a commonly used laser waveguide geometry.

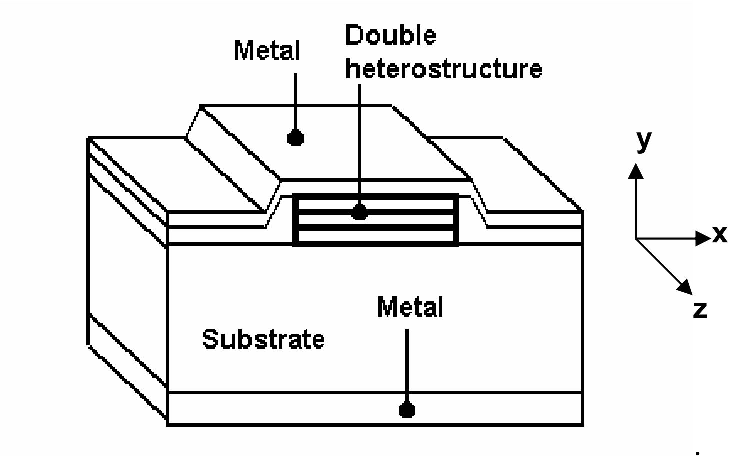

Figure 6. Laser waveguide constructed as a buried heterostructure. x – lateral direction, y – vertical direction, z – longitudinal direction.

The laser cavity of the Fabry–Perot laser is formed as a small section of the double heterostructure stripe waveguide. The section is usually cleaved from the substrate in a suitable crystal direction. This way the end of the waveguide becomes very flat and the end facets of the waveguide can be used as the reflectors for the laser cavity. To increase the reflectivity and thereby decrease the threshold current, at least one of the facets is often coated with a high reflectance coating. In addition, a low reflectance coating can be used in the other facet to increase the output from that end of the laser waveguide.

The length of the laser waveguide and the effective refractive index of the material (or the propagation vector of the optical fields) will define the longitudinal resonant optical modes that are oscillating in the laser cavity. The cross sectional area and the shape of the waveguide will define the transversal mode structure. In this thesis, we assume that the laser waveguide is narrow enough to carry only a single transversal mode. The reflectivity spectrum of the cavity mirrors, together with the material gain will define the *modal gain* for each of the longitudinal modes. The modal gains will then define the laser's wavelength spectrum. All of this is explained in detail with the description of the phenomenological laser model in Section 3.1.

2.2 External cavity lasers

External cavity semiconductor lasers can be defined as semiconductor lasers whose oscillating cavity is extended beyond the end-facets of the laser waveguide providing the gain. In this section, we will briefly review the history and the most important applications of the EC semiconductor lasers. We will also show the basic types of EC lasers and discuss the classification of the EC lasers based on the external cavity length and the strength of the optical feedback.

2.2.1 History and applications briefly

The external cavity lasers were invented shortly after the invention of the semiconductor lasers. The first published studies on the EC lasers were made in the early 1970's by several Russian scientists [2, 23, 24, 1]. Theory of the operation of EC lasers was developed in the late 1970's and the early 1980's [3, 25, 26, 27, 28, 29]. Dynamical studies and theory have been presented by several authors in the early 1980's [30, 5, 6, 31].

After the early studies, external cavity lasers have been used in various applications. These applications include frequency and power stabilization of semiconductor lasers (see e.g. [32, 33] and references therein), producing chaotic laser operation (see e.g. [34]), wavelength tuning and other types of spectral control of semiconductor lasers (see e.g. [35, 36]), mode locking of the lasers to produce pulsed oscillations in the laser power (see e.g. [37]), and various sensor applications (see e.g. [38, 39, 40, 41]). Perhaps the most important application of the EC lasers is the grating-tuned external cavity laser depicted in Figure 7. In this configuration, the wavelength selectivity of the external grating is used for tuning the wavelength of the semiconductor laser.

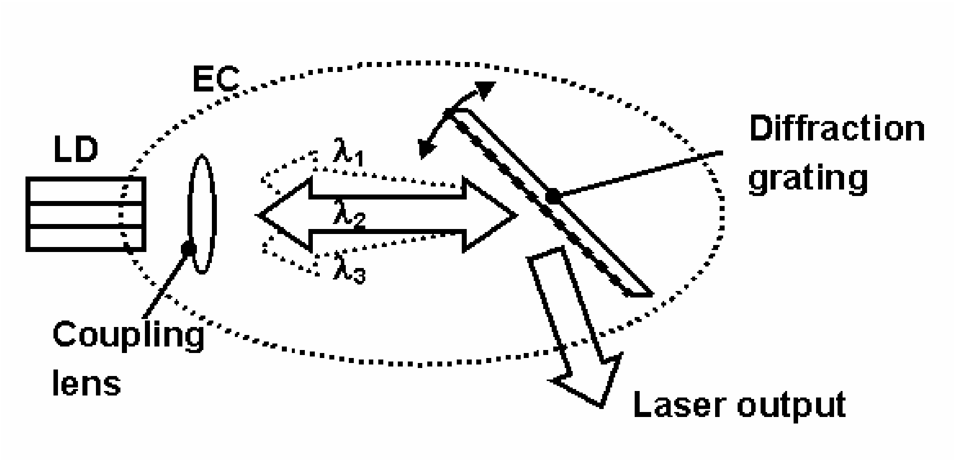

Figure 7. Schematic figure of a grating-tuned EC laser.

2.2.2 Basic EC structures and classification

The EC configuration can be realized in many different ways as shown in Figure 8. The simplest realization of the EC structure is the *direct coupling* configuration where an external mirror is brought to the close proximity of one of the end-facets of the laser waveguide. Some part of the light emitted by the laser is coupled back to the laser waveguide affecting the laser operation. The direct coupling can be used for the short external cavity lengths. The coupling strength can be increased by using a concave mirror or a diffractive element as the reflector, or using an additional optical coupling element. Figure 8B shows a *lens coupling* configuration that is commonly used for the 'mid-range' external cavity lengths (up to meters). In the longer external cavity lengths, an optical fiber may be used as the media in the external cavity to increase the strength of the optical feedback ('*fiber coupling*'). The external cavity lasers can also be realized using the *monolithic* integration of active and passive parts of the laser waveguide. Usually the term *combined-cavity lasers* is used for these kinds of monolithic solutions.

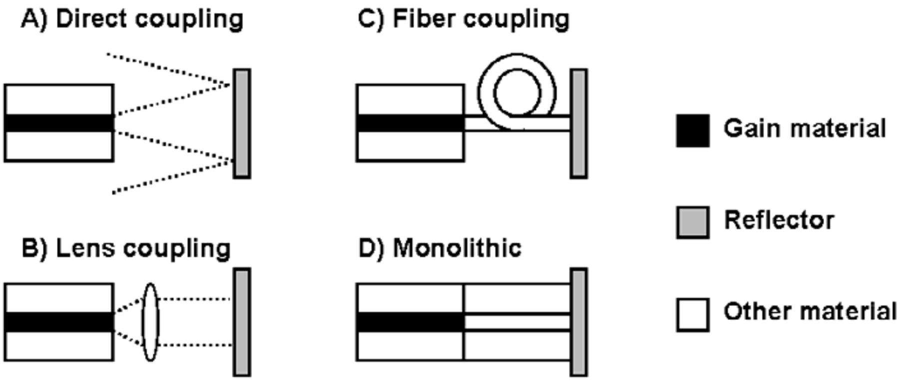

Figure 8. Various types of EC laser configurations.

The operation of the EC lasers depends highly on two factors: the external cavity length (delay of the feedback) and the feedback strength as shown originally by Tkach and Chraplyvy [6] (see also e.g. [33]). Not going into the details of the various dynamical operating regimes, we can make a rough classification of EC lasers. The EC lasers that are often used can be divided into four principle types as shown in the diagram in Figure 9. We call these groups 1) the delayed feedback lasers, 2) the long external cavity lasers, 3) the short external cavity lasers and 4) the extremely short external cavity lasers. The last two types can be thought to be sub-groups of the short external cavity lasers, but we have customarily chosen to use this division to discuss the special properties related to the extremely short external cavity lasers. Also, this division should not be considered an exhaustive classification, but rather a practical 'rule-of-thumb' division.

- The **delayed feedback lasers** (or 'weak delayed feedback lasers') are usually used for the study of the non-linear dynamics of the lasers operating in the unstable 'coherence collapse' region. The main idea of these lasers is to use a delayed optical feedback to break-up the standing-wave pattern inside the laser. The delay time must be on the order of or longer than the natural temporal coherence time of the laser radiation – i.e. close to the lifetime of the photon in the laser cavity. The coherence collapse region can be reached by using the external cavity lengths from centimeters to meters or even longer. The feedback strengths should be lower than about 10 % of the light emitted by the laser, depending on the used delay time. (For very low optical feedback levels, the influence of the feedback on the laser operation weakens, and the laser may again become stable under certain conditions. For simplicity, we leave the consideration of these operational regions out of this discussion.)

- The **long external cavity (LEC) lasers** (or 'strong delayed feedback lasers') are operating with the same external cavity length region as the delayed feedback lasers, but using higher optical feedback levels. The stronger feedback provides stable laser operation and reduces the linewidth of the laser. For example, grating tuned external cavity lasers (Figure 7) are operating in this region.

- The **short external cavity (SEC) lasers** are operating in the external cavity lengths shorter than centimeters. In that region, the delay effects on the feedback are negligible, and the laser operation is stable. The feedback strength may be chosen freely without a major effect on the dynamical operation of the laser.

- The **extremely short external cavity (ESEC) lasers** have external cavity lengths of less than ~100 micrometers. The laser operation is stable in all the feedback levels. The EC length is optically much shorter than the internal laser cavity length. The extremely short EC length makes it possible to use direct coupling configuration to provide high feedback levels.

In the dynamical sense, there is no difference between the ESEC lasers and the SEC lasers. The ESEC lasers are stable in all levels of optical feedback. However, there are two main differences between the ESEC lasers and the SEC lasers. The first difference is that for the ESEC lasers, the wavelength separation of the longitudinal modes of the external cavity is clearly larger than the wavelength separation of the longitudinal modes in the 'internal' laser cavity. The external cavity of the ESEC laser is thus optically much shorter than the internal laser cavity. That leads to the possibility of a novel use of the interference effects on the laser facet adjacent to the ESEC to control the laser operation. Several examples of this will be shown later on in this thesis.

The second difference between the SEC and the ESEC lasers is that for the ESEC lasers, the feedback levels can be made high by using the simple 'direct coupling' configuration – no additional optical components like coupling lenses are necessary. This leads to the more pronounced importance of understanding the diffraction effects and the diffracted-beam control in the design of the ESEC lasers than in the design of the SEC lasers. These two differences are rather shallow, but they make a difference in the practical realizations and use of the ESEC lasers. Next we will start to analyze the operation of the ESEC lasers more deeply, first considering ESEC lasers from the modeling perspective.

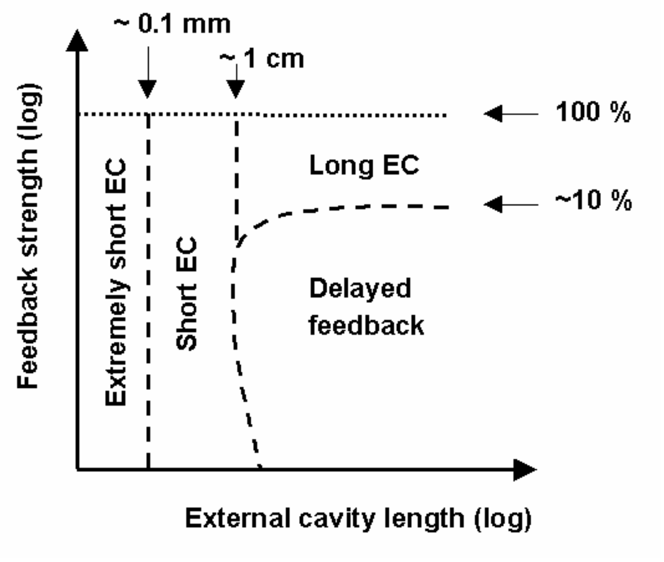

Figure 9. Practical classification of EC lasers.

3. Model for the ESEC laser

In the previous section, we gave a general review of the optical physics related to semiconductor lasers and external cavity (EC) lasers. In this section, we will describe how we have modeled the operation of the ESEC lasers. We will first describe our phenomenological laser model that we have used in order to model the internal operation of the semiconductor laser. The model of the ESEC is connected to the laser model via the effective reflectance of the ESEC. In Section 3.2, we will give a definition for the effective reflectance and in Section 3.3 we will show some ways to calculate the effective reflectance.

3.1 Phenomenological laser model

We have constructed a simple but sufficiently accurate model of the ESEC semiconductor laser system. The model is a simplified version of the laser model presented by Aikio and Howe in the reference [10] and used in [7, 8, 13, 15]. A related work on predicting the EC laser's spectrum has been presented in the references [3, 27, 28]. Most of the basic theory needed for the model has been taken from [17]. Multimode steady state rate equations are used in the model. Because of the complexity of the gain spectrum and the dynamics of the real semiconductor laser, the results produced by this model should be considered semi-quantitative. We will now describe the model that we use in the calculation of the multi-mode lasing characteristics of the semiconductor laser.

3.1.1 Longitudinal modes of the laser

Since we are modeling a multi-mode (multiple longitudinal modes) operation of the laser, let us first give the resonance condition that determines the longitudinal modes in the laser. The resonance condition states that the relative phase of the light after the round-trip in the laser cavity must be equal to a multiple of 2π:

$$2\pi \frac{2Ln}{\lambda_m} + \phi_{b,m} + \phi_{f,m} = m2\pi \,, \tag{24}$$

where L is the length of the laser cavity, n is the effective refractive index in the cavity, $\phi_{b,m}$ and $\phi_{f,m}$ are the phases of the modal reflectance at the back facet and at the front facet of the laser, correspondingly, (the back and the front facet reflectances are complex numbers: $r_b = |r_b|\exp(i\phi_b)$ and $r_f = |r_f|\exp(i\phi_f)$) and m is the order of the longitudinal mode. The wavelength, λ_m, corresponding to the m^{th} longitudinal mode can be solved from this equation. Let us write the solution here for clarity:

$$\lambda_m = \frac{2Ln}{m - (\phi_{b,m} + \phi_{f,m})/2\pi} \,. \tag{25}$$

3.1.2 Rate equations

3.1.2.1 Carrier rate equation

The *carrier rate equation* for a semiconductor laser can be written as (see [17], pp. 30–31):

$$I = \frac{Vq}{\eta_I}\left[R_{nr} + R_{sp} + R_{st}\right] \tag{26}$$

where I is the injection current to the laser, V is the volume of the active part of the laser cavity, q is a unit charge, and η_I is the internal quantum efficiency of the laser. The recombination rates R_{nr}, R_{sp} and R_{st} are, correspondingly, the rates for the non-radiative, the spontaneous radiative, and the stimulated radiative recombinations per unit time and unit volume. The non-radiative rate can be approximated as a function of the carrier density, N, as:

$$R_{nr} = AN + CN^3, \tag{27}$$

where A and C are constant coefficients. Similarly, the spontaneous emission rate can be approximated as

$$R_{sp} = BN^2, \tag{28}$$

where B is a constant. The stimulated emission rate is the sum of the emissions to the longitudinal modes in the laser:

$$R_{st} = \sum_m R_{st,m}, \tag{29}$$

where $R_{st,m}$ is the stimulated emission rate for the m^{th} mode. The modal stimulated emission rate can be written as:

$$R_{st,m} = v_{g,m} g_m \Gamma_m N_{ph,m}, \tag{30}$$

where $v_{g,m}$ is the group velocity of the light for mode m, g_m is the gain of the active medium, Γ_m is the confinement factor of the optical field in the gain medium, and $N_{p,m}$ is the number density of photons for mode m.

We have modeled the gain of the active medium using a logarithmic relation between the carrier density and the strength of the gain. The wavelength dependency was modeled using a measured or approximated gain spectrum $g(\lambda)$ (see Section 2.1.2.3). In the logarithmic model, the peak value of the gain spectrum, g_{peak}, follows the equation (cf. [17] p. 44, Equation (2.40)):

$$g_{peak}(N) = g_0 \ln\left(\frac{N + N_s}{N_{tr} + N_s}\right), \tag{31}$$

where g_0, N_s and N_{tr} are fitting parameters. The gain of the medium for mode m is given as

$$g_m(N) = g_{peak}(N) - \Delta g_{m,\max}, \tag{32}$$

where $\Delta g_{m,max}$ = $\max_\lambda[g(\lambda)] - g(\lambda_m)$, is the difference in the gain between the peak gain and the gain for the mode *m* at the wavelength λ_m. Note that here the $g(\lambda)$ refers to the measured gain spectrum and the g_{peak} to the model of Equation (31).

3.1.2.2 Photon rate equation

The *photon rate equation* can be written for each of the modes as (cf. [17], p. 35):

$$R_{st,m} + R'_{sp,m} = R_{loss,m}, \tag{33}$$

where $R_{loss,m}$ is the photon loss rate and $R'_{sp,m}$ is the spontaneous photon emission rate to the mode *m*. For the modal spontaneous emission rate, we have used a simple approximation

$$R'_{sp,m} = \frac{1}{D} R_{sp} = \frac{B}{D} N^2 . \tag{34}$$

Here D>>1 is a constant; i.e. the modal spontaneous emission rate is a small proportion of the total spontaneous emission rate. The photon loss rate can be written as

$$R_{loss,m} = v_{g,m} \alpha_m N_{ph,m}, \tag{35}$$

where $N_{ph,m}$ is the number density of photons in the mode *m*, α_m is the decay term (or 'loss term') including the internal losses, α_I, and the mirror losses $\alpha_{M,m}$:

$$\alpha_m = \alpha_{M,m} + \alpha_I . \tag{36}$$

The mirror loss term is related to the reflectivities of the mirrors of the laser cavity as:

$$\alpha_{M,m} = -\frac{1}{L}\ln\left(\left|r_{b,m}\right|\left|r_{f,m}\right|\right), \tag{37}$$

where $r_{b,m}$ is the amplitude reflectance of the back facet of the laser and $r_{f,m}$ is the amplitude reflectance of the front facet of the laser for the mode m. The length of the laser cavity is denoted as L.

3.1.3 Threshold condition

The threshold condition is often defined as the state where the gain and the losses are equal for the light oscillating in the laser cavity. This definition is misleading, since the gain term will never reach the loss term in the steady state laser operation. To keep the balance between the gain and the loss, the gap between the gain and the loss terms is filled with the source term, i.e. the spontaneous emissions. If we include the spontaneous emissions in the 'gain' in the definition of the threshold condition (i.e. 'the gain plus the spontaneous emissions are equal to the losses in the laser'), we end up in the photon conservation equation (or photon rate equation), which is always valid – above or below the 'threshold'. The conventional threshold condition does not describe the laser operation, but gives a good approximation of the values of certain operational parameters when the laser is lasing.

We use the conventional threshold condition to approximate the carrier density and the 'threshold current' for the laser. For the multimode operation, the threshold condition can be formulated so that the gain and the loss are equal for one of the modes. The threshold condition is thus:

$$\min_m\left[\alpha_m - \Gamma_m g_m(N_{th})\right] = 0, \tag{38}$$

where N_{th} is the threshold carrier density, defined by this equation. The mode, $m = p$, fulfilling the threshold condition is the *principal lasing mode*, and the corresponding wavelength, λ_p, is the *principal lasing wavelength*. The threshold condition can be illustrated using the so-called gain-loss diagram shown in Figure 10. Using the diagram, the principal lasing wavelength can be found at the wavelength where the gain and the loss curves touch each other.

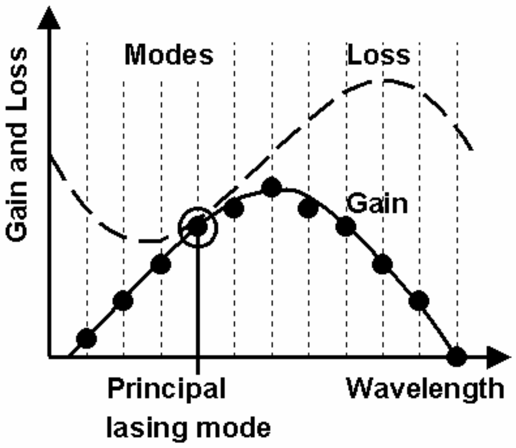

Figure 10. Illustration of the threshold condition with the gain/loss diagram.

Using the relationship between the gain and the carrier density defined in Equations (31) and (32), we can get an explicit form for the *threshold carrier density*:

$$N_{th} = e^{\left(\alpha_p - \Delta g_{p,\max}\right)/g_0}\left(N_{tr} + N_s\right) - N_s \, . \tag{39}$$

The threshold current is the part of the current consumed by the non-radiative and spontaneous recombinations at the threshold carrier density. Leaving the stimulated emission rate away from the carrier rate equation (Equation (26)), we get an expression for the *threshold current*:

$$\begin{aligned} I_{th} &= \frac{Vq}{\eta_I}\left[R_{nr}(N_{th}) + R_{sp}(N_{th})\right] \\ &= \frac{Vq}{\eta_I}\left[AN_{th} + BN_{th}^2 + CN_{th}^3\right], \end{aligned} \tag{40}$$

where, in the last equality, we used Equations (27) and (28).

3.1.4 Output power and injection current

Now, we can use Equations (35) and (30) to solve the photon density from the photon rate equation (Equation (33)):

$$N_{ph,m} = \frac{R'_{sp,m}}{v_g\left(\alpha_m - \Gamma_m g_m\right)}. \tag{41}$$

Applying the threshold condition to this equation, we can see that the denominator goes to zero and the photon density goes to infinity for the principal mode, which is not a physical solution. (To get a physical solution, the gain term, $\Gamma_m g_m$, must always be smaller than the loss term, α_m.) The photon density can, however, be approximated by applying the threshold condition only to the modal spontaneous emission rate on the numerator. Using Equation (34), that will give us:

$$N_{ph,m} = \frac{(B/D)N_{th}^2}{v_g\left(\alpha_m - \Gamma_m g_m\right)}. \tag{42}$$

The stimulated emission rate can now be calculated from Equation (30):

$$\begin{aligned} R_{st,m} &= \frac{g_m(N_{th})\Gamma_m(B/D)N_{th}^2}{\alpha_m - \Gamma_m g_m} \\ &= \frac{g_m(N_{th})\Gamma_m(B/D)N_{th}^2}{\Delta\alpha_m + \Delta g_m + \Delta}, \end{aligned} \tag{43}$$

where the gain on the numerator has been approximated to be the threshold gain. In the denominator of the last form of this equation, we have applied a customary notation [10]:

$$\Delta\alpha_m = \alpha_p - \alpha_m , \tag{44}$$

$$\Delta g_m = \Gamma_p g_p - \Gamma_m g_m , \tag{45}$$

and

$$\Delta = \alpha_p - \Gamma_p g_p , \tag{46}$$

where *p* is the denotation for the principal lasing mode. The gain and the loss terms are thus given relative to the corresponding quantities of the principal mode as illustrated in Figure 11. Term Δ is the gap between the gain and the loss terms for the principal mode.

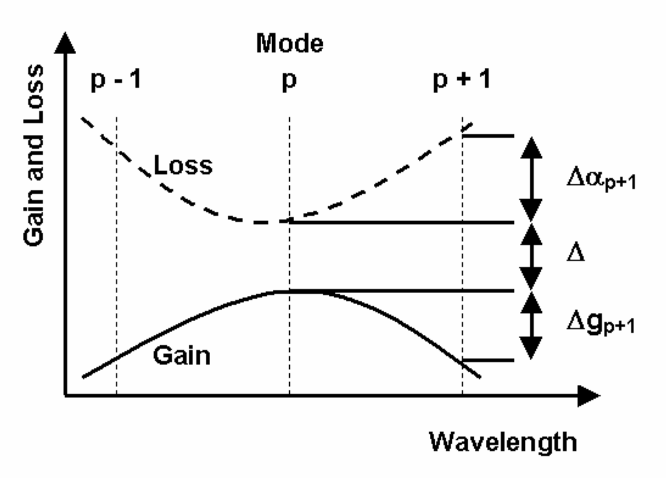

Figure 11. Explanation of the notation used in the model.

In our model, the 'delta term', Δ, is the only variable, not fixed by the threshold value of the laser operation. The stimulated emission rate is therefore a function of the 'delta term' only:

$$R_{st} = R_{st}(\Delta) = \sum_m R_{st,m}(\Delta) . \tag{47}$$

Applying this to the rate equation for the carrier density (Equation (26)), and using Equation (40) for the threshold current, we can now calculate the injection current consumed by the laser as the function of Δ:

$$
\begin{aligned}
I(\Delta) &= I_{th} + \frac{Vq}{\eta_I}\sum_m R_{st,m}(\Delta) \\
&= I_{th} + \frac{Vq}{\eta_I}(B/D)N_{th}\sum_m \frac{g_m(N_{th})\Gamma_m}{\Delta\alpha_m + \Delta g_m + \Delta}.
\end{aligned}
\tag{48}
$$

The injection current, *I*, is usually one of the predefined parameters in the modeling of the laser operation. Using Equation (48), the ‘delta term’, Δ, can be easily numerically solved for the given value of current, *I*, to get $\Delta = \Delta(I)$. The calculation of the stimulated emission rates for each of the modes is then done by inserting the calculated value of Δ to Equation (43). The modal output power of the laser can be calculated from the stimulated emission rate by transforming the number of photons to the energy of photons (multiplication with photon energy hc/λ_m), integrating over the volume of the laser cavity, *V*, and multiplying by the relative mirror loss rate $\alpha_{M,m}/\alpha_m$:

$$
\begin{aligned}
P_m(\Delta) &= \frac{hc}{\lambda_m}V\frac{\alpha_{M,m}}{\alpha_m}R_{st,m} \\
&= \frac{hc}{\lambda_m}V\frac{\alpha_{M,m}}{\alpha_m}\frac{(B/D)N_{th}^2\Gamma_m g_m(N_{th})}{\Delta\alpha_m + \Delta g_m + \Delta}.
\end{aligned}
\tag{49}
$$

The total optical power emitted by the laser is the sum of the modal powers (assuming negligible spontaneous emission):

$$
P_{tot} = \sum_m P_m . \tag{50}
$$

3.1.5 Power from the back or the front facet of the laser

The power of the laser is often monitored from one end of the laser only. The relative power from the back facet of the laser can be calculated using the reflectivities of the two ends of the laser waveguide. The ratio of the modal power, $P_{b,m}$, emitted from the back facet of the laser and the modal power, $P_{f,m}$, emitted from the front facet of the laser is given as (cf. [17], p. 78, Equation (3.29))

$$r_{b/f,m} = \frac{P_{b,m}}{P_{f,m}} = \frac{|r_{f,m}|\left(1 - |r_{b,m}|^2\right)}{|r_{b,m}|\left(1 - |r_{f,m}|^2\right)}. \tag{51}$$

The total modal power is the sum of the back and front powers: $P_m = P_{b,m} + P_{f,m}$, and therefore

$$P_{b,m} = \frac{r_{b/f,m}}{1 + r_{b/f,m}} P_m, \tag{52}$$

and

$$P_{f,m} = \frac{1}{1 + r_{b/f,m}} P_m. \tag{53}$$

3.1.6 Visualization of the modal spectrum

The plot of the modal powers as the function of the wavelength will give only the upper envelope function of the simulated spectrum of the laser. The longitudinal modes will cause modulation of the power vs. wavelength. The modulation depth was used in the Hakki–Paoli method [21] to calculate the gain from the amplified spontaneous emission spectrum of the laser. We can now use the same linear amplifier theory in the reverse order to calculate the modulation depth using the gain data, i.e. solving V_m form Equations (22) and (23).

This concludes the operational, ‘internal’ model of the semiconductor laser. Next we will see how the external cavity can be included in the model

3.2 Effective reflectance concept

3.2.1 Definition of the effective reflectance

In the ESEC laser, the mirror at the front facet of the laser is replaced with a complex external cavity structure. To calculate the effects caused by the ESEC, we can use the so-called *effective reflectance model* [4, 3, 27]. In this model, the ESEC is replaced with a compound mirror as shown in Figure 12. The reflectance of the compound mirror is called the *effective reflectance* of the ESEC. The effective reflectance, r_{eff}, is a complex number,

$$r_{eff} = \left| r_{eff} \right| \exp(i\phi_{eff}), \tag{54}$$

whose amplitude, $|r_{eff}|$, corresponds to the proportion of the laser light coupled back to the internal laser cavity from the ESEC. The phase of the effective reflectance, ϕ_{eff}, is the relative phase of the coupled light.

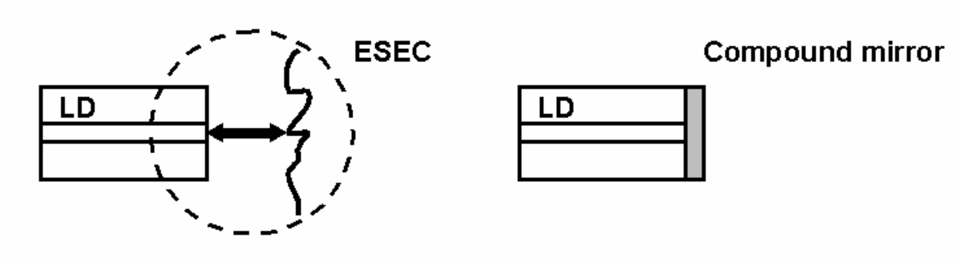

Figure 12. Effective reflectance/compound mirror concept.

Usually, the effective reflectance can be written as a coherent sum of the *external reflectance*, r_{ext}, and the *internal reflectance, r_{int},* at the laser facet (see Figure 13)

$$r_{eff} = r_{\text{int}} + r_{ext}. \tag{55}$$

The internal reflectance is the reflectance of the bare (or coated) laser facet. The external reflectance carries the part of the effective reflectance that is generated in the external cavity. The effective reflectance is usually wavelength dependent $r_{eff} = r_{eff}(\lambda)$. The wavelength spectrum of the effective reflectance determines the wavelength tuning effects in the ESEC lasers (compared to a free-running laser).

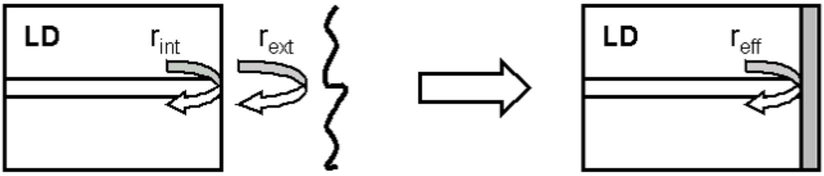

Figure 13. Effective reflectance as the sum of the internal and the external reflectances.

The effective reflectance can be applied in the phenomenological laser model simply by replacing the front facet reflectivity (or both the front and the back facet reflectivities) with the effective reflectivity everywhere in the model. This change affects the mirror loss term, $\alpha_{M,m}$, (Equation (37)) and the phase condition for the longitudinal modes (Equation (24)).

3.2.2 Validity of the effective reflectance model

The effective reflectance model can **not** be applied if

- the delay time of the feedback is long compared to the time scales of the natural phase fluctuations of the laser, or if
- the oscillation frequency of the feedback is changed compared to the light emitted by the laser.

The long delay times can lead to a chaotic dynamic operation of the laser, that can not be modeled without a dynamical model of the laser (see e.g. [5, 31, 34, 42]). This usually requires feedback distances of centimeters or meters. The length of the external cavity in the ESEC range is always shorter than about 100 μm. The delay times from the ESEC are thus shorter than the round-trip time of light in the internal laser cavity. ESEC lasers are thereby clearly within the limits of the delay condition.

The modeling of the change in the oscillation frequency of the feedback (see e.g. [43]) would require sophisticated handling of the 'cross reflectance' between different wavelengths. A change in the oscillation frequency in the ESEC structure is possible. The changes can be caused by optically non-linear materials or fast-moving components inside the ESEC. The effective reflectance model can be applied if these types of ESEC structures are not used.

There are also other EC/ESEC structures, not directly covered by the phenomenological laser model and the effective reflectance approach: arrays of laser diodes coupled via a common external mirror have been used to increase the optical output power of the lasers and to produce more collimated laser beam [24]. Broad area semiconductor lasers with an external mirror have been used to produce a controlled high-power laser beam [44]. Semiconductor lasers with the phase-conjugated feedback have been studied [45]. All of these types of the EC lasers require somewhat different approach for modeling.

Finally, for simplicity, some known factors influencing the laser's operation have been left out of the phenomenological laser model. One of these factors is the relationship between the refractive index and the carrier density. That factor is best known from the theory of the linewidth of the semiconductor laser presented by Henry [46]. The influence of this 'linewidth enhancement factor' to the EC laser dynamics has been studied e.g. by Heil et al. [47]. One important effect caused by that factor is the wavelength change of the longitudinal oscillating modes in the laser cavity as the function of the optical power in the laser, which is not taken into account in our model.

3.2.3 Remarks on the output power of the ESEC laser

The optical power from the two ends of a conventional edge emitting semiconductor laser can be calculated with Equation (53). When adding the ESEC to the system, the optical power getting out of the laser via the two facets can still be calculated using the same equation, if the front facet reflectance of the laser is replaced with the effective reflectance. However, only a part of the optical power, if any, emitted from the front facet will be transmitted through the ESEC to be observed or used as a regular laser beam. Some part of the power may be absorbed in the ESEC. Some part will be scattered from the external reflector structure and lost by not coupling back to the laser cavity.

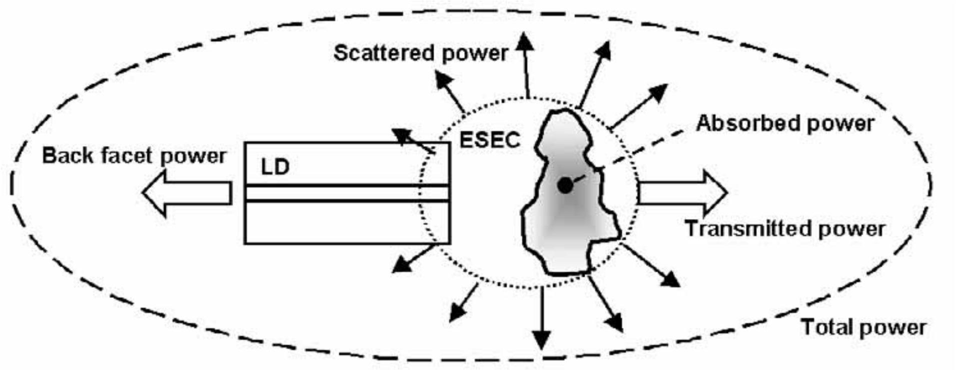

Figure 14. Optical output from the ESEC laser.

The output power via the front facet is thus the sum of the transmitted power, P_t, scattered power, P_s, and absorbed power, P_a: $P_f = P_t + P_a + P_s$. The total power emitted by the laser is the sum of the power emitted from the back facet and the power emitted from the front facet, i.e.: $P_{tot} = P_b + P_f = P_b + P_\mathrm{t} + P_a + P_s$ as illustrated in Figure 14. Correspondingly, as illustrated in Figure 15, the power P_I incident on the front facet of the laser will be divided in the ESEC into the reflected power, P_R, and the components of the front power, P_f: $P_I = P_R + P_f = P_R + P_t + P_a + P_s$, where the reflected power can be written as $P_R = R_{eff} P_I$.

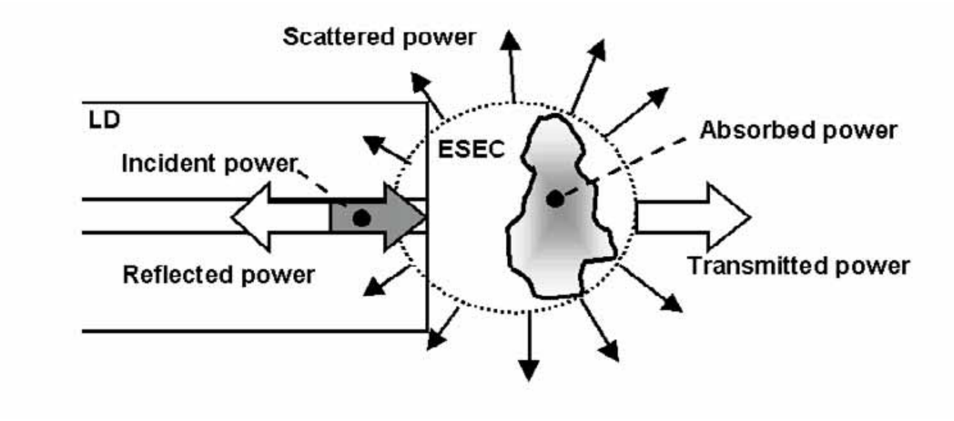

Figure 15. Optical powers at the laser facet and in the ESEC.

Of these quantities, P_b and P_f can be interpreted as the 'internal' laser quantities related to the power transfer out of the laser cavity. The powers, P_s, P_a and P_t are the 'external' quantities for the laser, which are related to the operation of the ESEC, but are seen by the internal laser cavity just via the front power, P_f. This is illustrated in Figure 16.

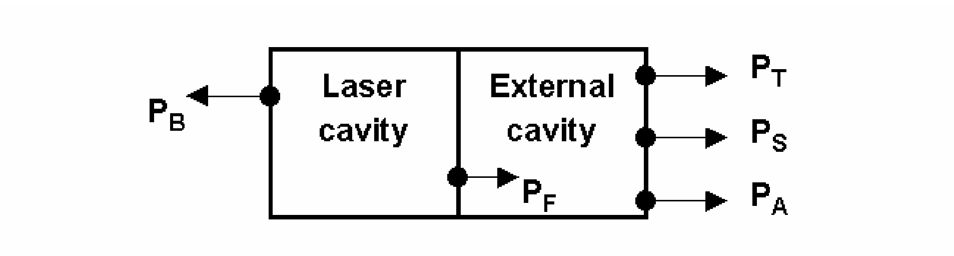

Figure 16. Internal and external components of the optical power.

3.3 Calculation of the effective reflectance

A key issue in the modeling of the operation of ESEC lasers is the calculation of the effective reflectance. We will next review the different ways to do the calculation. In Section 3.3.1, we will present the general aspects related to the calculation of the effective reflectance. After that we will describe simple one-dimensional models, a Gaussian model, and a model based on angular spectrum decomposition. Then we will use Fourier analysis and Babinet's principle to simplify some types of calculations. Finally, we present a method to calculate the effective reflectance from the finite difference time domain (FDTD) simulations of the electromagnetic fields.

3.3.1 General form

The main factors describing the effective reflectance are the reflectivities of the external reflector and the laser facet, and the coupling of the light from the external cavity back into the laser's internal cavity. Multiple reflections must often be taken into account. Also, the possible absorption in the cavity will influence the effective reflectivity.

The general form of the effective reflectivity on the laser facet can be given using the 'overlap integrals' between the electric fields of the waveguide mode propagating in the laser waveguide, $E_g(x, y; z)$, and the actual reflected field inside the laser cavity, $E_R(x, y; z)$. The overlap integral is the projection of the reflected field distribution to the waveguide mode, and can be written as an inner product between the two field distribution functions:

$$r_{eff} = K\int E_R(x,y)E_g^*(x,y)dxdy\,. \tag{56}$$

Here z is the direction of the propagation of light in the laser cavity, x is the direction perpendicular to the junction, and y is the direction of the junction (see Figure 6). The term K is a normalizing factor:

$$K = \left(\int\left|E_g(x,y)\right|^2 dxdy\right)^{-1}. \tag{57}$$

In the integral of Equation 56, the reflected field must be calculated using the given ('normalized') waveguide mode as the incident field. For a laser waveguide with multiple transversal modes, the projection of the reflected field must be calculated to each of the modes and using each of the modes as the incident field. This way all the cross-mode reflections will be taken into account. In the work presented in this thesis, we assume a single transversal mode operation.

As discussed in Section 3.2.1, the internal reflectance can often be separated from the effective reflectance. In such configurations the effective reflectance can be written as a coherent sum of the internal laser facet reflectance and the external reflectance: $r_{eff} = r_{int} + r_{ext}$, (cf. Equation (55)), where the external reflectance can be written as the overlap integral between the electric field of the externally reflected light and the waveguide mode:

$$r_{ext} = K \int E_{ext}(x,y) E_g^*(x,y)\,dxdy\,, \tag{58}$$

where E_{ext} is the electric field distribution of the externally reflected part of the electric field.

3.3.2 Simple one-dimensional models

Simple one-dimensional reflectance models are often used to calculate the optical feedback from the external cavities that are longer than the ESEC cavities. The general expression for the effective reflectance in the one-dimensional models is

$$r_{eff}(z_{EC}) = r_{\text{int}} + t_{\text{int}}^2 r_{er} f(z_{EC}) e^{i2\pi\frac{2z_{EC}}{\lambda}}\,. \tag{59}$$

Here $t_{int}^2 = (1 - r_{int}^2)$ is the transmittance of the front facet of the laser, r_{er} is the reflectance of the external reflector, λ is the wavelength, and $f(z_{\text{EC}})$ is some simple functional form for the coupling strength of the reflected light as the function of the external cavity length z_{EC}. The functional forms that have been used for the coupling strength are a constant value: $f(z_{EC}) = A$ [41, 48], a power law: $f(z_{EC}) = A\, z_{EC}^{-2}$, and an exponential law $f(z_{EC}) = A \exp(-D\, z_{EC})$ [28, 49, 50], where A and D are constants. In the longer external cavities, the change of the coupling strength is small for small changes in the external cavity length. There, when properly fitted, these laws are well suited for the analysis of the behavior of the external cavity lasers.

In the ESEC region, more sophisticated models have to be used. The rectangular aperture model has been used by several authors to model the diffraction effects related to the coupling of the feedback light from an external mirror [40, 3]. This model gives a relatively simple expression for the coupling coefficients. We will not go into the details of this model here (see [40, 3]), but we will continue directly to the Gaussian model.

3.3.3 Gaussian beams

The optical beam emitted by the laser can be approximated with an elliptic Gaussian beam, whose waist corresponds to the cross-section of the laser waveguide. If the external reflector in the ESEC does not change the wavefront significantly, the reflected beam will also be Gaussian. In such configurations, the effective reflectance can be calculated using the Gaussian overlap integrals [51, 52, 53, 54, 11]. Separating the internal reflection, we can write the effective reflectance from a simple planar external reflector as:

$$r_{eff} = r_{\text{int}} + t_{\text{int}}^2 r_{er} C_G\left(2z_{EC}, \lambda, \omega_{x0}, \omega_{y0}\right), \tag{60}$$

where C_G is a Gaussian overlap integral between the externally reflected and the incident Gaussian beams at the laser facet. In this model, the waveguide mode is assumed to have the same transversal distribution as the Gaussian beam at the beam waist, and the beam waist of the incident Gaussian beam is assumed to be located at the front facet of the laser. The semi-diameters of the elliptic Gaussian beam at the beam waist are ω_{x0} and ω_{y0} in x and y directions. Before returning to the laser facet, the reflected beam has propagated over a distance of $2z_{EC}$, where z_{EC} represents the external cavity length. Equation (60) was written for a single reflection from the external reflector. If the ESEC produces multiple reflections, the corresponding Gaussian overlap integrals and the reflection coefficients must be added to the equation, giving:

$$r_{eff} = r_{\text{int}} + \frac{t_{\text{int}}^2}{r_{\text{int}}} \sum_M \left(r_{er} r_{\text{int}}\right)^M C_G\left(2Mz_{EC}, \lambda, \omega_{x0}, \omega_{y0}\right). \tag{61}$$

Note that here the Gaussian overlap integral includes the phase term of the external reflection. The Gaussian overlap integral can be written in a simplified form [11]:

$$C_G = \frac{b_x b_y}{\sqrt{a_x a_y}}, \tag{62}$$

where

$$a_x = \omega_x^{-2}(z) + {\omega_{x0}}^{-2} + \frac{i}{2}\frac{2\pi/\lambda}{R_x(z)} \tag{63}$$

and

$$b_x = \frac{\sqrt{2}}{\sqrt{\omega_{x0}\omega_x(z)}}\exp\left\{\frac{-i}{2}\left[\frac{2\pi}{\lambda}z - \eta_x(z)\right]\right\}, \tag{64}$$

and similarly for a_y and b_y. Here, $\omega_x(z)$ is the beam radius of the Gaussian beam, and $R_x(z)$ is the wavefront radius of the Gaussian beam in x direction after a propagation of the distance z from the beam waist. The term $\eta_x(z)$ is the 'additional' Gaussian phase term. The functional forms of these terms are [55]:

$$\omega_x^2(z) = \omega_{x0}^2\left(1 + \frac{z^2}{z_0^2}\right), \tag{65}$$

$$R_x(z) = z\left(1 + \frac{z_0^2}{z^2}\right), \tag{66}$$

and

$$\eta_x(z) = \tan^{-1}\left(\frac{z}{z_0}\right), \tag{67}$$

where

$$z_0 = \frac{\pi\omega_0^2}{\lambda}. \tag{68}$$

3.3.4 Fourier optics

Fourier optics (see e.g. [56]) are suited for calculation of the effective reflectance, if the external reflector structure can be approximated to be composed of planar objects. Fourier optics are based on the application of the angular spectrum decomposition of the scalar electric field to model the free-space propagation of the field. The propagation can be calculated between two parallel observation planes. If the electric field has a well-defined frequency of harmonic oscillations, the field distribution on any observation plane can be related to the angular spectrum of the field (i.e. the amplitudes of the field in different propagation directions) by applying a Fourier transform to the field distribution. Each of the angular components of the field experiences a different phase-change in the propagation through a given distance. The inverse Fourier transform of the propagated field components will give the spatial distribution of the scalar electric field on the given final observation plane. The free space propagation can be written in the Fourier space (angular decomposition space) as a product between the electric field components, $\hat{E}(f_x, f_y) = \mathbf{F}(E(x, y))$ ($\mathbf{F}$ being the Fourier transform operator, and f_x and f_y are the spatial frequencies in x and y directions), and a transfer function, $T(f_x, f_y; z, \lambda)$:

$$\hat{E}_{final}(f_x, f_y) = \hat{E}_{initial}(f_x, f_y) T(f_x, f_y; z, \lambda). \tag{69}$$

The transfer function T is given as (see e.g. [56] p. 60)

$$T(f_x, f_y, z, \lambda) = \begin{cases} \exp\left[i2\pi \frac{z}{\lambda} \sqrt{1 - (\lambda f_x)^2 - (\lambda f_y)^2} \right], \sqrt{f_x^2 + f_y^2} < \frac{1}{\lambda} \\ 0, \quad \sqrt{f_x^2 + f_y^2} \geq \frac{1}{\lambda}. \end{cases} \tag{70}$$

The use of Fourier optics in the calculation of the optical fields in a complex system is done by using an alternating sequence of the free space propagation and the spatial ‘filtering’ of the fields. The spatial ‘filtering’ may affect both the phase and the amplitude of the fields. To use this method, each of the optical elements in the system has to be able to be modeled using a thin element approximation. In the thin element approximation the phase and the amplitude of the electric field is only locally changed by the element. The effect of the optical element can thus be presented as a filtering function, $F(x, y)$. The electric field after the filtering will be the product of the filtering function and the initial electric field:

$$E_{final}(x,y) = F(x,y)E_{initial}(x,y)\,. \tag{71}$$

We have used the Fourier optics to numerically calculate the reflected fields from planar external reflectors that cause phase and amplitude variations. The overlap integral is calculated numerically from the simulated field distributions. Specifically, we have used Fourier optics in the calculation of the effective reflectances from the data marks on an optical disk to model the direct semiconductor laser readout in Section 4.5. The next two sections will also give examples of the use of Fourier optics.

3.3.4.1 Overlap integral in Fourier space

Because the Fourier transform does not change the inner product of two functions, the calculation of the overlap integral of the electric fields can be done using either the angular spectrum or the spatial distribution of the two fields:

$$\begin{aligned} C &= \int E_1(x,y)E_2^*(x,y)dxdy \\ &= \int \hat{E}_1(f_x,f_y)\hat{E}_2^*(f_x,f_y)df_x df_y, \end{aligned} \tag{72}$$

where $\hat{E}_i = \mathbf{F}(E_i)$ for $i = 1, 2$. Some times it is easier to calculate the coupling coefficient in the Fourier space. As an example of that, we will use the Fourier space representation of the overlap integral in the calculation of the effective reflectance for the multiple reflections between the laser facet and a planar external reflector. Applying Equation (72) to an initial field, $E(z = 0)$, representing the waveguide mode, and a field propagated through a distance z_1, $E(z = z_1)$, we get

$$\begin{aligned} C(z_1) &= K\int E(z=0)E^*(z=z_1)dxdy \\ &= K\int \hat{E}(z=0)\hat{E}^*(z=z_1)df_x df_y \\ &= K\int \left|\hat{E}(z=0)\right|^2 T^*(z=z_1)df_x df_y. \end{aligned} \tag{73}$$

The effective reflectance of the multiple reflections in the ESEC with the external cavity length z_{EC} can be calculated as a sum (cf. Equation (61)):

$$\begin{aligned} r_{eff} &= r_{\text{int}} + \frac{t_{\text{int}}^2}{r_{\text{int}}}\sum_{M=1}^{\infty}\left(r_{\text{int}}r_{er}\right)^M C(M2z_{EC}) \\ &= r_{\text{int}} + \frac{t_{\text{int}}^2}{r_{\text{int}}}K\sum_{M=1}^{\infty}\left[\left(r_{\text{int}}r_{er}\right)^M \int\left|\hat{E}(z=0)\right|^2 T^*(z=M2z_{EC})df_x df_y\right]. \end{aligned} \tag{74}$$

Since $T(Mz) = T(z)^M$, (see Equation (70)) the effective reflectance can be written as:

$$\begin{aligned} r_{eff} &= r_{\text{int}} + \frac{t_{\text{int}}^2}{r_{\text{int}}}K\sum_{M=1}^{\infty}\left[\left(r_{\text{int}}r_{er}\right)^M \int\left|\hat{E}(z=0)\right|^2 T^*(z=2z_{EC})^M df_x df_y\right] \\ &= r_{\text{int}} + \frac{t_{\text{int}}^2}{r_{\text{int}}}K\int\left|\hat{E}(z=0)\right|^2 \sum_{M=1}^{\infty}\left[r_{\text{int}}r_{er}T^*(z=2z_{EC})\right]^M df_x df_y \\ &= r_{\text{int}} + \frac{t_{\text{int}}^2}{r_{\text{int}}}K\int\frac{\left|\hat{E}(z=0)\right|^2}{1-r_{\text{int}}r_{er}T^*(z=2z_{EC})}df_x df_y. \end{aligned} \tag{75}$$

This is a closed form presentation of the effective reflectance for any field form *E* in the case of the multiple reflections between the laser facet and a planar external reflector.

3.3.4.2 Babinet's principle

Babinet's principle is a superposition principle of electromagnetic fields. According to Babinet's principle, if a space is filled with two electric fields, E_1 and E_2, the total electric field in the space is the sum of the two fields $E = E_1 +$

E_2. Now, from Babinet's principle and the linearity of the field propagation equation (69) follows a superposition principle for the propagated scalar electric fields. It states the following: Let E_1 and E_2 be the distributions of the scalar electric fields at an observation Plane 1 and let E'_1 and E'_2 be the corresponding fields propagated to Plane 2 (i.e. there is a propagation relation between E_1 and E'_1 and between E_2 and E'_2). Then if we define a field $E = A\ E_1 + B\ E_2$, the corresponding field propagated to Plane 2 will be $E' = A\ E'_1 + B\ E'_2$ (see Figure 17).

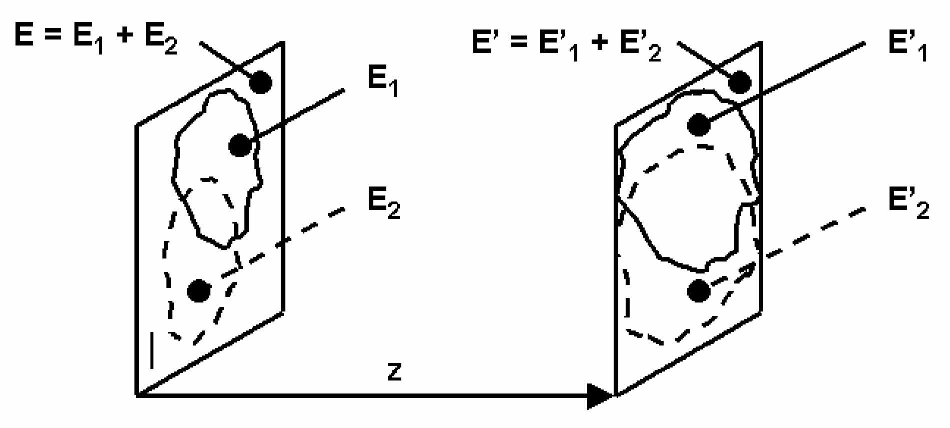

Figure 17. Illustration of the partial electric fields.

If we now take an overlap integral between E' and some given field distribution, E_g, we see that

$$\begin{aligned} C &= \int E' E_g^* dxdy \\ &= \int AE'_1\, E_g^* dxdy + \int BE'_2\, E_g^* dxdy. \end{aligned} \tag{76}$$

Using the notation

$$C_i = \int E'_i\, E_g^* dxdy, i = 1{,}2\,, \tag{77}$$

we get

$$C = AC_1 + BC_2\,, \tag{78}$$

where C_1 and C_2 are the coupling coefficients for the fields E_1 and E_2 propagated from Plane 1 to Plane 2, and C is the coupling coefficient for the field $E = A\,E_1 + B\,E_2$ propagated from Plane 1 to Plane 2. This relation means that the coupling coefficient on Plane 2 for a superposition of the fields defined on Plane 1 can be calculated as a weighted sum of the coupling coefficients of the partial fields propagated to Plane 2. The weighting coefficients of this sum are the same as the coefficients of the field superposition. This relation is useful, for example, when calculating the effective reflectance from an external reflector that is composed of multiple parts that may have varying reflectivity.

3.3.5 FDTD calculations

Finally, we will present a method to determine the effective reflectance from an arbitrary ESEC structure. The method uses finite-difference time-domain (FDTD, see e.g. [57]) calculations to define the optical field reflected back into the laser waveguide from the ESEC. The FDTD method is based on solving the Maxwell's equations using discrete spatial and temporal coordinates in the simulation. In the FDTD calculation, the ESEC may contain small metallic apertures and/or other three dimensional structures, such as data marks on an optical disk. The only limitation is the size of the calculation grid (directly proportional to the computer memory required), which is dictated by the size and the physical complexity of the external cavity structure.

An FDTD model of an ESEC laser comprises a short portion of the laser waveguide (adjacent to the output facet) and the entire external cavity structure, which is comprised of the laser's output (front) facet and some closely spaced external reflecting entities. This structure is embedded in the FDTD calculation grid by determining the complex refractive index for each grid cell (i.e. each location in the calculation space). FDTD is a physical model in the sense that no phenomenological explanations (other than the idea of the refractive index and, of course, the Maxwell's equations) are needed for determining the behavior of light that propagates within the calculation volume. On the other hand, this means that we have to know the geometry and the optical properties of the materials contained in the modeled system.

The electromagnetic field is sourced from a chosen location in the laser waveguide; the source field fills the entire cross section of the waveguide and it should be properly apodized so that it corresponds to the transverse mode(s) of the waveguide. A complex-field ($E = E_i e^{i\omega t}$ instead of a real field: $E = E_i \sin(\omega t)$) source should be used, in order to obtain the phase information. As the FDTD calculation executes, the electromagnetic field spreads out from the source and propagates in the waveguide and in the external cavity. Some part of the field is reflected back toward the laser waveguide structure and a small part of that is coupled into the waveguide's guided mode(s).

One fundamental feature of the FDTD calculation is that it does not inherently separate the scattered field from the incident field. Nor does it separate the guided modes from radiating modes in the waveguide. The FDTD calculation produces the total electromagnetic field in the calculation grid, comprising all of these partial fields. We will now present a simple method to extract the reflectance information from this calculated total field distribution.

Let the total electric field distribution in the calculation grid be $E(x, y, z, t = t_{\mathrm{stop}})$. When determining the effective reflectance, we are only interested in the guided part of the electric field inside the laser waveguide. As in Section 3.3.1, this is obtained by taking the projection (overlap integral) of the total field in the laser waveguide to the guided mode(s) in the cross-sectional plane of the waveguide:

$$
\begin{aligned}
C(z,t) &= \int E(x,y,z,t) E_g(x,y)^* \, dxdy \\
&= C_I(z,t) + C_r(z,t) \\
&= \frac{1}{K} e^{i\omega t}\left(e^{-ik(z-z_0)} + r_{eff} e^{ik(z-z_0)}\right).
\end{aligned}
\tag{79}
$$

Here E is the total field, E_g is the transverse profile of the guided mode(s) and C is the coupling coefficient for the total field given as the function of the z position in the waveguide. The coordinates are such that z-axis is parallel to the guiding direction of the waveguide (cf. Figure 6). Equation (79) shows that the guided part of the field is a coherent sum of the incident ($C_I = 1/K \exp[i\omega t - ik(z_0 - z)]$) and the reflected ($C_r = 1/ K\, r_{eff} \exp[i\omega t + ik(z - z_0)]$) waves, where ω is the angular frequency and z_0 locates some reference plane, where the effective reflectance will be calculated. The term K is the normalization factor defined in Equation (57). To demonstrate that the effective reflectivity calculation works even for un-normalized fields, the term K is intentionally left out of the first form of Equation (79). The term $1/K = |C_I|$, thus represents an arbitrary field strength of the guided mode.

For harmonic fields, C is a complex valued function, the values of which form an origin-centered ellipse in the complex plane. The lengths of the major and the minor axes of this ellipse (i.e. the extreme absolute values of C) are:

$$\begin{aligned} |C_{\max}| &= |C_I| + |C_r| = \left(1 + |r_{eff}|\right)|C_I| \\ |C_{\min}| &= |C_I| - |C_r| = \left(1 - |r_{eff}|\right)|C_I|, \end{aligned} \tag{80}$$

where, in the last equality, $|C_r| = |r_{eff}||C_I|$ has been used. Now, using Equation (80) we see that the modulation, M, of $|C(z, t)|$ (as a function of z) directly gives the amplitude of the electric field reflectance:

$$M = \frac{|C_{\max}| - |C_{\min}|}{|C_{\max}| + |C_{\min}|} = |r_{eff}| \tag{81}$$

The phase of the reflectance is determined by the locations of the minima and the maxima.

Various numerical errors may occur in the FDTD calculation. Thus, the values of C only approximate an ellipse. An easy way to fit an ellipse to this data is to use a pseudo inverse (Moore–Penrose inverse, see for example [58]) matrix method to obtain the coefficients for a set of equations

$$ax_n^2 + bx_n y_n + cy_n^2 = 1, \tag{82}$$

where $x_n = \mathrm{real}(C_n)$, $y_n = \mathrm{imag}(C_n)$ are the values of C at the pixel columns of the calculation grid, where $C_n = C(z = z_0 - n\Delta z, t)$ (pixel pitch is Δz) and a, b and c are the unknown coefficients of the polynomial that defines the ellipse. The matrix representation for Equation (82) is $XA = [1\ 1\ \ldots\ 1]^{\mathrm{T}}$, where $A = [a\ b\ c]^{\mathrm{T}}$, and

$$X = \begin{vmatrix} x_1^2 & x_2^2 & \cdots & x_N^2 \\ x_1 y_1 & x_2 y_2 & \cdots & x_N y_N \\ y_1^2 & y_2^2 & \cdots & y_N^2 \end{vmatrix}^{\mathrm{T}} . \tag{83}$$

Now, the polynomial factors, A, which give the 'least mean square' fit are given by

$$A = X^{+} \begin{vmatrix} 1 & 1 & \cdots & 1 \end{vmatrix}^{\mathrm{T}} = \begin{vmatrix} a = \sum_j X_{1j}^{+} & b = \sum_j X_{2j}^{+} & c = \sum_j X_{3j}^{+} \end{vmatrix}^{\mathrm{T}} , \tag{84}$$

where X^+ is the pseudo inverse of X such that $XX^+X = X$ and $X^+XX^+ = X^+$.

The lengths of the axes of the ellipse are given as the elements of the following diagonal matrix D

$$D = \mathrm{diag}(B) = \mathrm{diag} \begin{vmatrix} a & b/2 \\ b/2 & c \end{vmatrix} = \begin{vmatrix} C_{\max} & 0 \\ 0 & C_{\min} \end{vmatrix} , \tag{85}$$

where matrix B is chosen in such a way that $[x\ y]B[x\ y]^{\mathrm{T}} = ax^2 + bxy + cy^2 = 1$ yields the equation for the ellipse, i.e., Equation (82). Diagonalization of matrix B represents a coordinate transformation to a coordinate system in which the axes of the ellipse lie parallel to the coordinate axes. The values of $C_{\max}$ and $C_{\min}$ given by Equation (85) can then be inserted into Equation (81) to calculate the effective reflectivity.

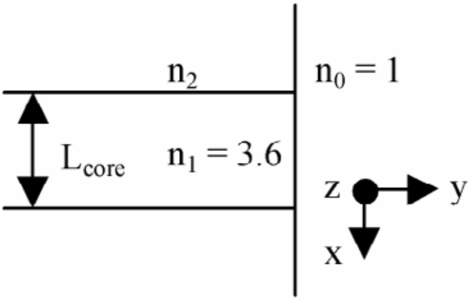

Figure 18. Laser-end model for calculating the reflectance from the end of the laser waveguide.

3.3.5.1 Validation of the FDTD method

To validate our model, the reflectance of a simple slab waveguide end facet was calculated with our method and the results were compared to those presented in references [59], [60], and [61], where the reflectance from the end of a slab waveguide has been analytically determined. The slab waveguide geometry is shown in Figure 18. The core thickness of the waveguide, the refractive index of the cladding material, and the polarization of the source were varied in the FDTD model. In Figure 19, the calculated reflectivity is compared with the results given in reference [61]. In this figure, the reflectivity of the fundamental mode is presented for TE (E_x, E_y, H_z) and TM (E_z, H_x, H_y) polarizations. Note that the polarizations are reversed in comparison to the previous papers ([59, 60, 61]). For each polarization, two curves are calculated. These represent two different cladding material indices $n_2 = 3.24$ and $n_2 = 3.492$, which correspond to the index difference of 10 % and 3 % between the cladding and the core materials. The index of the core is $n_1 = 3.6$. The results from our numerical method (circles) are in good agreement with the analytical results given in reference [61] (points). The general trend is that the numerical method gives somewhat higher reflectivity values than the analytical computation. This is most likely the result of numerical errors in the FDTD computations.

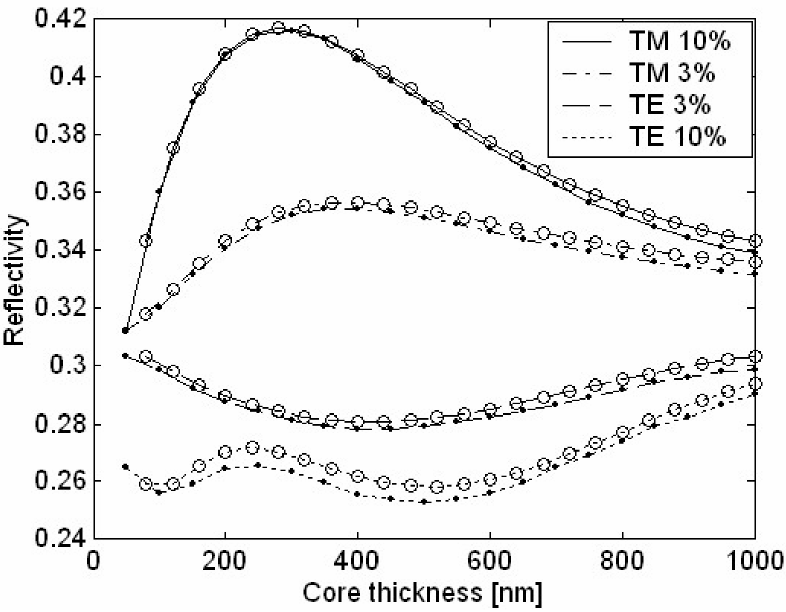

Figure 19. The intensity reflectivity of a laser facet calculated with the FDTD method (circles) is compared with the results given in reference [61](points).

In these calculations, the wavelength was 860 nm, the FDTD cell size was 10 nm, and the calculation space was 8 μm x 1 μm (x x y). With the smallest core thickness (80 nm), there were only 8 cells in the core region. To provide adequate spatial sampling for the waveguide geometry, the simulations were not performed with core thicknesses smaller than this. The optical fields inside the waveguide were sourced from a transverse plane located 600 nm from the laser facet. Free space (air) occupied a region extending 400 nm beyond the front of the facet. Berenger's PML (perfect matched layer) method [57] was used to truncate the calculation space.

4. Devices based on ESEC lasers

In the previous sections we discussed the physics related to extremely short external cavity lasers and the ways to model the laser operation. In this section we concentrate on the applications of the ESEC lasers. Section 4.1 gives an overview of the operation and possibilities related to ESEC laser sensors and other devices. In Section 4.2 we describe the characteristics of an ESEC laser with a planar external mirror. Section 4.3 describes a tunable laser based on the use of a miniature Fabry–Perot etalon as the external reflector. ESEC laser profilometry is studied in Section 4.4, and the last section, Section 4.5, describes the work done with the direct semiconductor laser readout in the optical data storage.

4.1 ESEC laser sensors and devices overview

ESEC lasers are very sensitive to the changes of the optical properties related to the external cavity. In the following sections, we will give some detailed examples of how that fact can be utilized in designing optical sensors and other devices based on ESEC lasers. In this section, we will review the operational principles of ESEC laser sensors and discuss the possibilities related to them.

4.1.1 The relationships between effective reflectance, optical power and lasing wavelength

As shown in the previous sections, the influence of the ESEC on the laser can be described via the effective reflectance of the ESEC. The main factors in the effective reflectance are the amplitude and the phase of the reflected light: $r_{eff} = |r_{eff}|\exp(i\phi_{eff})$. According to the theory presented in Sections 3.1 and 3.2, the amplitude of the effective reflectance affects 1) the modal gain of the laser, 2) the balance between the internal losses and the mirror losses in the laser, and 3) the balance between the output powers from the two ends of the laser. The phase of the effective reflectance affects only the oscillation mode structure of the laser light.

4.1.1.1 Optical power and the amplitude of the effective reflectance

The amplitude of the effective reflectance will directly affect the optical power of the laser. If we increase the amplitude of the effective reflectance starting from zero and assuming a constant injection current, the output power of the laser will first increase due to the increasing modal gain. Then at some point, assuming that the reflectivity of both laser facets is high enough, the internal losses start to dominate the mirror losses, and the optical output power of the laser starts to decrease. In the end, the optical power is absorbed by the laser rather than radiated out through the laser facets. When increasing the reflectivity, the increasing modal gain also leads to a decreasing threshold current and a bias voltage, the latter of which can be easily directly observed (see [26]).

The increasing effective reflectance also affects the balance of the optical powers radiated through the two ends of the laser. The higher the effective reflectance of the ESEC is, the more light is radiated out from the laser facet opposite to the ESEC. These phenomena are demonstrated in Figure 20, where in the left panel, the total optical power and in the right panel, the optical power radiated through the back facet of the laser, are shown as the function of the two reflectances of the laser facets (see also [10]).

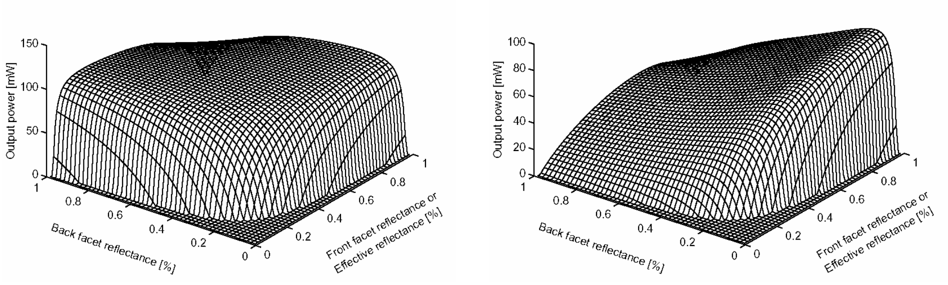

Figure 20: The optical output power of the laser as the function of the back and the front facet reflectances; (left) total power; (right) power from the back facet.

The sensitivity of the optical power on the changing amplitude of the effective reflectivity depends highly on the laser design. The amplitude of the effective reflectance usually depends on the internal reflectivity of the laser facet, the reflectivity of the external reflector structure, the possible absorption inside the external cavity, and the coupling efficiency of the light from the external cavity back to the internal laser cavity. Also, the interference between the external and the internal reflections will cause variations in the amplitude of the effective reflectivity. This interference is usually highly wavelength dependent and it is therefore described more deeply in the next section.

4.1.1.2 Wavelength dependency of the effective reflectance

If the amplitude of the effective reflectance varies with the wavelength, that will affect the distribution of the optical power of the longitudinal laser modes via affecting the modal gains. That will in turn lead to changes in the lasing wavelength compared to a free-running laser.

The effective reflectance is the coherent sum of the internal laser facet reflectance and the external ESEC reflectance, $r_{eff} = r_{int} + r_{ext}$ (see Equation (55); for the definition of internal and external reflections, see Figure 13). The interference between the internal and the external reflections on the laser facet usually generates the major part of the wavelength dependency of the effective reflectance, and therefore is the reason for the wavelength selectivity in many ESEC lasers. The phase difference and the balance between the amplitudes of the internal and the external reflections play important roles in many of the sensing applications.

Another source for the wavelength dependency of the effective reflectance is the spectral characteristics of the external reflector structure. The spectral selectivity of the external reflector is seen in the laser's operation via its effect on the modal gain.

4.1.1.3 Other possible dependencies of external reflectivity

If the effective reflectance is time dependent, that can lead to changes in the dynamic characteristics of the laser. In most of the sensor applications, the time scales of the physical phenomena to be sensed are much longer than the internal relaxation time scales of the laser. Therefore, the laser operation can usually be interpreted to be static. If needed, the time dependence of the effective reflectivity can be taken into account using a dynamical laser model (see e.g. [5]).

A more complex case, not fully covered by a simple effective reflectance model, would be a change in the wavelength inside the external cavity due to a Doppler shift or nonlinearities in the materials [43]. In that case, the light returning from the ESEC would be on a different wavelength than the incident light, which can potentially lead to a change in the lasing wavelength or possibly cause some dynamic operation of the laser (chirp). Additionally, the change in the polarization state of the light inside the ESEC could possibly introduce some additional possibilities to control the laser by affecting the coupling of light into the waveguide.

4.1.2 The use of ESEC lasers in sensor applications and other ESEC devices

As described above, the changes in the effective reflectance can change the operation point of the laser. The bias voltage over the laser junction, the optical output power and the wavelength spectrum of the laser are affected. In addition, the changes in the operation point may also change the noise characteristics of the laser light. These effects are summarized in Figure 21.

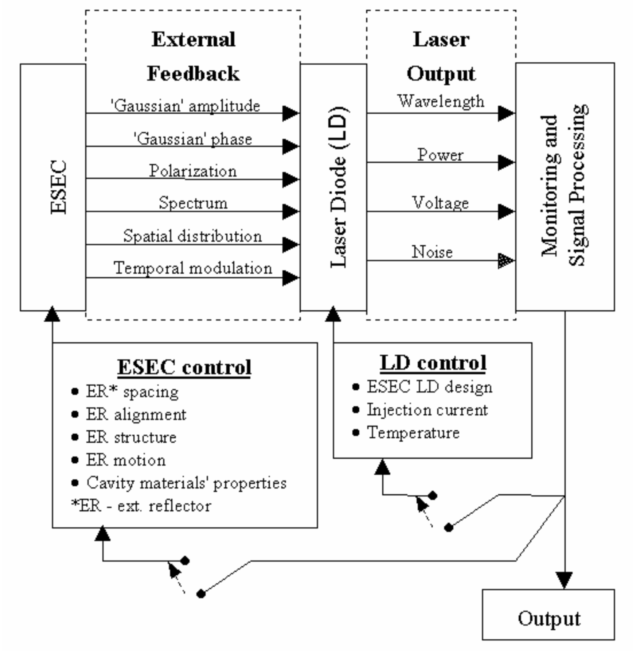

Figure 21. General concept of the ESEC devices.

Figure 21 also summarizes the operating principles of the devices based on the use of the ESEC lasers. The main parts of such a device are 1) a laser diode, 2) an ESEC structure and 3) a signal monitoring or processing unit. In addition to these, 4) a laser control unit and 5) an ESEC control unit are usually needed. The signal monitoring/processing unit can be connected back to the laser control and the ESEC control units to provide a feedback loop in order to dynamically adjust the operation of the device if needed.

The laser diode (1) can be of almost any type available. In this thesis, a Fabry–Perot semiconductor laser diode is assumed to be used in the ESEC laser configuration. However, there are several examples of other types of semiconductor lasers utilizing an ESEC as well. Especially, vertical cavity surface emitting lasers (VCSELs) have been extensively used in the ESEC configuration (see e.g. [62, 63, 64]). The laser control unit (4) is needed for setting the injection current level and often also for regulating the temperature of the laser device.

The ESEC (2) is composed of one or more external reflectors that provide the optical feedback to the laser. The reflectors can be planar or may have some more or less controlled spatial structure. The material in the cavity can be uniform or it may be composed of combinations of optically different materials to provide the desired functionality for the ESEC. The ESEC may also change temporally. The ESEC is usually controlled with an ESEC control unit (5). The external cavity length, the ESEC material properties, and the movement/ alignment of the external reflector may be controlled.

The optical and the electrical (voltage) signals provided by the ESEC laser can be monitored and used with monitoring and signal processing units (3). The bias voltage monitoring can provide the direct electrical input to the devices utilizing the ESEC laser, or controlling the laser or the ESEC. The changes in the optical power can be monitored with photo diodes or any other similar device. The wavelength of the light emitted by the ESEC laser can be monitored by any spectroscopic means. Optical spectrum analyzers may be used in the laboratory conditions but other spectral filtering methods may be useful in more sophisticated products. Also, integrated wavelength sensors (e.g. [65]) may prove to be useful when designing ESEC devices that utilize wavelength tuning effects.

Several examples of the use of ESEC laser devices can be found in the literature. Eliseev et al. [1] proposed the use of ESEC lasers for optical multi-wavelength communication already in 1970. ESEC configurations have been used for semiconductor laser stabilization (see e.g. [32, 33] and references therein). Various types of tunable lasers have been made using ESECs [66, 67, 68, 69, 11, 12, 54, 70, 71, 72, 62]. Various ESEC sensors have been demonstrated [7, 9, 73, 67, 40, 74, 48, 75, 76]. Most of these sensors are based on the monitoring of the changes in the optical power or the bias voltage. A special application for ESEC laser sensors has been the near field optical data storage [8, 10, 13, 77, 64, 78, 15, 50, 79, 80, 81, 82, 83, 84, 85]. The very small aperture lasers in the ultra short ESEC configurations have opened up the possibility to go beyond the conventional diffraction limit in the optical data storage and related near field sensing applications [86, 87, 8, 13, 15, 88, 89, 90, 91, 92]. Finally, the butt-coupling of the laser to a single mode fiber is a distinct natural application for the ESEC laser configuration [52, 71, 54, 93, 53].

4.1.3 The scope of the following applications

Most of the previous work with ESEC laser sensors has concentrated on using the power or the voltage variations as the monitored signal. The power monitoring and the voltage monitoring are relatively simple to realize and thus provide an easy way to get feedback on the laser's operation. The wavelength tuning has been mainly considered with tunable laser devices. In the following work in this thesis, we will concentrate on the wavelength tuning which is studied less than the other types of signals. We will analyze the ways to apply the wavelength tuning of the ESEC lasers in sensing applications and also further analyze some wavelength tunable laser configurations. In addition, we will apply the advanced modeling methods to study different ESEC configurations.

4.2 ESEC with a planar mirror

As a first example, let us consider an ESEC structure composed of an edge-emitting semiconductor laser and a planar mirror that is placed in close proximity to the front facet of the laser (see Figure 22). This system is the most conventional ESEC laser configuration, and therefore the following analysis of this system will reveal the most important design and operation principles of most of ESEC lasers. For the clarity of the text, we will call the system briefly a 'planar-mirror ESEC' or use the abbreviation PM-ESEC.

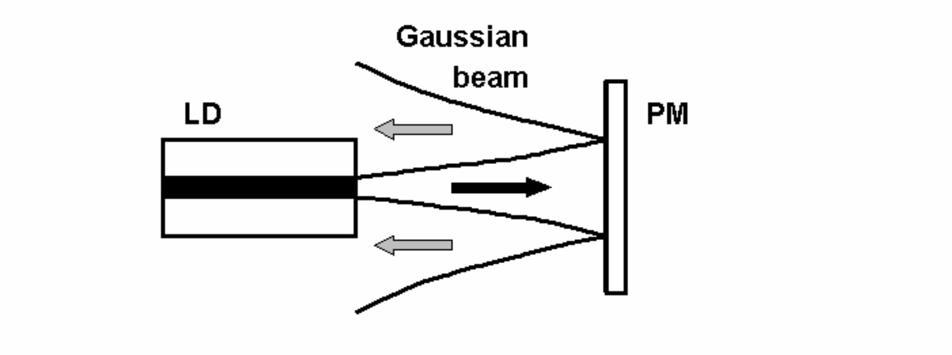

Figure 22. Schematic picture of a planar mirror (PM) ESEC laser.

We will study how the laser's operation point changes as a function of various parameters of the PM-ESEC system. These parameters are the separation between the laser and the mirror, the reflectivities of the back and the front facets of the laser diode, and the reflectivity of the mirror. The mirror tilt is not considered here (see e.g. [53]). As stated at the end of the previous section, the main emphasis in all of the examples is on the wavelength tuning effects, and therefore the interpretation of the changes in the laser's power and the bias voltage are not as deeply analyzed. We will first describe the theory and the numerical models used for analyzing the PM-ESEC lasers and then show some experimental results.

4.2.1 Theory and modeling of PM-ESEC

4.2.1.1 Effective reflectance

To calculate the effective reflectance for the PM-ESEC, we used a Gaussian beam approximation for the laser beam. This method is described in detail in Section 3.3.3. The effective reflectance is of the form given in Equation (61). An example of the calculated effective reflectance for a single wavelength ($\lambda = 1550$ nm) as the function of the external cavity length is shown in Figure 23. The (intensity) reflectivity of the front facet of the laser is assumed to be $R_{int} = 0.25$ ($r_{int} = 0.5$) and the (intensity) reflectivity of the external mirror is $R_{er} = 0.95$ ($r_{er} = 0.975$). The Gaussian beam waists are $\omega_{x0} = 2.5$ µm and $\omega_{y0} = 0.5$ µm. One of the main features of the effective reflectance curve is the half a wavelength (quasi-) periodicity. That is caused by the interference between the internal and the external reflections. The highest modulation in this interference pattern is reached at the cavity length where the internal and the external reflections are of equal magnitude. In the shorter cavity lengths, the external reflectance is dominating.

In addition to the amplitude, $|r_{eff}|$, the domination of the external reflectance is seen in the phase of the effective reflectance, ϕ_{eff}. When the external reflectance is dominating, the phase of the effective reflectance can have any value between 0 and 2π. This will lead to the continuous tuning of the longitudinal modes of the laser. If the internal reflectivity dominates, the phase of the external reflectance only oscillates close to the value determined by the phase of the internal reflectance. This is illustrated in Figure 24, where the phasor diagrams of the reflectances show the increasing phase variation as the amplitude of the external reflectance increases (see also [28]). The amplitude of the phase oscillations is given by $\phi_{eff,max} = \arcsin(|r_{ext}|/|r_{int}|)$, which can be deduced geometrically from the phasor diagrams. In the long external cavity lengths, the amplitude of the external reflectance decreases and therefore the effective reflectance approaches the internal reflectance.

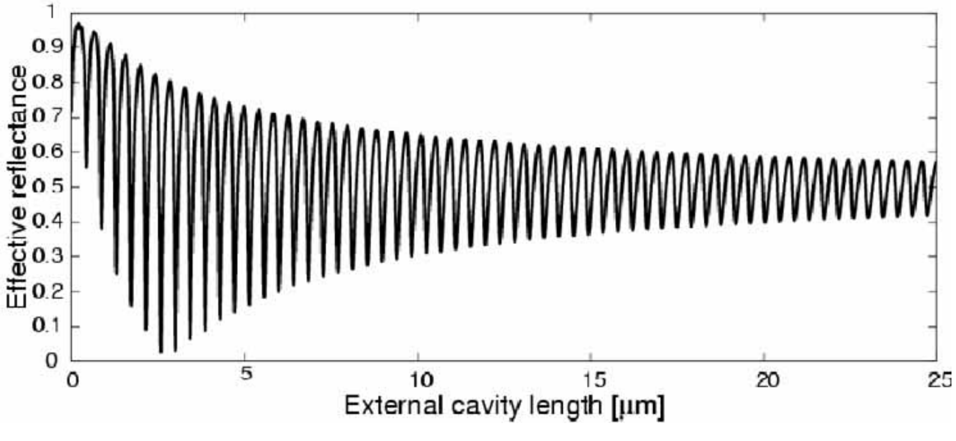

Figure 23. Effective reflectance of a PM-ESEC laser as the function of the EC length.

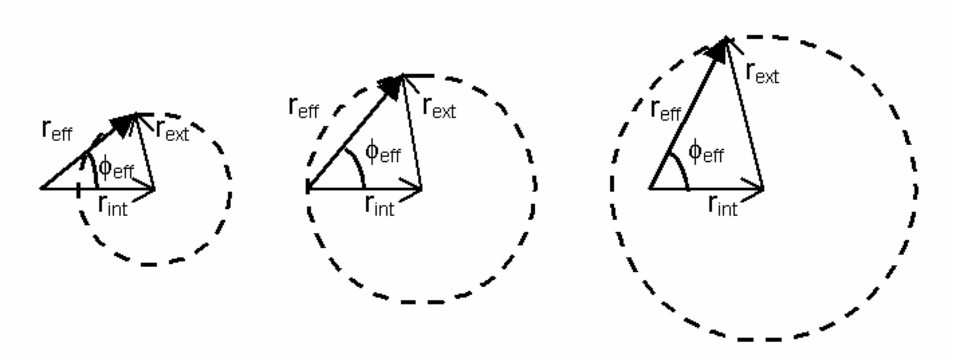

Figure 24. Illustration of the effective phase formation. Left: long external cavity, Center: equal internal and external reflectances, Right: short external cavity.

In Figure 25, the effective reflectance has been plotted as the function of the wavelength for an ESEC length of z_{EC} = 10 μm. The ESEC configuration is the same as in Figure 23. The maxima of the effective reflectivity curve correspond to the wavelengths of the external cavity modes in the system. The wavelengths of the modes are close to $\lambda_{EC,M} = 2z_{EC}/M$, where M is the order of the EC mode. However, due to the additional phase term ($\eta_{x,y}$ in Equation (64)) affecting the Gaussian beams close to the beam waist, the external cavity modes are somewhat shifted relative to the values given by $\lambda_{EC,M}$ above. The amplitude of the oscillations is dependent on the wavelength due to the stronger diffraction of the longer wavelengths.

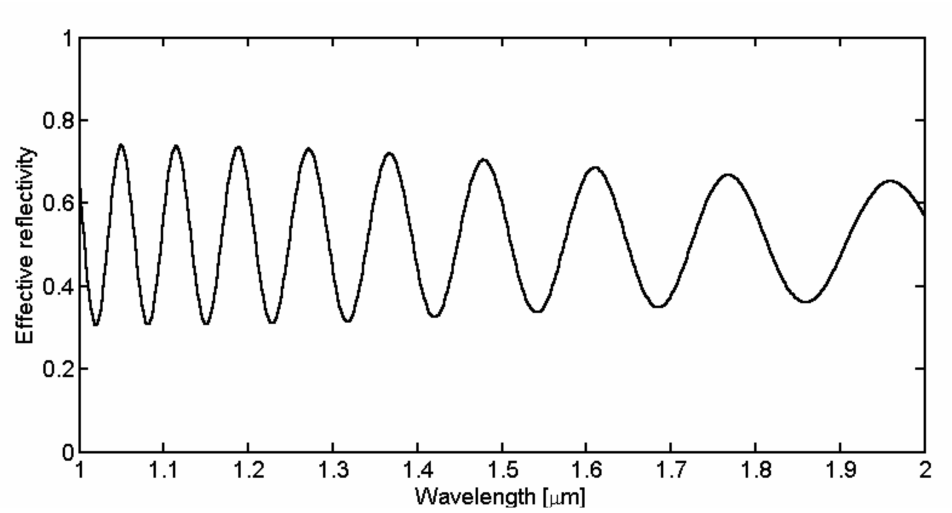

Figure 25. Effective reflectance spectrum of a PM-ESEC laser.

4.2.1.2 Applying the laser model

The insertion of the calculated effective reflectance to the laser model gives a theoretical estimation of how the ESEC laser behaves as the function of the external cavity length. Figure 26 shows the calculated power, the lasing wavelength and the mode structure for a PM-ESEC laser at $\lambda = 1550$ nm and at a constant injection current of $I = 100$ mA. The front facet (intensity) reflectance of the laser was $R_f = R_{int} = 5$ % and the back facet (intensity) reflectance $R_b = 80$ %. The gain spectrum used in the simulation corresponds to the measured gain of the 1550 nm 4QW laser shown in Section 2.1.2.3 Figure 4. This gain curve, fitted to the measured data, is shown in the gain/loss diagram in Figure 27 together with the original measured data and the calculated loss curves when the external cavity length is close to 10 μm.

The wavelength tuning is described in more detail in the next section and the power variations are discussed in the section after that. The role of the longitudinal modes will be discussed in the last section.

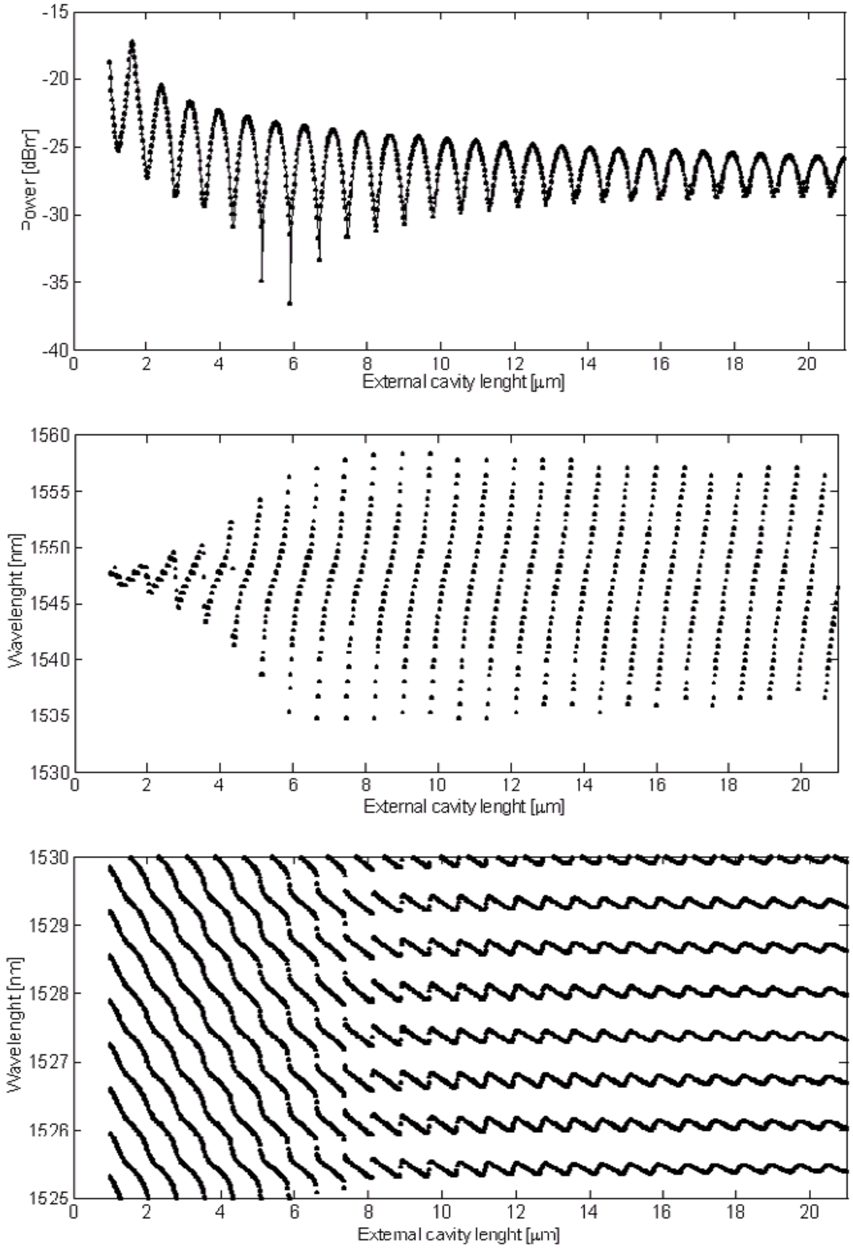

Figure 26. Simulated operation of a PM-ESEC laser as the function of the EC length; (top) total optical output power; (center) principal lasing wavelength; (bottom) wavelengths of the longitudinal modes.

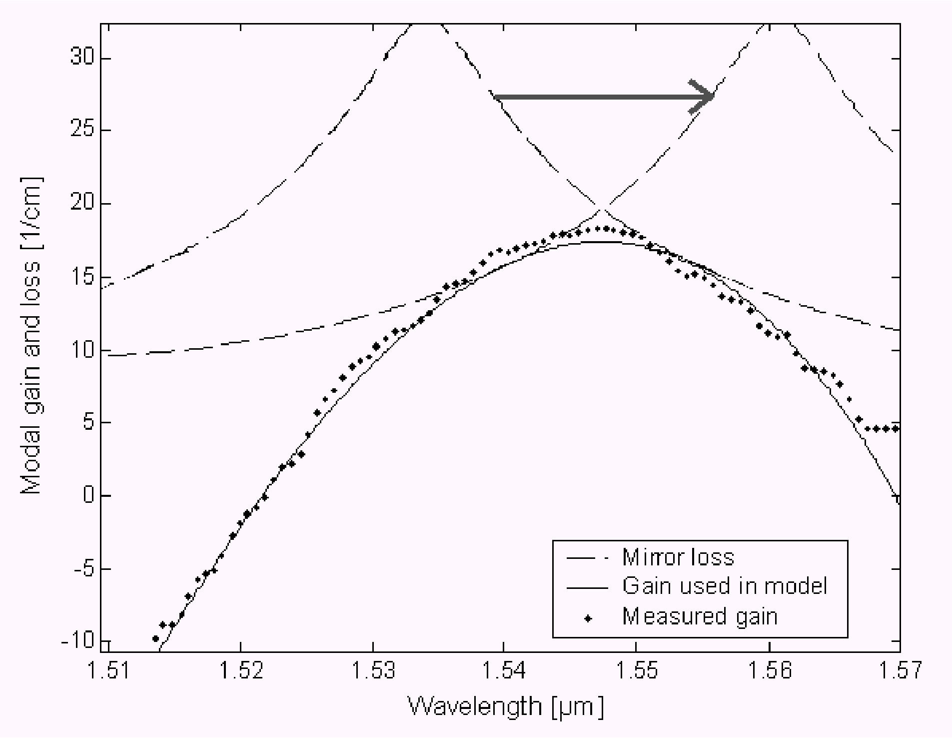

Figure 27. The measured material gain, the fitted gain used in the laser model, and the calculated loss terms (for two closely separated EC lengths) in the gain/loss diagram. The arrow shows the direction of the movement of the loss term with an increasing EC length.

4.2.1.3 The three regions of wavelength tuning

The wavelength tuning behavior of the PM-ESEC laser as the function of the external cavity length can be divided into three regions (I–III). These regions, shown in Figure 28, are:

I. Reduced tuning region

II. Non-linear tuning region

III. Linear tuning region.

The boundaries of these regions are not exact, but the characteristics are clear. When still increasing the external cavity length, the next clear transformation of the tuning behavior happens in the 'short external cavity' (SEC) region, when the wavelength separation of the longitudinal modes of the laser chip is close to equal to the wavelength separation of the longitudinal modes of the external cavity. That fourth region can be called (IV) a random tuning region, since the laser modes seem to 'lit and fade' in a random order, due to the 'aliasing' effects between the two sets of the cavity modes.

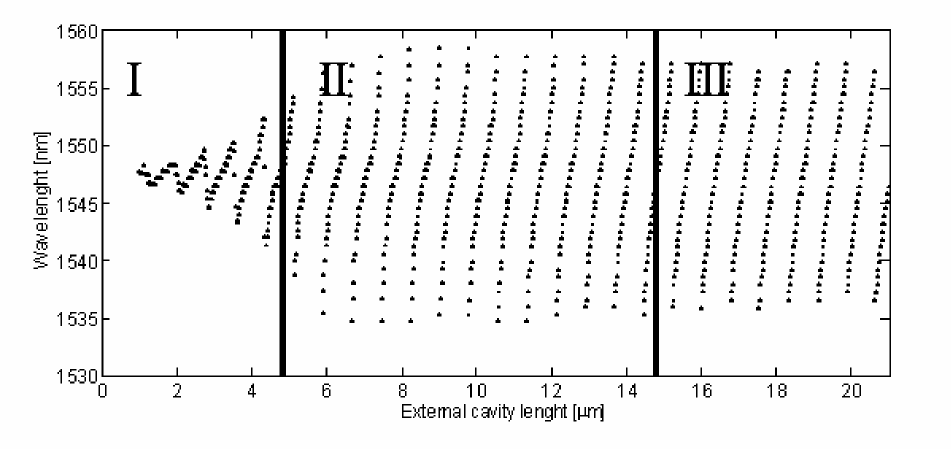

Figure 28. Three tuning regions overlaid with the simulated tuning curve of the PM-ESEC laser. I –reduced tuning region, II – non-linear tuning region, and III – linear tuning region.

The characteristics of the tuning regions I–III can be explained by looking at the gain/loss diagrams presented in Figure 29. As explained in Section 3.1.3, the principal lasing wavelength can be deduced from these diagrams by finding the wavelength of the minimum separation between the gain and the loss curves i.e. the touching point of the two curves. The power level of the laser, on the other hand, can be estimated from the height of the touching point in the diagram – the higher the gain must rise to touch the loss curve, the lower the power will be.

The first order effect of a gradual change in the external cavity length will be the movement of the loss curve to the left or to the right in the diagram (see Figure 27). The wavelength tuning can now be deduced by following the touching point of the two curves as the loss curve moves sideways in the diagram. After increasing or decreasing the external cavity length by half a wavelength, the loss curve has almost its original shape and place in the diagram, as expected on the basis of the one-half wavelength (quasi-) periodicity of the tuning curve.

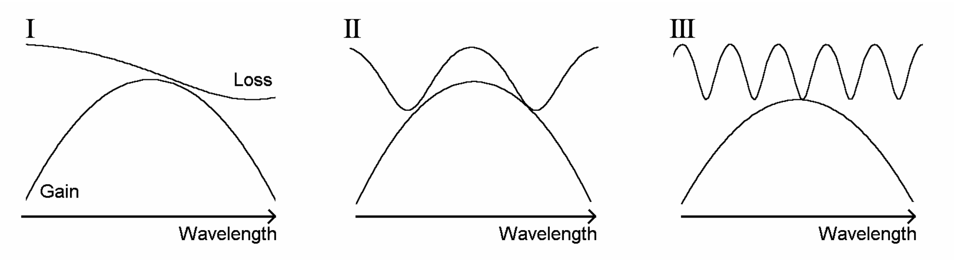

Figure 29. Gain/loss diagrams for the three tuning regions.

The reduced tuning region (I) starts from the zero external cavity length. It is characterized by the weak wavelength tuning that reflects the weak wavelength dependency of the effective reflectance. In this region the wavelength separation of the external cavity modes is larger than the effective gain band of the laser: $\Delta\lambda_{EC,M} > \Delta\lambda_g$, as shown in Figure 29. Because of the gentle shape of the loss curve, the lasing point in the gain/loss diagram will always be close to the top of the gain curve. When the external cavity length is gradually increased, the wavelength tunes up and down according to the direction of the slope of the loss curve. This explains the backward tuning also seen in Figure 28.

The largest tuning range is achieved in **the non-linear tuning region (II)**. In that region, the wavelength separation of the external cavity modes is close to equal to the width of the gain band $\Delta\lambda_{EC,M} \approx \Delta\lambda_g$ so that the gain curve has almost the same shape as the loss curve. The lasing point in the gain/loss diagram does not stay close to the top of the gain curve anymore, but it is not bound by the tips of the loss curve either. This movement of the lasing point relative to both curves leads to the non-linear tuning as the lasing point falls behind the movement of the loss curve.

In **the linear tuning region (III)**, the wavelength separation of the external cavity modes is clearly smaller than the spectral width of the gain band, $\Delta\lambda_{EC,M} < \Delta\lambda_g$. The lasing point stays always close to the tips of the loss curve, and the lasing wavelength therefore follows the external cavity modes. The linearity of the tuning versus the external cavity length is a direct consequence of the resonance condition $\lambda_{EC,M} = 2/Mz_{EC}$. The slope of the tuning curve is thus determined by the factor $2/M$, where M is the order of the EC mode.

Note that in region III, the tuning range is directly defined by the external cavity mode separation. In regions I and II, the tuning range is always less than the wavelength separation of the external cavity modes i.e. the term ‘reduced tuning’ actually applies to both regions I and II.

4.2.1.4 Wavelength tuning range and the mirror reflectivities

The wavelength tuning of the laser depends on the wavelength separation of the external cavity modes as seen in the previous section, but also on the amplitude of the modes in the loss term. The factors affecting the amplitude are the reflectance of the front facet of the laser, the reflectance of the external mirror, and the external cavity length via the coupling of the reflected light.

Figure 30 presents the simulated tuning ranges for the PM-ESEC lasers operating at 1550 nm. The tuning ranges are presented as the function of the reflectance of the external mirror, R_{er}, and for various values of the internal laser facet reflectance, R_{int}. The external cavity length for these curves is about z_{EC} = 20 µm. According to the graph, the longest tuning range in this case is achieved with the external mirror reflectivity of $R_{er} \approx 70$ % for all the values of the internal reflectivity.

The influence of the external cavity length for the tuning is shown in Figure 31. In that figure the tuning range is plotted for various external cavity lengths as the function of the reflectivity of the external mirror, R_{er}. The internal reflectivity of the laser facet is $R_{int} = 5$ %.

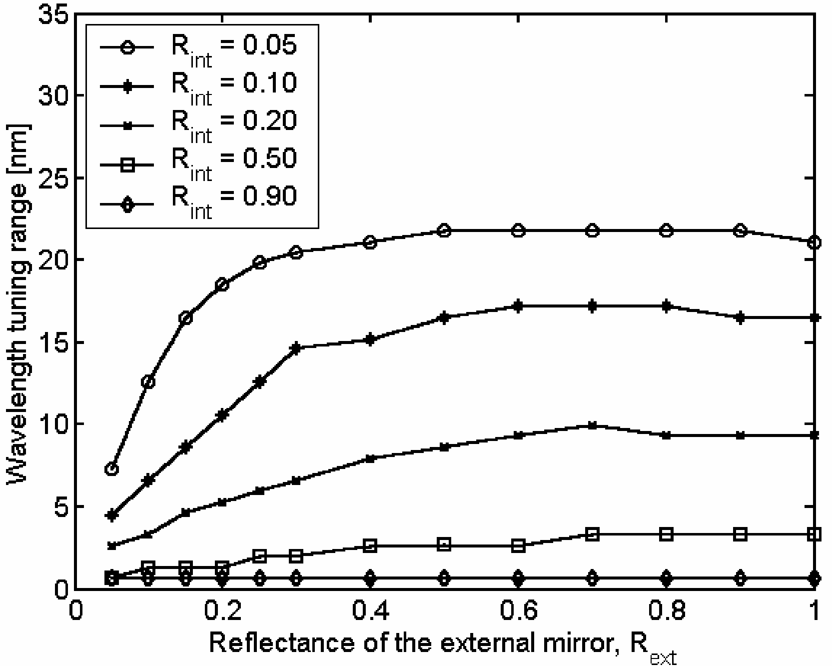

Figure 30. Wavelength tuning range of a PM-ESEC laser as the function of the intensity reflectance of the external mirror for several values of the internal laser facet reflectance.

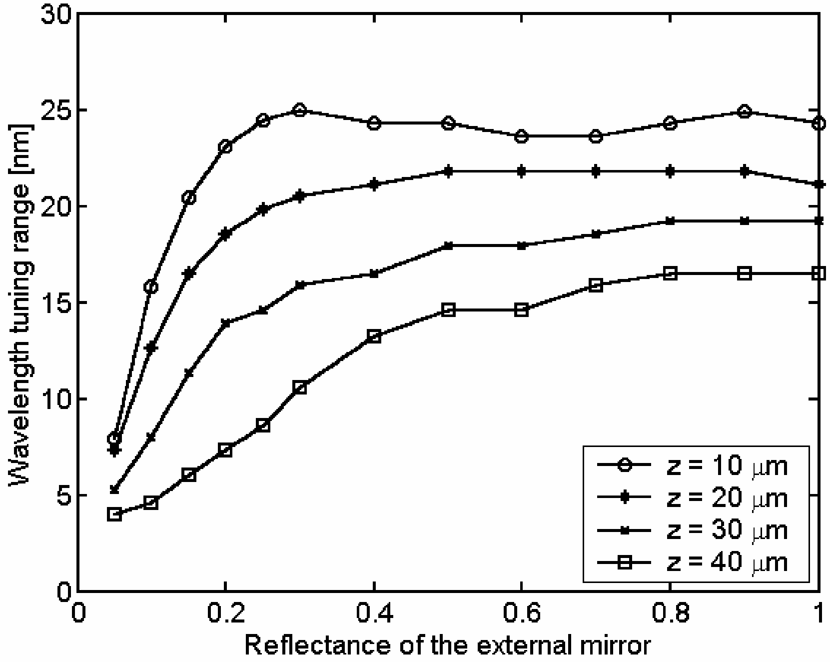

Figure 31. Wavelength tuning range of a PM-ESEC laser as the function of the intensity reflectance of the external mirror for several values of the EC length.

4.2.1.5 Power variations

The power of the laser in Figure 26 shows a half a wavelength quasi-periodicity as the function of the ESEC length reflecting the quasi-periodic behavior of the effective reflectance. The top envelope function of the power curve shown in Figure 26 – i.e. the maximum power per period – can be calculated by using the sum of the amplitudes of the internal and the external reflections as the effective reflectivity of the ESEC. In other words, the effective reflectance directly determines the top-envelope curve of the optical power. Understanding the depth of the power modulation, however, requires more analysis.

There are actually three factors that can affect the depth of the modulation: the maximal loss per period, the wavelength separation of the external cavity modes and the spectral shape of the gain. As stated in the previous section, the power emitted by the laser can be estimated from the height of the lasing point in the gain/loss diagram. The diagrams in Figure 29 can therefore be used to illustrate the power variations in the three regions.

In region I, where the gain spectrum is narrower than the separation between the longitudinal modes of the ESEC, the lasing point is always close to the top of the gain curve – i.e. the top of the gain curve closely follows the shape of the loss curve as the loss curve moves. In that case, the minimum power is determined by the minimum amplitude of the effective reflectance, given as the difference between the amplitudes of the internal and the external reflections: $|r_{eff,\ min}| = |(|r_{ext}| - |r_{int}|)|$. Usually this leads to large variations in the output power.

In region III, the laser's gain band is much wider than the wavelength separation of the adjacent external cavity modes. In that case, the power variation is actually determined by the shape of the gain spectrum and not by the shape of the loss term (or the effective reflectivity). This leads to a smaller variation in the power than what could be expected by just studying the effective reflectance values.

When the optical power variations are considered, **region II** is merely a transformation region between regions I and III.

4.2.1.6 How well can the power and wavelength be predicted?

The prediction of the power and the wavelength of the PM-ESEC laser is dependent on the knowledge of the laser's gain spectrum with various carrier densities and temperatures and the knowledge of the effective reflectance of the ESEC. Of these two factors, the effective reflectance can usually be predicted rather accurately. The gain, however, depends on so many factors that its prediction is always problematic (see [16]). The method that we have adopted here is to use a measured shape of the gain curve with the assumption that its shape does not change significantly at the different carrier density levels (i.e. gain levels) as long as we stay close to the threshold values of the free-running laser.

Now, assuming that the effective reflectance is well predicted and the gain spectrum contains some unknown factors, we can give some comments on the predictability of the laser's behavior in the three regions of tuning. First, the tuning can be predicted accurately only in the linear tuning region (III). In that region, the lasing wavelength closely follows the external cavity modes. Second, the power can be predicted rather well in region I, but also in region III when the external cavity length is large enough. In region I, the loss curve determines the lasing point, although in that case the height of the gain curve varies a lot which may weaken the predictability. In the long cavity length part of region III, the power is determined by the shape of the top of the gain curve and has only small variations. Third, the top envelope curve of the power can be rather well predicted since it is determined by the effective reflectance maxima.

4.2.1.7 Longitudinal modes

The longitudinal modes of the PM-ESEC laser are determined from the resonance equation (Equation (24)): $2nL/\lambda_m = m + \phi_{eff}/2\pi$, where λ_m is the wavelength for the m^{th} longitudinal mode, L is the length of the laser, n is the effective refractive index of the laser waveguide, and ϕ_{eff} is the phase of the effective reflectance. As discussed in Section 4.2.1.1, the phase of the effective reflectance can make full 2π revolutions as the function of the external cavity length if (and only if) the external reflectance dominates the internal reflectance (i.e. $|r_{ext}| > |r_{int}|$). This will lead to a continuous tuning of the longitudinal modes in the short external cavity lengths, which is clearly seen in Figure 26. In the longer external cavity lengths the modes just oscillate close to the wavelengths of the longitudinal modes of the free-running laser (i.e. the modes determined purely by the internal reflectance). The amplitude of these oscillations in the wavelength is determined by the amplitude of the phase oscillations (see Section 4.2.1.1), being $\Delta\lambda_m \arcsin(|r_{ext}|/|r_{int}|)/2\pi$. Here $\Delta\lambda_m = \lambda_m^2/(2nL)$ is the wavelength separation of the adjacent longitudinal modes.

The spectrum of the laser is a composition of the longitudinal modes. The optical power of each mode is principally determined by the modal gain. The change in the spectral distribution of the modal gains will directly affect the power emitted by each of the modes. This leads to the mechanism for the wavelength tuning of the PM-ESEC laser. A gradual change in the external cavity length will change the spectral distribution of the modal gain via changing the mirror losses of the laser. Due to their localization in the longer external cavity lengths and their slow motion in the short external cavity lengths, the longitudinal modes cannot keep up with the tuning of the modal gain distribution. Therefore, the change in the external cavity length will eventually lead into a change in the principal lasing mode (i.e. the mode with the highest modal gain) and thereby change the principal lasing wavelength (the wavelength with the most power). As a result, the lasing wavelength of the PM-ESEC laser is tuned discontinuously by ‘mode hopping’ between the longitudinal modes.

More than one longitudinal mode usually contributes significantly to the optical output power of the laser. The strength of the principal mode compared to the other modes depends on the modal gain difference as well as the electric current injected to the laser. The external cavity usually increases the side mode suppression compared to the free-running laser [94]. There are two factors that contribute to this phenomenon. First, the wavelength dependence of the loss term increases the modal gain difference between the principal mode and the side modes. Secondly, the maxima of the effective reflectance are always higher than the internal reflectance. This leads to a decreased threshold current of the laser, and therefore more current is used for the stimulated emissions. As stated before, the increased current strengthens the principal mode and therefore increases the side mode suppression.

4.2.2 Experiments on PM-ESEC

Figure 32 presents measurements that were done for a PM-ESEC configuration consisting of a 1550 nm edge-emitting InGaAsP/InP laser (Laser 1 in Table 1, p. 30) and a glass plate coated with a thin layer of gold that acted as the external mirror. The top row shows the power of the laser, the middle row shows the principal lasing wavelength, and the bottom row shows the wavelength behavior of the longitudinal modes of the laser. The glass plate was attached to a nanopositioning system that was used to adjust the external cavity length. The laser’s spectrum and the power were measured with an optical spectrum analyzer connected to the laser via a multimode optical fiber pigtailed to the back facet of the laser (the facet opposite the ESEC).

The external cavity length was increased in small steps, starting from the configuration where the laser almost touched the glass plate. The spectral data was collected on a computer and post-processed to get the power, the principal wavelength and the modal wavelengths shown in Figure 32. The power in the figure is the optical power detected by the spectrum analyzer and integrated over the monitored wavelength range, not the absolute total power emitted by the laser. The lasing wavelength is the principal wavelength, i.e. the wavelength bearing the maximal power on the monitored wavelength range. The modal wavelengths are determined from the local maxima of the spectrum. The horizontal axis should be considered as a relative change in the external cavity length, since the external cavity length at the starting point was not known exactly.

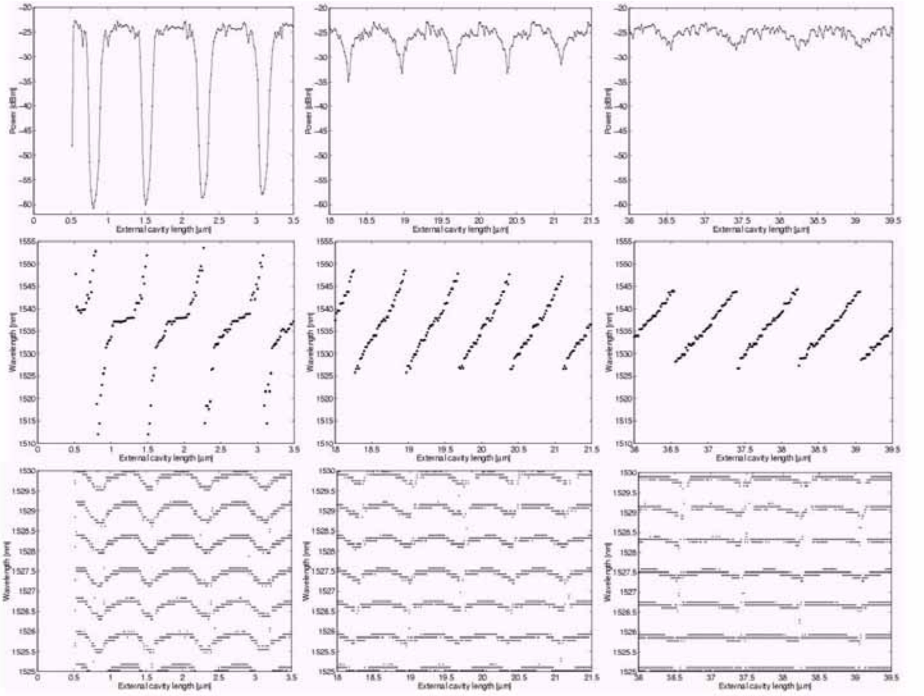

Figure 32. Measured operational characteristics of a PM-ESEC laser as the function of the EC length; (top) optical output power; (center) principal lasing wavelength; (bottom) wavelengths of the longitudinal modes.

Many of the features described in the theoretical analysis of the PM-ESEC laser are seen in Figure 32.

- The half a wavelength (quasi-) periodicity is clearly seen in all of the graphs.
- The power variation decreases towards the longer external cavity lengths.
- The wavelength tuning is highly non-linear in the short external cavities (non-linear tuning region II) and becomes more and more linear as the external cavity length increases (region III). The wavelength tuning range decreases with the increasing external cavity length.
- The longitudinal modes oscillate close to a certain value and the oscillation amplitude decreases with the increasing cavity length.

One feature that is not seen in these pictures is the reduced tuning region (region I). That, however, was observed in another measurement, done with a 790-nm GaAs laser (Laser 2 in Table 1, p. 30) with an otherwise similar measurement set-up. The tuning curve of that laser is shown in Figure 33. The other feature not seen in Figure 32 is the continuous tuning of the longitudinal modes, which means that the internal reflectance of the laser is the dominating factor in the effective reflectance at all the external cavity lengths. Both of these missing features can be explained if the actual external cavity lengths in this measurement were longer than that indicated by the horizontal axis of the figures. Quantitatively, Figure 32 shows a power variation of up to 35 dB and a wavelength tuning of 45 nm (with the 35-dB power variation).

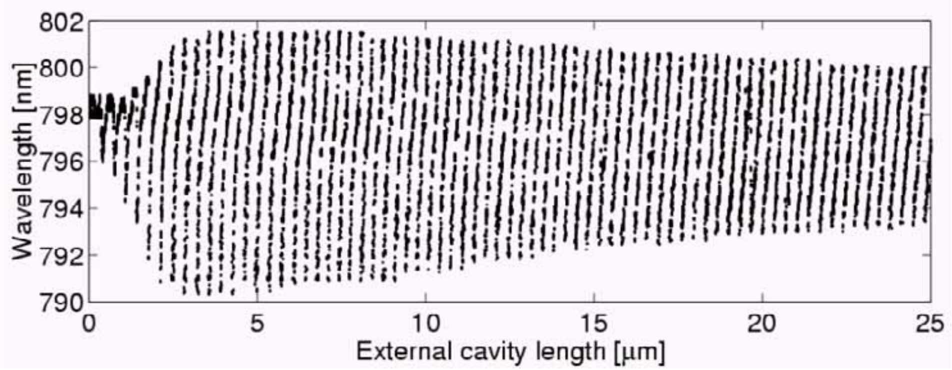

Figure 33. Measured tuning curve demonstrating the existence of the reduced tuning region.

4.2.3 Conclusions

We analyzed the characteristics of a PM-ESEC laser using our ESEC laser model and experiments, concentrating on the wavelength tuning phenomena. We showed and explained three tuning ranges of the PM-ESEC laser with distinct tuning characteristics and explained the related power changes. We also analyzed the influence of various design parameters on the tunability of the PM-ESEC system and discussed how well the laser model predicts the different characteristics of the PM-ESEC lasers.

4.3 Wavelength tuning with a micromachined Fabry–Perot etalon

In the previous section, we analyzed the ESEC laser with a planar mirror as the external reflector. In this section, we increase the complexity of the external cavity by using a tunable micromachined Fabry–Perot (FP) etalon as the external reflector (see Figure 34) [95, 72, 11, 12, 14, 96]. We will use the abbreviation FP-ESEC for this configuration. The tunable FP etalon consists of two mirrors separated with an air gap. The 'top' mirror can be moved relative to the stationary 'bottom' mirror to tune the etalon length (the thickness of the airgap). The idea behind this work was to see if the micromachined FP etalon could be used in the ESEC configuration to build a hybrid integrated tunable laser. Section 4.3.1 will review the modeling of the FP-ESEC laser, earlier published in [12, 11]. In Section 4.3.2 we will discuss the optimization of the FP-ESEC laser and finally, in Section 4.3.3 we will show the realization of the laser and give some experimental results.

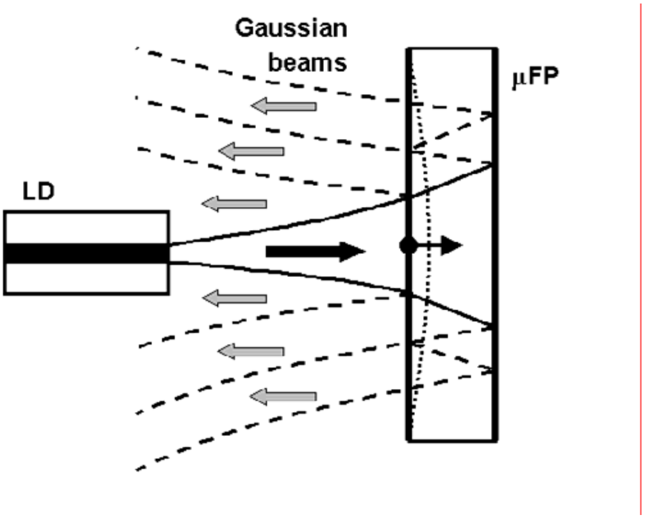

Figure 34. Schematic picture of the FP-ESEC laser with a micromachined Fabry–Perot etalon (μFP) as an external reflector. The arrow shows the tuning principle, based on the movement of the FP mirror adjacent to the laser diode.

4.3.1 Modeling the FP-ESEC laser

The modeling of the FP-ESEC laser is done according to the guidelines described in [11, 12]. In the modeling sense, the FP-ESEC consists of the front facet of the laser diode and two external mirrors located consecutively on the optical axis of the laser beam (see Figure 34). The mirror adjacent to the laser facet can be moved relative to the mirror farther from the laser to tune the FP etalon. The mirror farther from the laser has a fixed position relative to the laser.

4.3.1.1 Effective reflectance

As for the PM-ESEC, a Gaussian beam approximation (see Section 3.3.3) is used to calculate the coupling of the external reflections back into the laser cavity. Now, instead of the single reflection from the external mirror, we will have to take into account multiple reflections from the two mirrors forming the FP etalon. We can write the effective reflectance as [11]

$$r_{eff} = r_{\text{int}} + t_{\text{int}}^2 \left[r_{FP} C_G (2z_{EC}) + \frac{1-r_{FP}^2}{r_{FP}} \sum_{M=1}^{\infty} r_{FP}^{2M} C_G (2z_{EC} + M2l) \right], \qquad (86)$$

where, as earlier, r_{int} is the internal reflectivity of the laser's front facet, t_{int} is the transmittivity of the laser's front facet, r_{FP} is the reflectance of the mirrors in the FP etalon, C_G is the Gaussian coupling coefficient (see Equation (62)), l is the FP etalon length and z_{EC} is the external cavity length, i.e. the separation between the laser's front facet and the FP mirror adjacent to the laser.

Figure 35 shows the basic structure of the effective reflectance spectrum calculated for a wide range of wavelengths in a FP-ESEC configuration. This FP-ESEC configuration was designed to be used with a 1550-nm InGaAs laser diode and therefore the transmission band of the FP etalon is located close to 1550 nm. The (intensity) reflectivities of the FP mirrors in this example are 80 % ($|r_{FP}|^2 = 0.8$). The dotted line is the effective reflectance from a planar mirror (i.e. PM-ESEC) given for a reference.

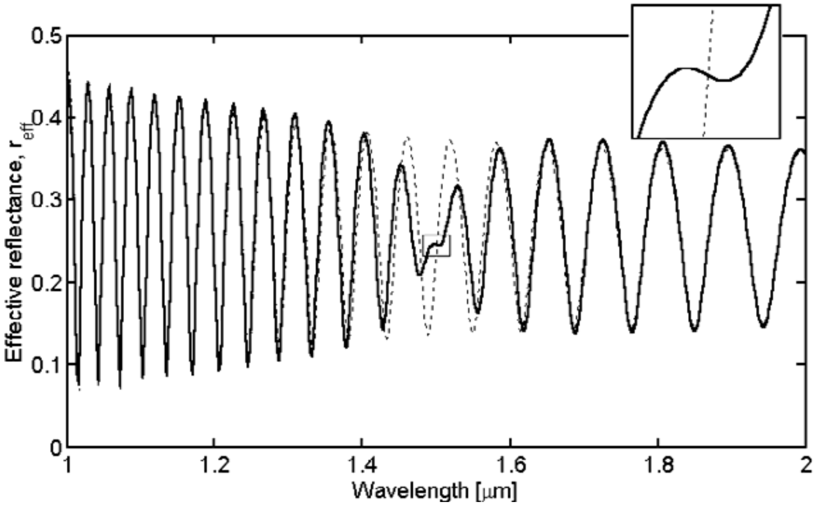

Figure 35. The effective reflectance spectrum of the FP-ESEC laser (solid line) compared to the PM-ESEC laser (dotted line). The inset shows a detail of the additional phase revolution at the resonance band of the FP etalon.

As in the case of the PM-ESEC lasers, the main feature of the effective reflectance spectrum is the external cavity modes shown as the oscillation of the effective reflectance. The wavelength separation between the EC modes is approximately $\Delta\lambda_{EC,\,M} = \lambda^2/\,(2\,z_{EC})$ (in this example, z_{EC} = 20 μm). The use of the FP instead of a regular mirror as the external reflector causes a disturbance to the external cavity mode structure. This disturbance is located at the transmission band of the FP etalon, i.e. at the resonance wavelengths of the etalon. In Figure 35 the disturbance is seen at the wavelengths close to 1500 nm.

The FP transmission band affects the effective reflectance in two ways. First, the amplitude of the external reflectance is notably decreased within the transmission band. That leads to a decrease in the amplitude of the oscillations produced by the external cavity modes (or, actually, by the interference between the internal and the external reflections at the laser's front facet). The other effect produced by the FP etalon is that the phase of the external reflection makes an additional revolution of 2π as the function of the wavelength inside the transmission band. The effect of the additional phase revolution is seen in the inset of Figure 35 where the additional oscillation at the center part of the transmission band is magnified.

Next, let us consider the tuning of the FP etalon length. Since only the mirror closest to the laser will move, the tuning of the FP will affect both the FP etalon length and the external cavity length (the distance between the moving mirror and the laser's front facet). As the FP etalon length decreases, the external cavity length increases. The effect of tuning the FP etalon length is illustrated in Figure 36, where the amplitude of the effective reflectance is presented in gray-scale as the function of the wavelength and the etalon length of the PF. The brightest tones in the gray scale correspond to the effective reflectance of 0.4 and the darkest tones to 0.1. The external cavity modes are seen in this picture as vertical bars. The FP transmission band is seen as a disturbance going diagonally through the image.

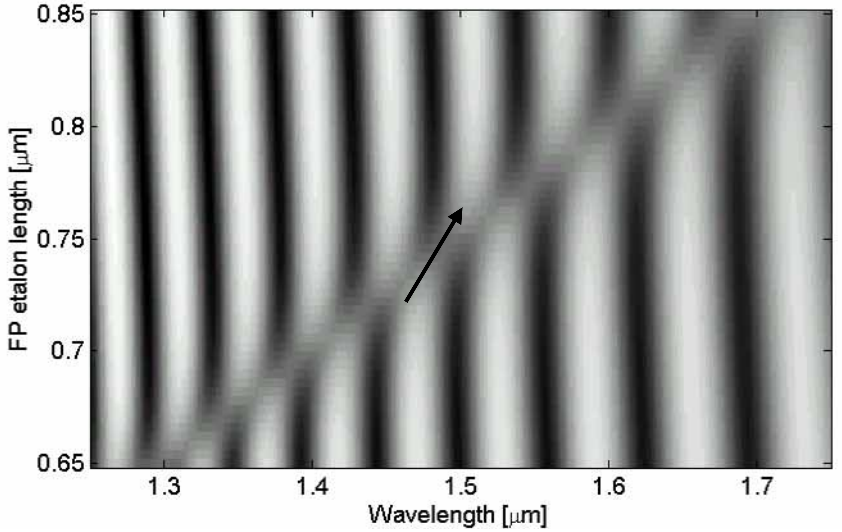

Figure 36. Effective reflectance diagram showing the amplitude of the effective reflectance (gray scale) as the function of the wavelength and the FP etalon length. The arrow shows the rapid tuning of an external cavity mode due to the additional phase revolution at the resonance band of the FP etalon.

The additional phase revolution at the FP resonance band causes the external cavity modes to rapidly tune towards the larger wavelengths at the resonance band when the FP etalon length is increased. This rapid tuning is indicated with an arrow in Figure 36. This phenomenon can be used to tune the lasing wavelength with a very small movement of the etalon mirror. If we make a larger movement with the mirror of the FP etalon, we can also see a wavelength tuning of the external cavity modes outside the FP resonance band. This tuning, illustrated in Figure 37, is essentially the same phenomenon as the external cavity mode tuning for the PM-ESEC laser. It is based on changing the phase of the external reflectance by changing the external cavity length. Figure 37 also shows a second FP resonance band sweeping over the wavelength range. Next we will discuss how these two ways of tuning the external cavity modes can be used to tune the lasing wavelength of the FP-ESEC laser.

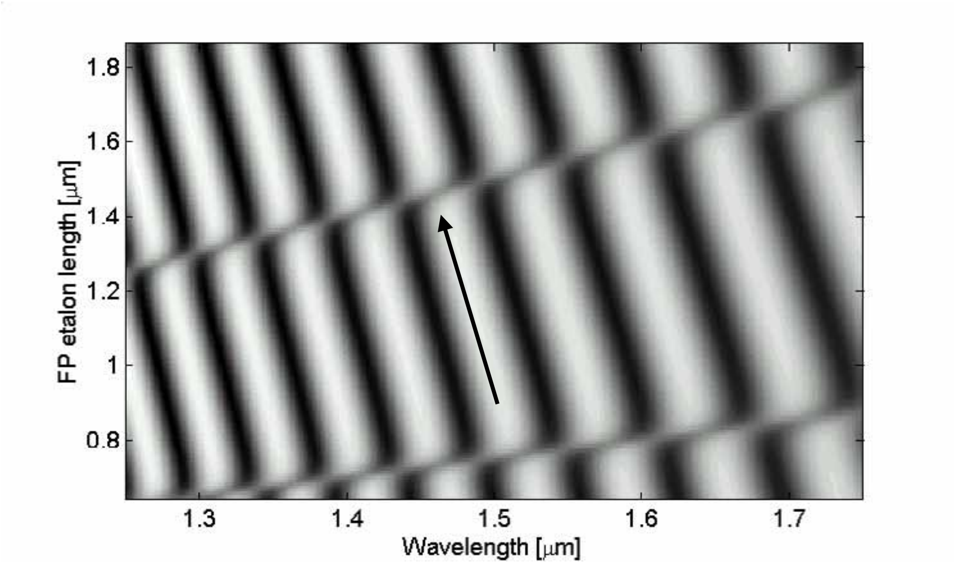

Figure 37. Effective reflectance diagram showing the amplitude of the effective reflectance (gray scale) as the function of the wavelength and the FP etalon length. The arrow shows the conventional tuning of an external cavity mode due to the gradual change of the EC length as the FP etalon length is tuned.

4.3.1.2 Tuning the laser with the external FP etalon

We can now insert the calculated effective reflectances in our laser model to study the wavelength tuning of the laser diode using the FP etalon as the external reflector. The laser used in the modeling and experiments is the same 1550 nm InGaAsP/InP laser (Laser 1 in Table 1, p. 30) as in the previous section and thereby the details of the model have already been told there. The analysis of the effective reflectance already revealed the two modes of tuning: 1) the rapid tuning due to the phase revolution inside the FP resonance band and 2) the conventional tuning with the mirror movement. Both of these tuning regions are shown in Figure 38 together with the simulated power variation.

The tuning with the mirror movement was analyzed rather deeply in Section 'PM-ESEC'. The only difference here is that the resonance bands of the FP will disturb the tuning at the regular intervals. To get the largest possible tuning range, the starting point of the tuning has to be chosen carefully.

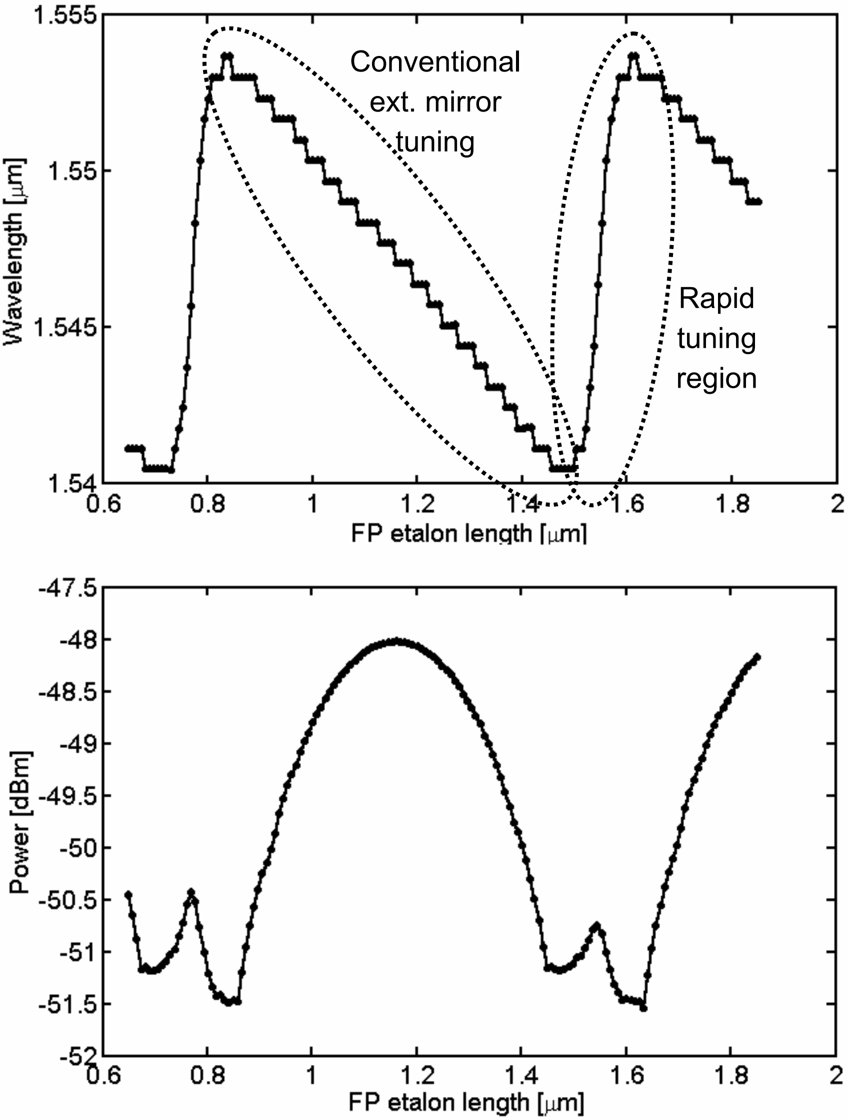

Figure 38. Simulated operation of the FP-ESEC laser as the function of the FP etalon length; (top) wavelength tuning; (bottom) total optical output power. The two types of tuning, the conventional mirror tuning and the rapid tuning, are highlighted on the wavelength tuning curve.

That is done by adjusting the external cavity length of the starting point of the tuning. The influence of the selection of the external cavity length is discussed in detail with the rapid tuning. The method of the wavelength tuning with the mirror movement in the FP-ESEC configuration hardly gives any advantage over the tuning achieved with the conventional PM-ESEC. Therefore, a transparent base element may be used instead of the stationary second mirror of the FP, if use of the FP geometry is desired.

The rapid wavelength tuning is shown in detail in Figure 39. In this case, a change of 0.1 μm in the external cavity length produces wavelength tuning of about 13 nm. It turns out that rapid tuning is very sensitive to various factors of the FP-ESEC configuration. The main factors are the external cavity length and the reflectivity of the mirrors of the FP etalon, but also the reflectivity of the front facet of the laser diode affects the tuning. The influence of the front facet reflectivity is very similar to the PM-configuration, and therefore that analysis is not repeated here. Now we'll have a look at the other two factors.

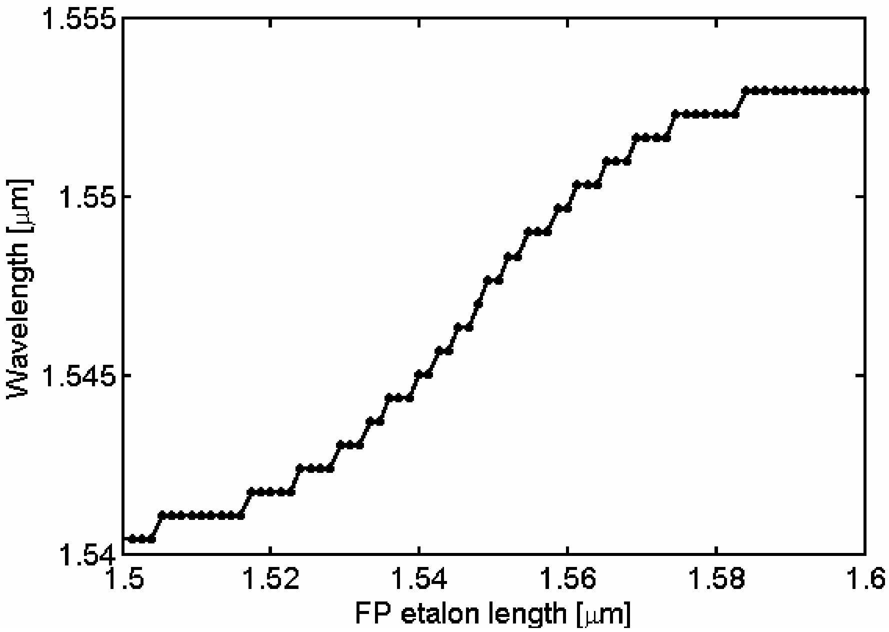

Figure 39. A detailed tuning curve for the rapid tuning region (R_{FP} = 0.8).

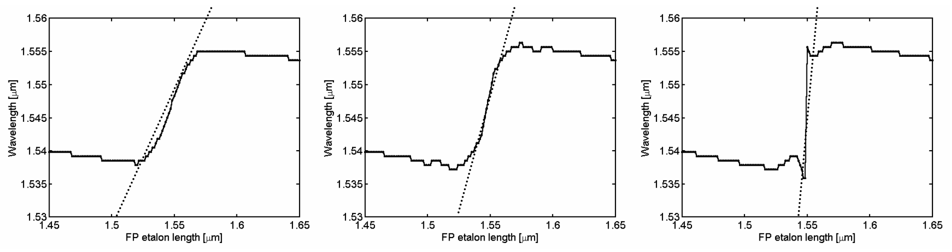

Figure 40. The influence of the reflectivity of the FP mirrors (the finesse of the FP) on the wavelength tuning in the rapid tuning region; from left to right: $R_{FP} = 0.95, 0.98, 0.99$.

4.3.1.3 Wavelength tuning and the finesse of the FP etalon

The reflectivity of the mirrors determines the finesse of the FP etalon. The higher the reflectivity, the higher the finesse, and the narrower the transmission band of the FP. The width of the transmission band also determines the pace of the additional phase revolution within the transmission band. For the higher values of the finesse, the phase revolution happens in a shorter range of wavelengths. In the FP-ESEC lasers, the higher finesse is seen as faster wavelength tuning as the function of the FP etalon length. This is illustrated in Figure 40, where rapid tuning is presented for three values of FP mirror reflectivities: left: R_{FP} = 95 %, center: R_{FP} = 98 %, and right: R_{FP} = 99 %. The 'speed' of tuning, highlighted with the dashed lines, increases with the increasing FP mirror reflectance.

Note that at high FP mirror reflectivities the laser's wavelength leaps to higher values without any intermediate steps; the 'continuous' tuning breaks down. This phenomenon can be understood by looking at the wavelength tuning curve overlaid with the effective reflectivity calculations shown in Figure 41. On the left, the reflectivity of the FP mirrors is 80% (low finesse), whereas on the right it is 99% (high finesse). For the low values of finesse, the transmission band of the FP is wide enough to both weaken the 'actual' external cavity modes and form a 'bridge' between the modes (see Figure 41 for the terminology). For the high values of finesse, the transmission band of the FP affects only a very narrow range of the wavelengths simultaneously, and therefore the EC modes are intact when the 'bridge' is formed between them. The gain is highest on the margins of the EC modes and not on the 'bridge', and therefore the lasing wavelength just jumps from one EC mode to the next.

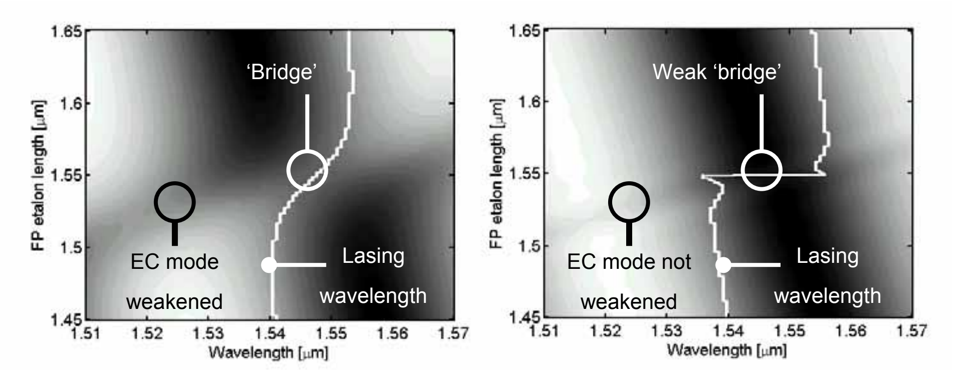

Figure 41. The tuning curves on the rapid tuning region overlaid with the effective reflectance diagram for the low finesse (left, R_{FP} = 80 %) and the high finesse (right, R_{FP} = 99 %) of the FP etalon. The 'bridge' formation and the EC mode weakening (or lack of them) can be used to explain the behavior of the rapid tuning for the low and the high finesse FP etalons.

The wavelength tuning range depends on the finesse of the FP. Figure 42 shows the tuning range of the FP-ESEC laser as a function of the reflectivity of the FP mirrors. This figure of the tuning range is actually valid for both the rapid tuning region and the conventional 'PM-tuning' region. The width of the tuning range is mainly determined by the steepness of the tuning curve in the rapid tuning region, depending on the finesse. This is illustrated in Figure 43, where the simplified tuning curves are presented for the conventional 'planar mirror (PM) tuning', the tuning with a high-finesse FP etalon and the tuning with a low-finesse FP etalon (cf. also Figure 40).

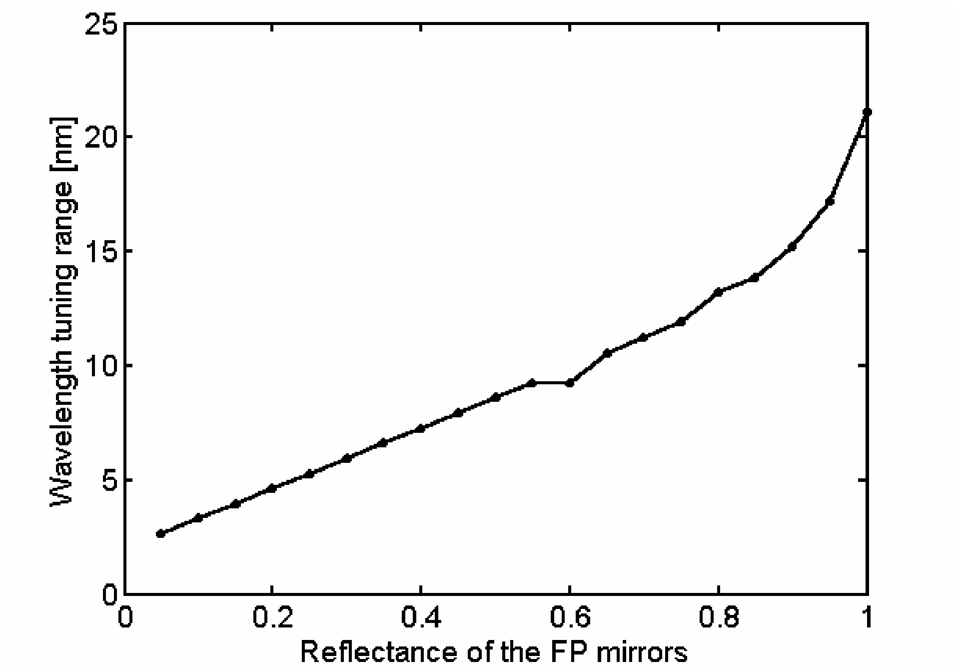

Figure 42. Wavelength tuning region as the function of the reflectance of the FP mirrors (for both tuning regions).

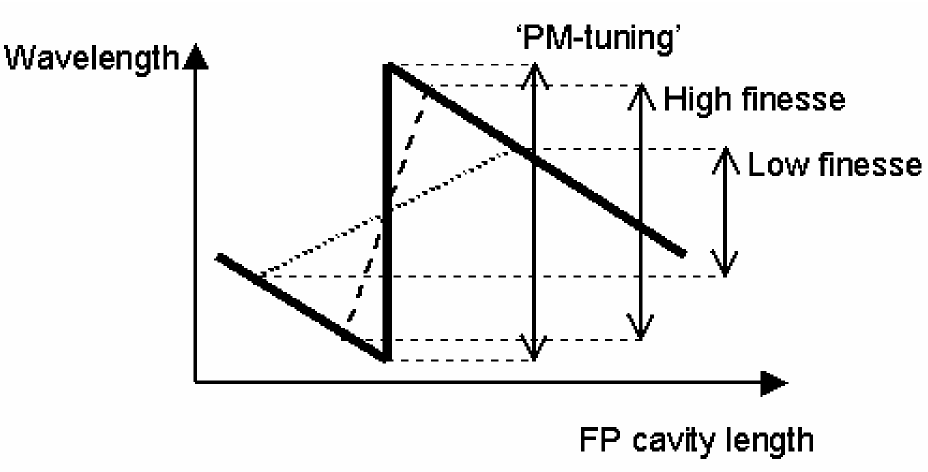

Figure 43. Illustration of the relation between the tuning range, the slope of the tuning (in the rapid tuning region), and the finesse.

4.3.1.4 Wavelength tuning and the external cavity length

Now let us look at how the external cavity length affects the wavelength tuning in the rapid tuning region of the FP-ESEC laser. The overall ‘large scale’ behavior of the tuning range with the increasing external cavity length is very similar to the PM-ESEC lasers, and therefore the analysis presented in Section 4.2 will not be repeated here. However, on a smaller scale, the wavelength tuning of the FP-ESEC laser is highly dependent on the fine-tuning of the external cavity length.

As seen in Figure 41, the rapid tuning of the wavelength of the FP-ESEC laser is based on the change of the lasing point from one external cavity mode to the next via a continuous path (the ‘bridge’) between the two modes. This ‘bridge’ is formed by the additional phase revolution of the external reflectance within the transmission band of the FP etalon. Now, the necessary conditions for the rapid tuning to occur are that with the increasing FP etalon length 1) the lasing wavelength must initially be in the EC mode on the short-wavelength side of the gain band of the laser and 2) the ‘bridge’ must be formed at the center of the gain band. Since the external cavity length determines the locations of the external cavity modes in the wavelength space, both of these conditions are affected by changing the external cavity length.

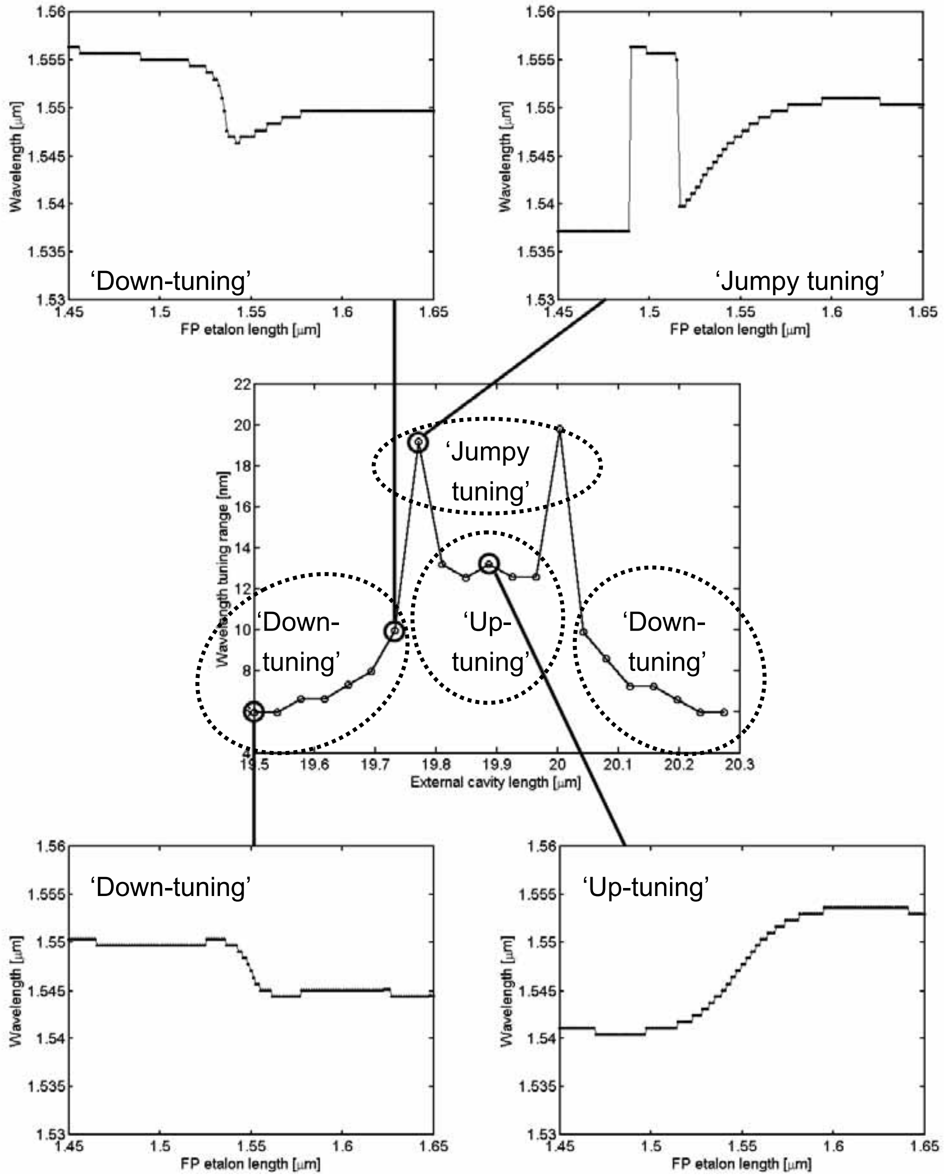

Figure 44. The influence of small changes in the EC length on the behavior of the rapid tuning. In the middle, the wavelength tuning range is plotted as the function of the EC length. One half – a wavelength cycle on the EC length is covered in the figure. The images on the top and bottom rows show examples of the tuning curves on various EC lengths. Three different types of tuning behavior can be distinguished: ‘up-tuning’ (preferred), ‘down-tuning’, and ‘jumpy tuning’. The preferred ‘up-tuning’ region covers only a small proportion of the EC lengths.

Figure 44 shows the wavelength tuning range as the function of the external cavity length on the rapid tuning region of the FP-ESEC laser. Included in the figure is a half a wavelength cycle of the external cavity length. Almost the same pattern is repeated outside the plotted area. Also included in the figure are samples of the tuning curves within the plotted range of the external cavity lengths.

Three different regions of the wavelength tuning are highlighted in the figure: 1) an '**up-tuning**' region, which, according to our definition, is the true 'rapid tuning' discussed in the previous sections, 2) a '**jumpy tuning**' region and 3) a '**down-tuning**' region. In the up-tuning region, the tuning starts from an EC mode in the shorter wavelengths and tunes up to the next EC mode as shown in Figure 45, where the tuning curve is overlaid with the gray-scale presentation of the effective reflectance. In the jumpy tuning region, the wavelength is jumping back and forth between the two EC modes. In the down-tuning region, the wavelength stays within one EC mode and is just somewhat disturbed by the FP transmission band sweeping over the mode. The up-tuning region is preferred due to the longest and smoothest tuning range.

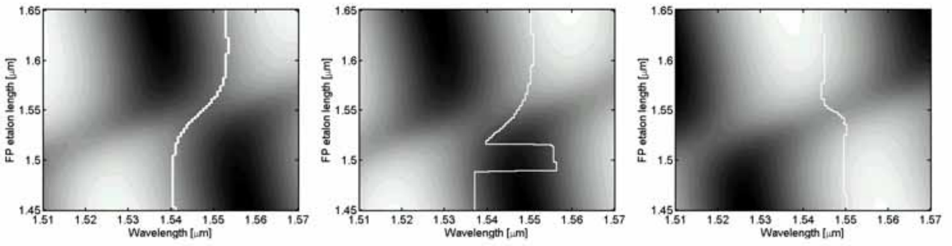

Figure 45. Up-tuning, jumpy-tuning, and down-tuning curves overlaid with the corresponding effective reflectance diagrams to explain the different tuning behaviors.

Figure 44 and Figure 45 are calculated for a low-finesse FP etalon with an 80 % mirror reflectance. Figure 46 shows the tuning range as the function of the external cavity length for a higher-finesse FP etalon. Here the FP mirror reflectance was 95 %. Three things have happened in this curve compared to the low-finesse configuration. First, the tuning range in the up-tuning region has increased. This was discussed in the previous section. Second, the tuning range in the down-tuning region has decreased. Third, the up-tuning range has narrowed, which is maybe the most important result in this analysis.

In the low-finesse configuration, the up-tuning region is about one fourth of the half-a-wavelength period, whereas, in the high finesse configuration, the up-tuning region is only about one seventh of the period. In the units of the external cavity length, this means that, in the low-finesse configuration, the FP must be positioned within ~200 nm range and, in the high-finesse configuration, within ~100 nm range in any one of the periods to achieve the rapid up-tuning. If the external cavity length is randomly selected, rather than actively adjusted, this means a probability of ¼ for a low-finesse configuration and the probability of 1/7 for a high-finesse configuration to end-up in the up-tuning region.

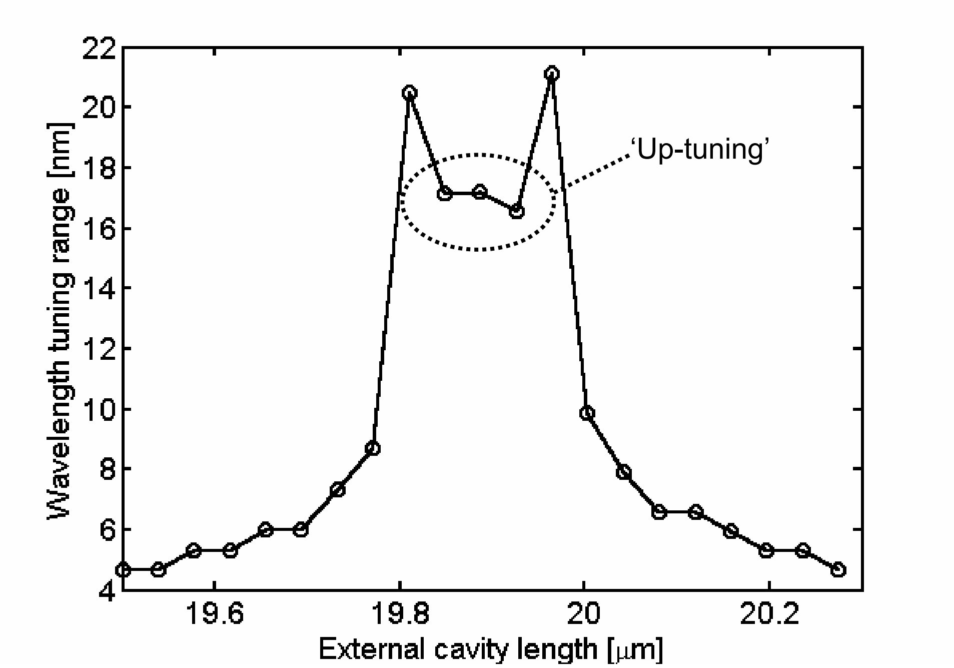

Figure 46. The tuning range as the function of the external cavity length for a higher-finesse FP etalon (R_{FP} = 95 %), cf. Figure 44, where (R_{FP} = 80 %).

Figure 47 shows one more issues related to the rapid up-tuning of the wavelength in the FP-ESEC laser configuration. The actual tuning range even within the up-tuning range is highly sensitive to the external cavity length. In Figure 47, the tuning curves are shown for the extreme ends of the up-tuning range for the low-finesse configuration. The change of 150 nm in the external cavity length leads to a shift of 5 nm in the tuning range, which is more than 1/3 of the total tuning range in this configuration. The analysis shows that the desired rapid up-tuning region is thus very difficult to find and regulate without an active and very accurate adjustment of the external cavity length.

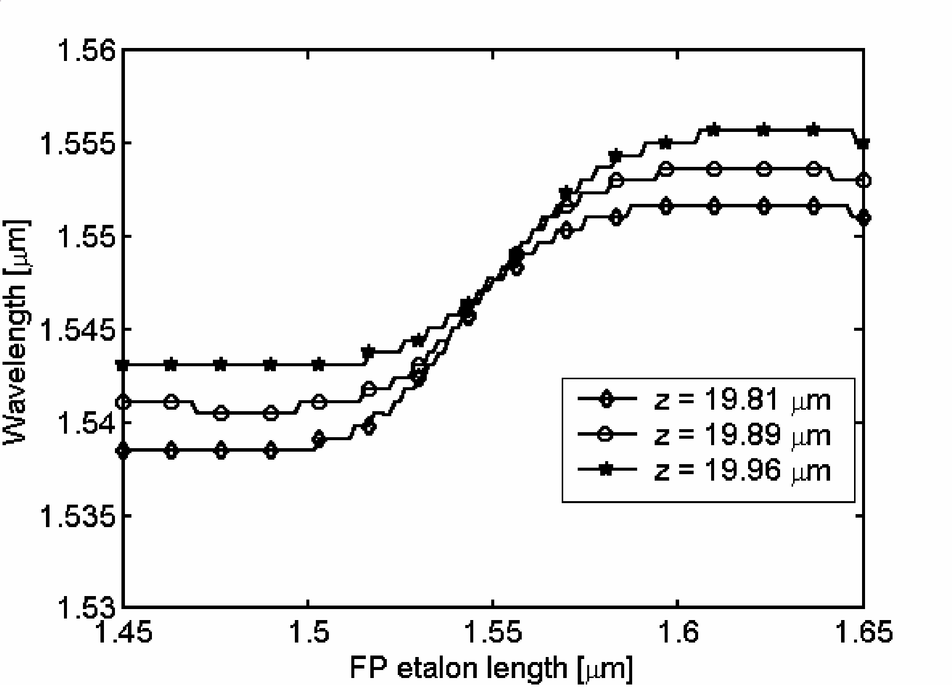

Figure 47. The variation of the tuning curve with small changes to the EC length in the rapid tuning region of an FP-ESEC laser.

4.3.2 Wavelength tuning experiments with the FP-ESEC laser

Sidorin et al. [95, 70, 72] and Heikkinen et al. [14, 96] have presented experimental work on laser tuning with an FP-ESEC configuration. Sidorin et al. [95, 70, 72] observed and characterized the rapid tuning region. Heikkinen et al. [14, 96] mainly used the conventional planar-mirror-type of tuning, but using the additional phase revolution in the FP resonance band to achieve a single mode laser operation. In the following, we will take a look at the measurements based on the work of Heikkinen et al. [96].

4.3.2.1 Measurement set-ups

The measurements of the wavelength tuning in the FP-ESEC configuration shown in the following work were done with two (pre-) prototypes of a FP-ESEC tunable laser. A detailed description of the prototypes is out of the scope of this work (see Heikkinen [96]), but we will now give an overview of the set-up. The prototypes were built on an LTCC (low temperature co-fired ceramics) substrate. The FP-ESEC laser was composed of a 1550-nm InGaAsP/InP laser (Laser 1 in Table 1, p. 30) and a silicon micromachined FP etalon. In the first prototype, shown in Figure 48, the external cavity length could be adjusted via the thermal expansion by changing the temperature of a copper plate carrying the laser. In the second prototype, Figure 49, we used a piezoelectric component to change the external cavity length. The operating temperature of the laser was controlled by using a thermo-electric cooler. The laser light was coupled to an optical fiber with a coupling lens. In the first prototype, this coupling was done through the external cavity, but in the second prototype via the back facet (the facet opposite the ESEC) of the laser. The spectrum of the light was monitored with an optical spectrum analyzer. A photo-diode was used to monitor the laser power.

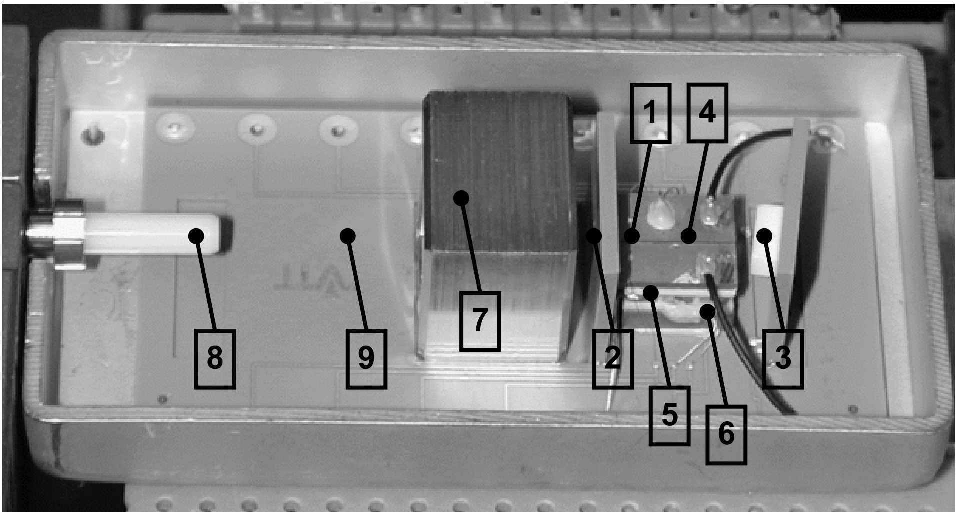

Figure 48. The first prototype of the tunable laser. 1 – laser diode, 2 – micromachined FP etalon (behind the mounting plate), 3 – monitoring photo diode, 4 – laser substrate, 5 – thermoelectric cooler, 6 – copper plate and heater, 7 – coupling lens, 8 – optical fiber, 9 – LTCC substrate with mounting features. The size of the prototype is about 6 cm × 3 cm.

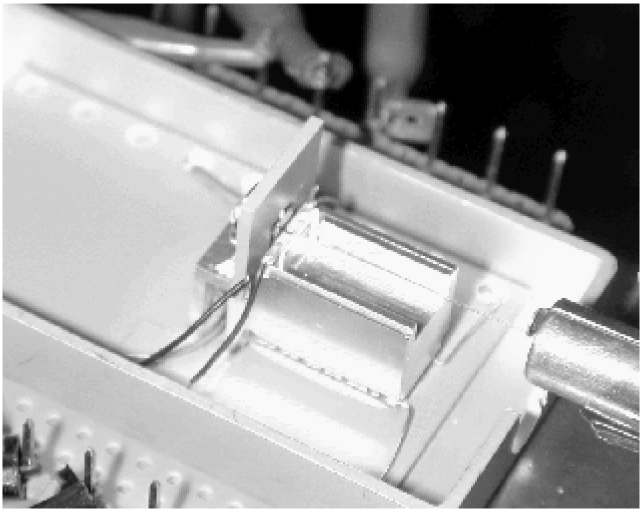

Figure 49. The second prototype.

The structure of the silicon micromachined FP etalon is shown in Figure 50 [97, 98]. The etalon consists of two mirrors composed of quarter wavelength layers of polysilicon and silicon dioxide. The lower mirror is in a fixed position, whereas the upper mirror can be moved towards the lower mirror by applying a voltage between the mirrors. The movement of the upper mirror is caused by electrostatic force. The FP etalon operates in the third order. The (theoretical) mirror reflectance of the FP etalon is 98.7 %.

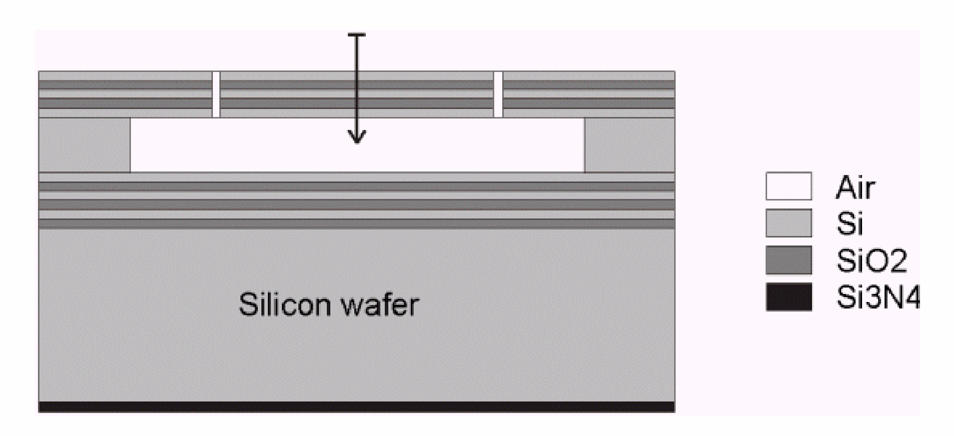

Figure 50. Structure of the silicon micromachined FP etalon. The arrow indicates the direction of the movement of the upper mirror due to the electrostatic force.

4.3.2.2 Conventional mirror tuning with FP etalon

We will now show some tuning results at the conventional mirror-tuning region that are measured using the second prototype. Figure 51 shows the measurement of the principal lasing wavelength versus the piezo voltage. Here, the external cavity length is tuned with the piezo, not the FP etalon length. The voltage of the piezo changes the external cavity length linearly, decreasing the external cavity length with the increasing voltage. The voltage change of 40 V corresponds roughly to an 800-nm change in the external cavity length. The tuning range is about 13 nm. The resulting tuning curve shows nice linear behavior with the piezo voltage.

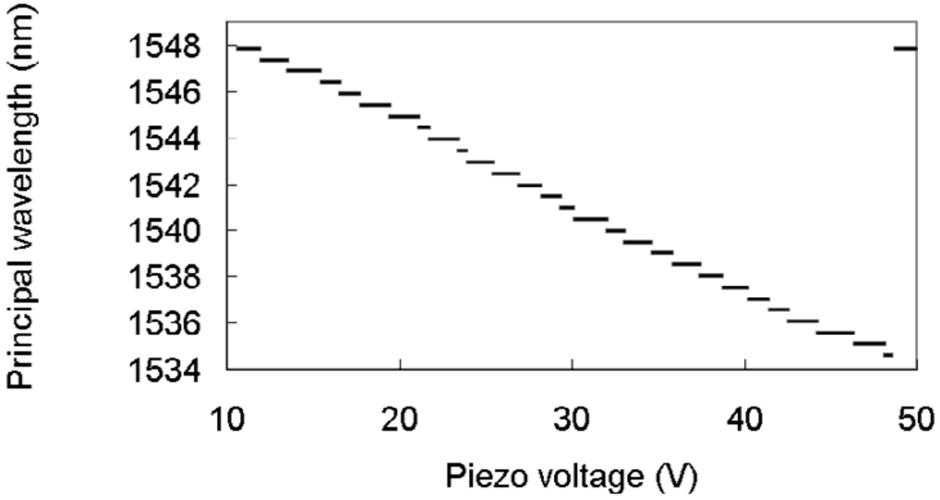

Figure 51. Principal lasing wavelength versus the piezo voltage measured with the second tunable laser prototype.

The piezo tuning, shown in Figure 51 is an example of the wavelength tuning of the semiconductor laser in the PM-ESEC configuration. In the FP etalon tuning, the piezo was used to adjust the initial external cavity length for the tuning with the FP etalon length. Figure 52 shows two examples of the wavelength tuning using the FP etalon length on the conventional mirror tuning region, with different piezo voltages. The horizontal axis represents the voltage between the mirrors of the FP etalon. The functionality between the voltage and the FP etalon length is non-linear, leading to the increasing slope of the tuning towards the higher voltages (for the actual functionality, see e.g. [95]). Changing the voltage from 0 V to 34 V, the upper mirror moves less than 400 nm, leading to the tuning range of 6 nm, which is about half of the tuning range observed with the piezo tuning.

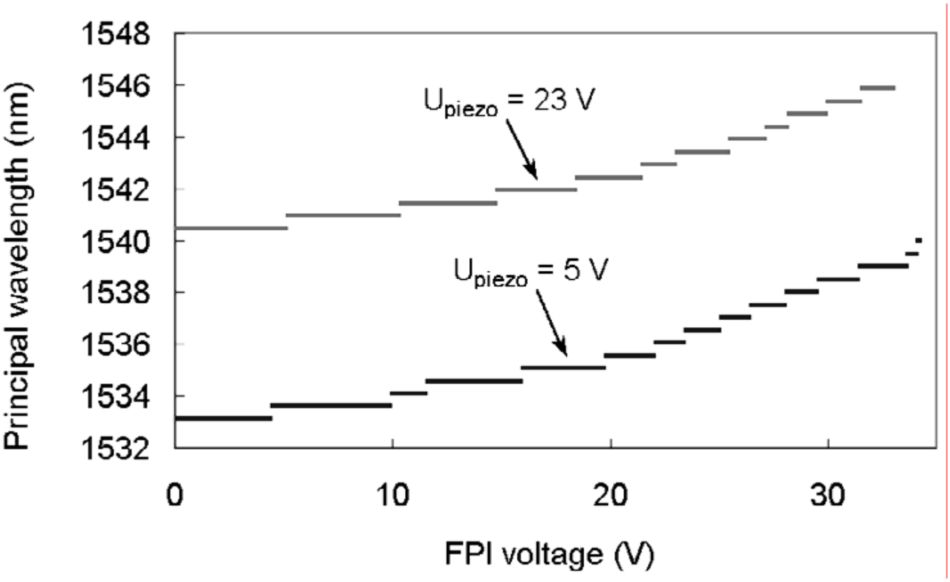

Figure 52. Principal lasing wavelength versus the FP control voltage in the conventional mirror-tuning region measured with the second tunable laser prototype for two different piezo voltages.

4.3.2.3 Rapid tuning region

Unfortunately, the mirror reflectance of the micromachined FP etalon was too high to get a proper wavelength tuning in the rapid tuning region. The experimental results are, however, in line with the simulations with the high-finesse FP etalons. The rapid tuning has been earlier observed by Sidorin et al. [70, 95, 72]. Figure 53 shows some of our trials to find the rapid tuning region using the first prototype. The measured principal (peak) wavelength of the laser's spectrum is shown as the function of the FP control voltage. The three curves are plotted for different temperatures of the copper plate that was used to tune the external cavity length with the thermal expansion. The hotter the copper was, the longer the external cavity length was. The temperatures thus represent different external cavity lengths.

The tuning curves in Figure 53 indicate that no continuous 'up-tuning' was found. ('Up-tuning' is a term adopted in the previous section referring to the tuning to the longer wavelengths with the increasing FP etalon length – here the increasing FP voltage decreases the FP etalon length.) Closest to that is the tuning curve for 34 °C, where the wavelength is somewhat decreased before the laser operation jumps to the shorter wavelengths. For the lower copper temperature (24 °C) the FP resonance causes a slight dip in the tuning curve close to the FP control voltage of 39 V. For the higher temperature (38 °C), the down-jump occurs at the low FP voltages, and the FP resonance causes only a slight change in the wavelength close to 39.5 V.

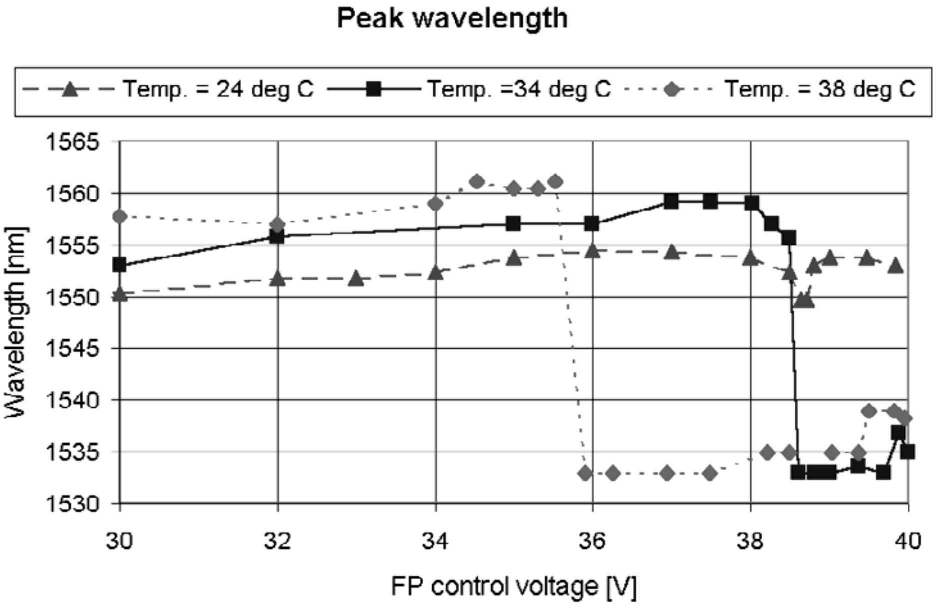

Figure 53. Trials to find the rapid tuning region using an FP etalon with too high finesse in the first tunable laser prototype. The principal lasing wavelength is plotted versus the FP control voltage.

The tuning curves of Figure 53 have been reconstructed with simulations in Figure 54. Note that the horizontal axis in the figure has been reversed to help the comparison. The purpose of this reconstruction was not to find a perfect match, but to show that the theory qualitatively predicts all of these possibilities in the tuning of a high-finesse FP etalon. Comparing the two figures, we can conclude that all the main features of the measurements mentioned above are repeated in the simulations.

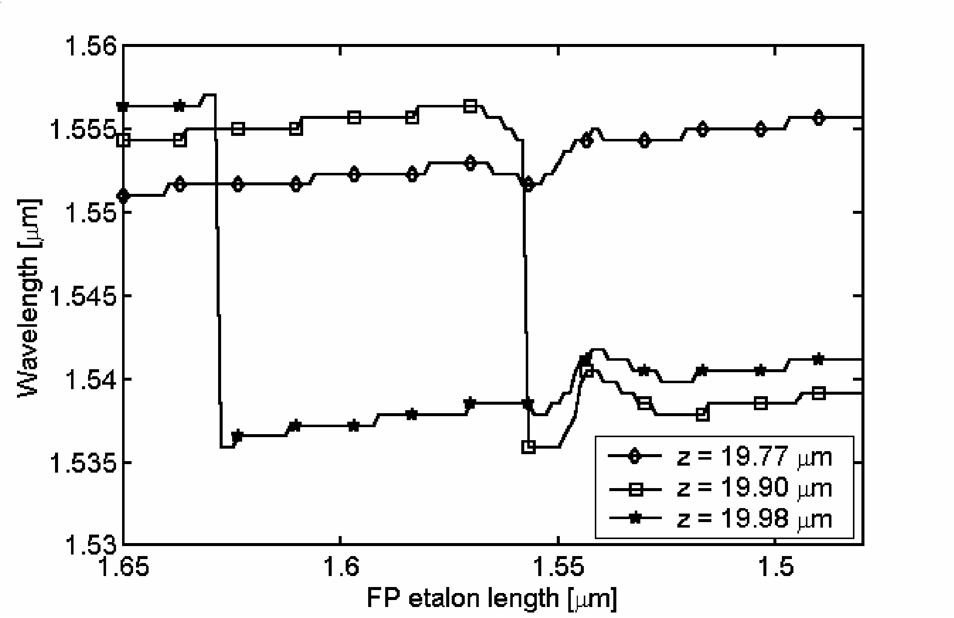

Figure 54. Simulation of the tuning curves for a high-finesse FP etalon.

The left side of Figure 55 shows examples of the measured spectra of the FP-ESEC laser operating at different FP control voltages. At the top figure, the lasing point is on the long-wavelength EC mode. At the center figure, a 'bridge' is formed between the two EC modes. Because of the high finesse of the FP etalon, the true EC modes are not suppressed enough and we can see three peaks in the spectrum: the EC mode on the long wavelengths, the 'bridge' between these modes, and the EC mode on the short wavelengths. At the bottom figure, the FP voltage is further decreased, and now the lasing is operating on the short-wavelength EC mode. On the right side of Figure 55 the spectra have been reconstructed by the simulations. A simulated spectral image of the tuning is shown in Figure 56.

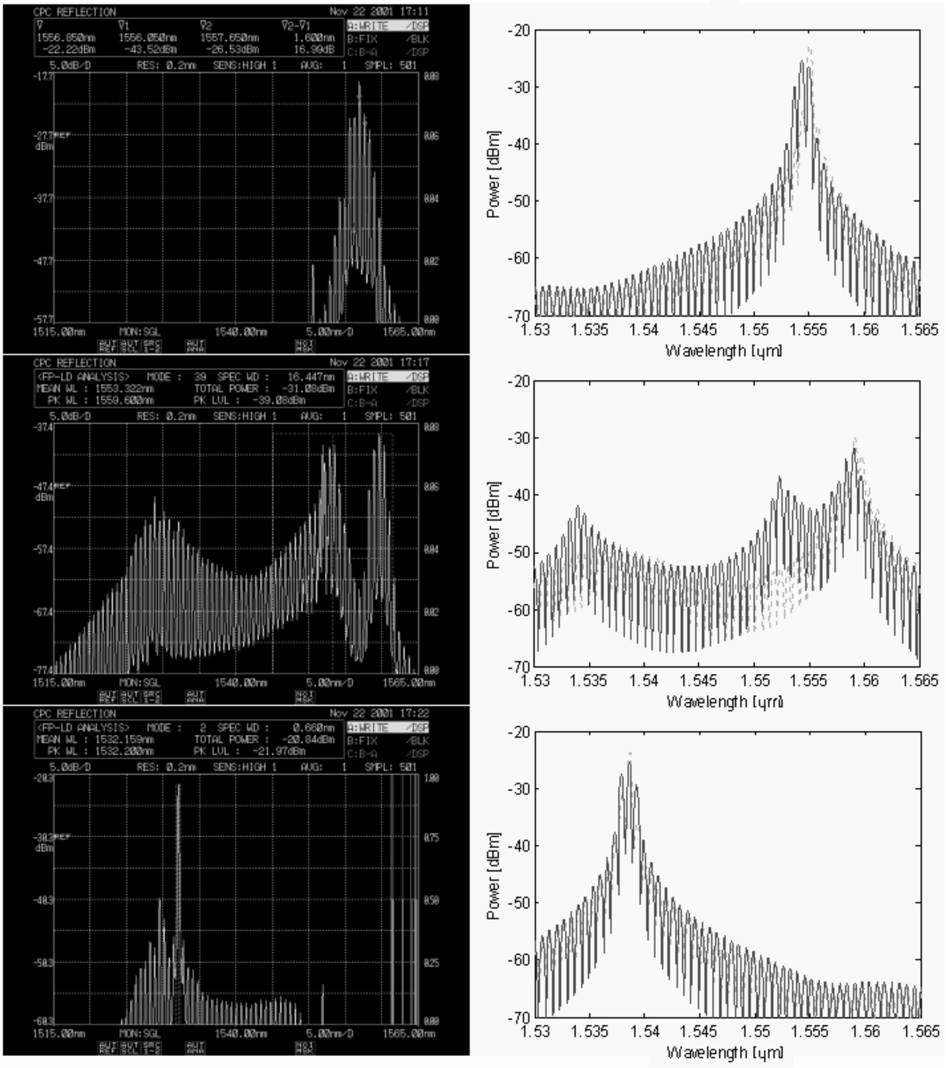

Figure 55. Measurements (left) and simulations (right) of the laser spectrum for the FP-ESEC laser with a high-finesse FP etalon. The rows correspond to different values of the FP etalon length.

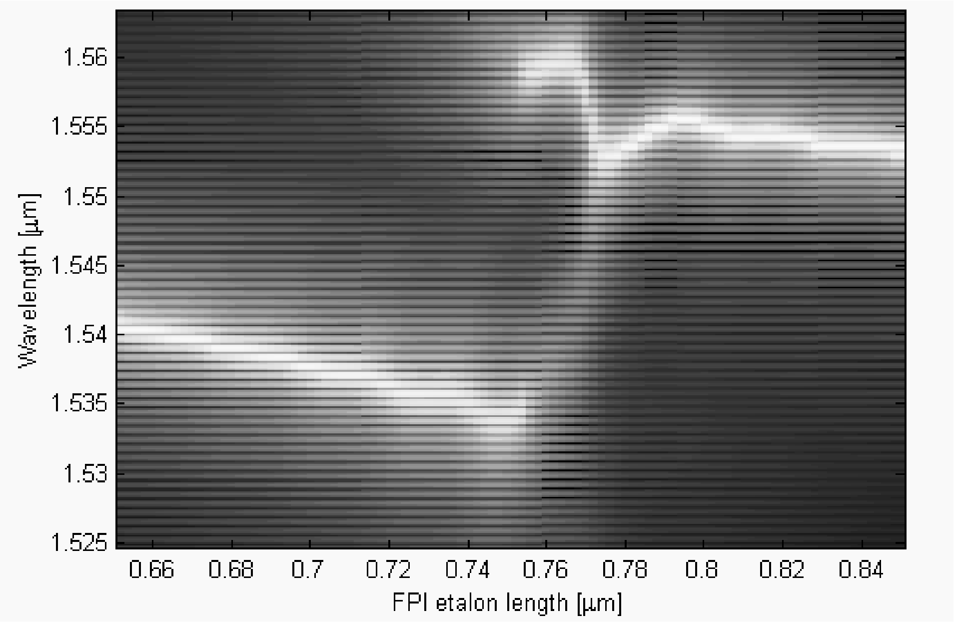

Figure 56. Simulated spectral image of the tuning of the FP-ESEC laser using a high-finesse FP etalon.

4.3.3 Conclusions

We used our laser model to analyze the tuning characteristics of an FP-ESEC laser. The analysis shows that two different tuning regions can be found: the conventional mirror tuning and the rapid tuning regions. The wavelength behavior of the rapid tuning region is very sensitive to the design parameters of the system, especially to the mirror reflectivity of the FP and the external cavity length. It was shown that without an accurate adjustment of the external cavity length, it is very difficult to apply the rapid tuning region efficiently.

The experimental results on the wavelength tuning with the FP-ESEC configuration were presented. The conventional mirror-tuning region was demonstrated. Unfortunately, the rapid tuning region was not observed, due to the high finesse of the FP etalon used in the experiments. The observed behavior of the laser spectrum was, however, well in line with the simulations for the high-finesse FP etalons, giving qualitative proof for the simulation method.

4.4 Wavelength tuning profilometry

The third example of the use of the ESEC lasers is the use of the wavelength tuning of the ESEC laser in the measurement of surface profiles. In this measurement configuration, the laser diode is brought to close proximity of the surface to be measured (see Figure 57). Some part of the light emitted by the laser is reflected from the surface and coupled back to the laser cavity. The surface thus acts as an external reflector. As seen in the previous sections, the lasing wavelength is very sensitive to the changes in the length of the external cavity via the changes of the phase of the external reflection. This fact can be used to determine the changes in the distance between the laser facet and the external reflector surface just by monitoring the wavelength of the laser. By scanning the surface with the laser ‘flying’ very close to the surface and monitoring the lasing wavelength, we can get a detailed picture of the profile of the surface. This measurement system is called *wavelength tuning profilometry* in the ESEC configuration [9].

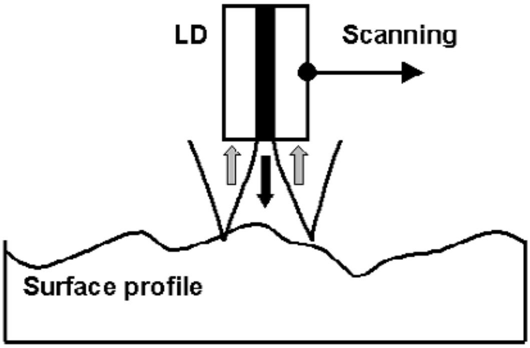

Figure 57. Schematic picture of the ESEC configuration for the wavelength tuning profilometry.

The previous two examples of the use of the ESEC lasers were based on planar external mirrors. The Gaussian beam approximation and the results from the PM-ESEC in Section 4.2 can be used to give the first order estimate of the laser’s operation point with a certain surface profile. However, the planar mirror approach will only take into account the change in the distance between the laser and the measured surface. A non-planar surface will also change the wavefront of the reflected laser beam, which has to be taken into account in the analysis if the surface profile has high spatial frequency components.

In this section we will first analyze the wavelength tuning profilometry from the viewpoint of the planar mirror approach. After that we will present some results of surface profile measurements with this method, and finally we use FDTD simulations of the electromagnetic fields close to the surface to explain some of the features observed in the measurements.

4.4.1 Analysis with the planar mirror approach

We will now study the 'first-order' properties of the wavelength tuning profilometry. The main results that we want to get from this analysis are the limiting factors affecting the resolution on the depth of the profile and the lateral resolution on the surface. We will also discuss the optimal configuration for the measurements.

The limiting factors for the resolution in the profile depth direction are the longitudinal mode structure of the laser and the tuning range per one half-a-wavelength cycle in the external cavity length. The functionality of the sensitivity of the laser's wavelength to the change of the external cavity length is in linear approximation $dz_{EC}/d\lambda = \lambda_f/(2\Delta\lambda)$, where $\Delta\lambda$ is the wavelength tuning range, λ_f is the wavelength of the free-running laser (peak wavelength of the gain). The wavelength tuning is 'quantized' by the longitudinal modes of the laser. The mode separation, i.e. the smallest detectable change in the wavelength is $\Delta\lambda_m \approx \lambda^2/(2nL)$, where L is the length of the laser diode, and n is the effective refractive index of the laser waveguide. This mode separation and the sensitivity of the laser give the smallest detectable change in the external cavity length: $\Delta z_{EC,min} = dz_{EC}/d\lambda\ \Delta\lambda_m = \lambda_f/(2\Delta\lambda)\ \lambda^2/(2nL) \approx \lambda^3/(4\ n\ L\ \Delta\lambda)$. As the basis of this analysis, a short wavelength laser is preferable in this application even if the tuning range $\Delta\lambda$ scales with the wavelength.

In the following experiments, we used a 790-nm GaAs laser (Laser 2 in Table 1, p. 30). The wavelength tuning measured for this laser in the PM-ESEC configuration is shown in Figure 33. The maximal tuning range of the laser was about 12 nm, giving the estimated profile depth resolution of 6 nm (n = 3.6, L = 500 μm).

The non-linearity of the laser tuning causes some uncertainty to the depth measurements. In principle, the non-linearity can be compensated by calibration and data processing, but in practice that may be difficult, since so many factors (temperature, surface reflectance) affect the shape of the tuning curve on the non-linear tuning region. One way to estimate the accuracy of the depth measurement is to remember that the half-a-wavelength periods in the external cavity length are well pronounced in the wavelength measurements. Those half-a-wavelength periods can thus be used as the basic ‘measuring sticks’ on the profile measurements. Even though there is some non-linearity in the tuning, we can estimate that one tenth or one twentieth of the one half-a-wavelength cycle can be resolved. That will give us the accuracy estimate of 20–40 nm for the profile depth measured with the 790-nm laser diode.

To estimate the lateral resolution, we can consider the size of the laser beam on the surface. The $1/e^2$ beam width ω_x for a Gaussian beam is given with Equation (65). In our case the beam waist is about 1 μm x 3 μm, giving the estimated beam width depicted in Figure 58. (The CD track separation added to the figure will be used in the next section.)

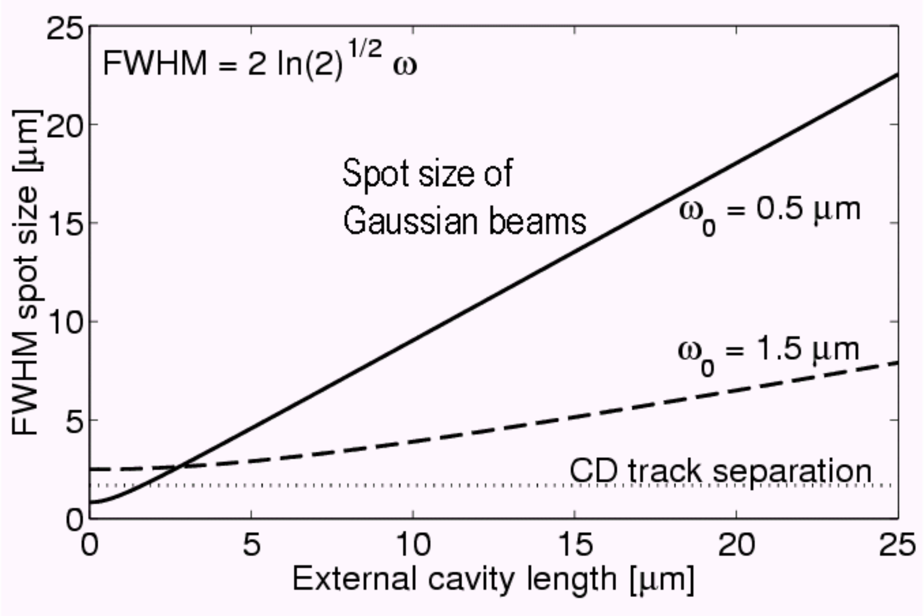

Figure 58. The spot size of the Gaussian beams on the surface of the external reflector as the function of the external cavity length. The beam-waist radii are indicated with ω_0. A CD track separation is shown in the image to indicate the need for very short external cavity lengths in the DSLR configuration.

The optimal ‘flying height’ of the laser above the measured surface depends on three factors. 1) The aim for high depth resolution of the measurement drives the flying height towards the largest tuning ranges that are found on the non-linear tuning region (see Figure 28). 2) The accuracy of the measurement drives the flying height to the linear tuning region of the laser, i.e. towards large external cavity lengths. 3) The aim for high lateral resolution drives the flying height to the reduced tuning region, i.e. towards short external cavity lengths. Since there is no ‘common ground’ for these factors, the system can be optimized for one or two of these needs at a time depending on what are the most important requirements for the measurement.

4.4.2 Profile measurements via wavelength tuning

Let us now look at the experimental results of the wavelength tuning profilometry. The experiments were done using the 790-nm GaAs laser (Laser 2 in Table 1, p. 30). The target surface was a sinusoidal surface relief grating, etched to glass, and coated with a thin layer of gold to increase the reflectivity. Various grating periods were used in the measurements. We will show the measurement results for two grating types with the periods 30 μm and 5 μm.

The laser was mounted in a fixed position and the target grating was mounted on a nanopositioning system. The light emitted from the back facet of the laser (the facet opposite to the ESEC) was directed to an optical spectrum analyzer via an optical fiber. Both the optical spectrum analyzer and the nanopositioning system were controlled with a computer, and the measurement data was automatically acquired and saved on the computer memory. The laser was brought to close proximity of the target by manually controlling the nanopositioning system. The external cavity length was estimated to be about 5 μm, indicated by the width of the tuning range. During the measurement the target was automatically moved in small steps in the direction perpendicular to the grating lines. After each step, the spectrum was measured and saved on the computer.

Figure 59 shows the spectrum of the laser (in vertical direction) as the function of the scan position. The levels of gray represent the values of the spectral density of the optical power. Note that the wavelength scale is increasing towards the bottom of the figure. Starting from the left side of the figure, there is a short section of constant signal (which is the planar top surface of the substrate, where the grating is etched). After that the wavelength starts to increase, indicating an increase in the external cavity length. The increase continues for five cycles of the half-a-wavelength tuning periods. After that the external cavity length starts to decrease and that decrease continues for a little more than five cycles, and so on. What we see in this spectral image is actually the profile of the grating mapped to the laser wavelength in the half-a-wavelength tuning periods.

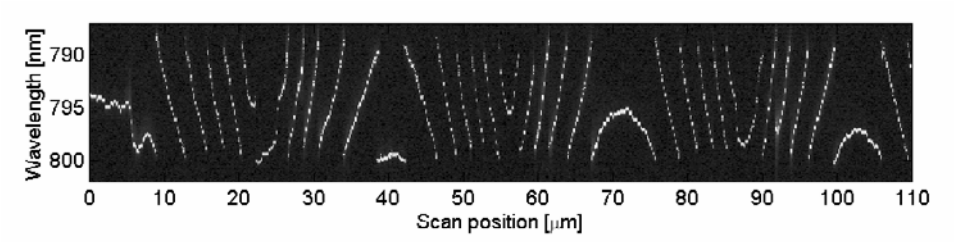

Figure 59. Spectrum of the laser as the function of the scan position on a surface relief grating in the wavelength tuning profilometry configuration. The spectral density is shown in gray scale. Note that the wavelength scale is reversed.

Each of the half-a-wavelength tuning periods corresponds to a 2π shift in the phase of the external reflection. In Figure 60, we have converted the wavelength data of Figure 59 to the phase of the external reflectance and added multiples of 2π to the phase. Now the measured profile of the grating lines is already visible. This intermediate step is used later when comparing the FDTD simulations to the measurement. The final step is to convert each of the 2π sections to a half-a-wavelength change in the external cavity length and remove the excess orders of the phase. The result is the grating profile shown in Figure 61.

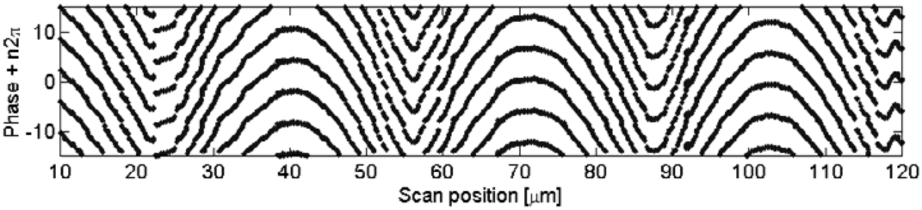

Figure 60. Phase diagram for the external reflection based on the wavelength data shown in Figure 59.

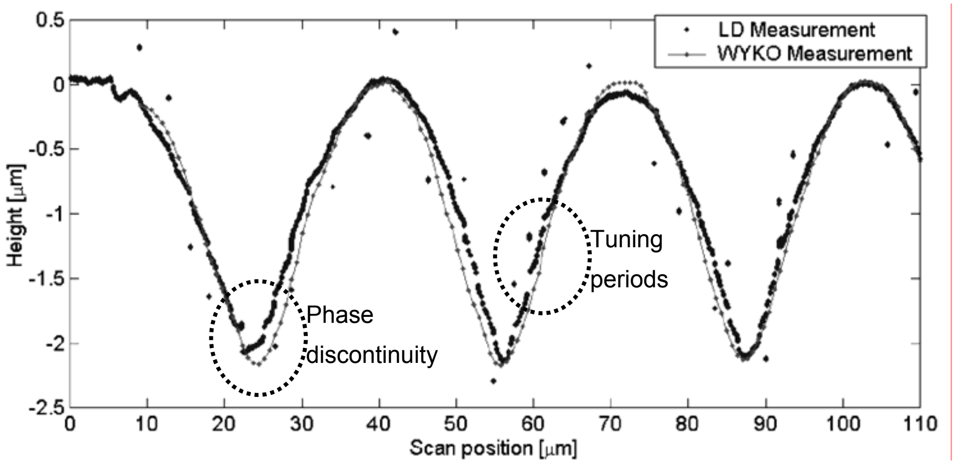

Figure 61. The surface profile of a grating measured using the wavelength tuning profilometry technique (LD measurement) compared to a measurement done with a commercial white light interferometer (WYKO measurement). Some features of the measured profile are highlighted in the image.

Figure 61 also shows the grating profile measured with a commercial white light interferometer (WYKO). The comparison of these two measurements shows a relatively good similarity of results. The major difference between these two measurements is that the wavelength tuning periods can still be seen in the ESEC measurement. That gives some non-existent surface structure to the measured profile. With a proper transformation routine from the wavelength to the phase, this effect can possibly be diminished. Here, we have used a simple linear mapping between the wavelength and the phase. Another difference in the profiles is the phase discontinuity at the bottom of the grating line. That effect is physical in nature. It is caused by the bottom of the grating that focuses the reflected light. This causes phase discontinuities near the focus seen in the profile. This mechanism is proved later on with the FDTD analysis.

The experiment described above was done with a grating with the periodicity of 30-μm and the depth of 2 μm. Figure 62 shows the measured phase diagram for a grating with the same depth but with the periodicity of 5 μm. Here, no trace is left of the profile of the grating. We will next use FDTD calculations to find out why the signal disappears with the short grating periods.

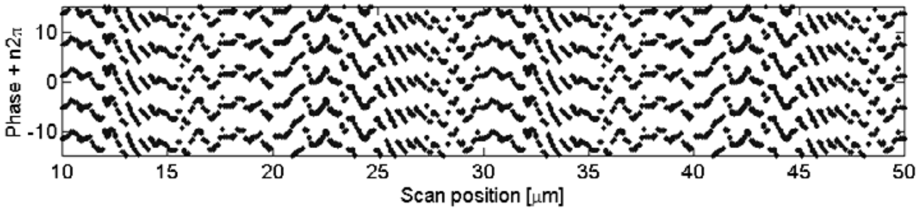

Figure 62. Phase diagram for the external reflection based on the wavelength tuning measurement of a dense grating. The information of the surface profile is lost.

4.4.3 FDTD simulations of the fields close to the surface

We used a two-dimensional scalar finite difference time domain (FDTD) code [99] to simulate the optical fields of the laser light in the vicinity of the grating surface. In this simple model, the laser source was modeled as a 'hard source' (see [57]) using a constant amplitude distribution over the source area. The problem with the hard source is that it reflects the optical fields in the simulation. The grating was modeled as a high-index material, providing relatively high reflectivity. Absorbing boundaries (simple Murr ABC model [57]) were applied to the margins of the calculation grid.

The result of the FDTD calculation is the total field distribution in the system. The incident and the scattered components are not separated. To calculate the phase and the amplitude distribution of the reflected component, the non-reflected incident component of the field has to be removed. This was done by first calculating the steady state optical fields for an isolated laser, and then subtracting this isolated component from the fields that were calculated with the grating in place. The calculated scalar electric field of the isolated laser is shown in Figure 63. The amplitude of the electric field is shown on the left and the relative phase is shown on the right side of the figure.

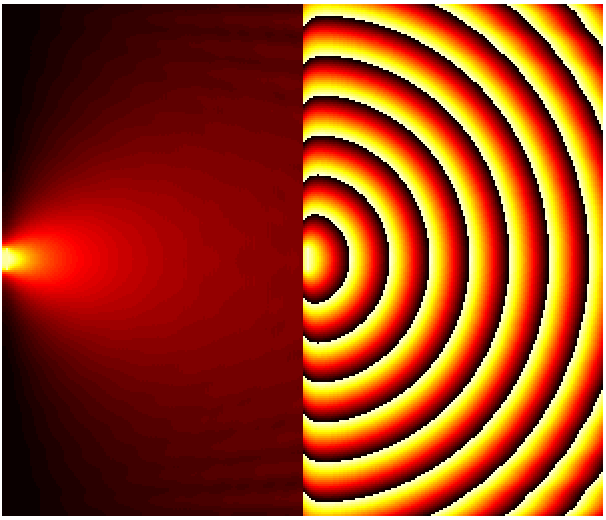

Figure 63. Scalar FDTD simulation of the light beam emitted by a solitary laser; (left) amplitude of the optical field; (right) phase of the optical field.

First we calculated the optical fields for a coarse grating. The resulting field distribution is shown in Figure 64. On the left panel is the total field and on the right panel is the reflected part of the field. Both amplitude and phase are shown in the figures. The grating period in the simulations was 12 μm and the depth of the grating was 2 μm. The wavelength used in the simulations was 790 nm.

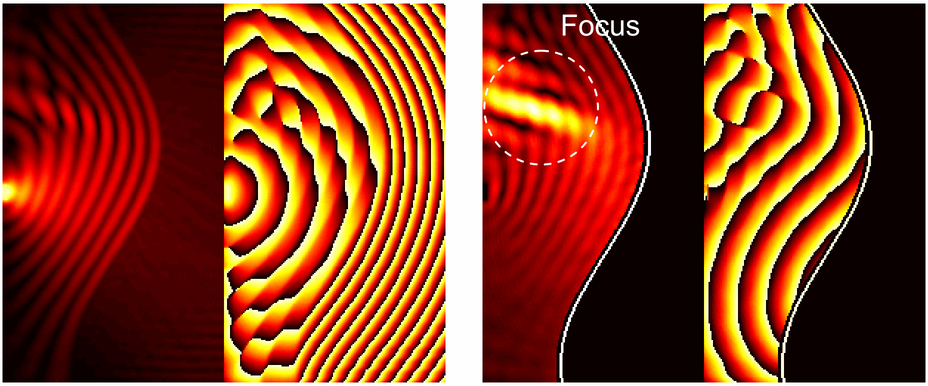

Figure 64. Scalar FDTD simulation of the field distribution of the laser scanning the long-period grating; (left) the amplitude and the phase of the total electric field; (right) the amplitude and the phase of the reflected electric field. The focus produced by the convex part of the grating can be seen in the image.

Figure 64 is just one snapshot from the scan of the grating, but it already shows some significant features. One of the features is the focus that is formed by the concave bottom of the grating. At the focus, the cross-waves of the reflected light generate an area with a high intensity but also form discontinuities in the phase distribution. These discontinuities were seen in the measured profile of the grating in Figure 61.

Another feature shown in Figure 64 is the numerical reflectance of the hard source that generates a low-amplitude standing wave between the grating and the source. That artificial reflectance generates some fluctuation to the phase near the source. This fluctuation is weak enough not to disturb the qualitative analysis of the system and can be interpreted as being caused by the reflectivity of the laser facet.

To calculate the changes in the reflected phase when the grating is scanned with the laser, we did a series of simulations with varying the lateral position of the grating relative to the laser. From each of these simulations, we saved the phase data from a narrow stripe extending from the laser source to the surface of the grating. From these narrow stripes of phase information we constructed the diagram showed in Figure 65. That diagram shows how the phase profile of the electric field directly in front of the laser (in the space between the laser and the grating) will change when the grating is scanned. This diagram shows relatively smooth changes in the phase profile as the function of the scan position.

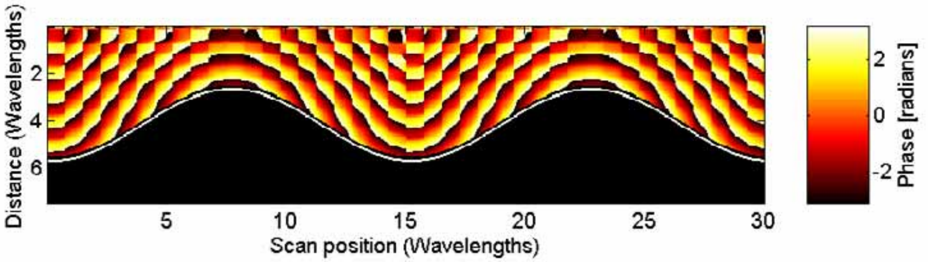

Figure 65. Diagram of the phase profile directly in front of the laser (in the space between the laser and the grating) for the long-period grating as the function of the scan position.

To get a diagram of the reflected phase on the laser facet, similar to the measured phase diagram in Figure 60, we used the phase information from a horizontal line close to the laser source in Figure 65. The resulting phase diagram is shown in Figure 66. The simulated phase diagram and the measured diagram are very similar. Even the phase discontinuity caused by the focusing is shown in both cases.

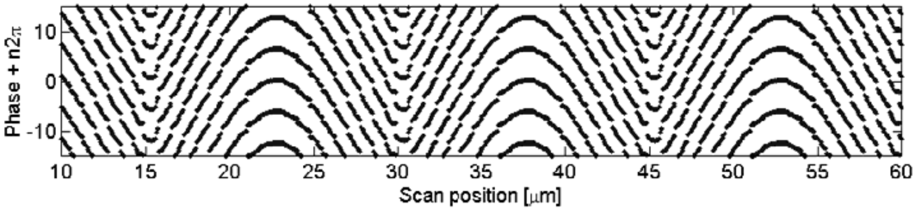

Figure 66. Simulated phase diagram of the reflected field close to the surface of the laser for the long-period grating. The diagram is very similar to the diagram on the phase measured via the wavelength tuning experiment (see Figure 60).

One feature that is worth noting is the shape of the phase profile. The top parts of the grating lines are round, U-shaped, whereas the bottom parts of the grating lines are sharp, V-shaped. This same shape is repeated in the measurements (cf. Figure 60 and Figure 61) in the ESEC configuration, but also in the measurements that are done with the commercial white light interferometer (WYKO, Figure 61). According to the simulations, both of these methods thus seem to have difficulties in reproducing the actual sinusoidal shape of the grating.

Next, we did similar simulations for a grating with the periodicity of about 4 μm. The simulated fields for that grating are shown in Figure 67, the diagram on the phase in front of the laser as the function of the scanning position is shown in Figure 68 and the phase diagram for the external reflection is shown in Figure 69. All of these diagrams show that the phase distribution is disturbed so severely by the dense grating structure that the profile information is lost. The (multiple) reflections from the surface are producing cross-waves that destroy the smooth phase distribution. The phase diagrams of Figure 62 and Figure 69 are very similar, and this simulation explains very well the experimental results with the dense grating.

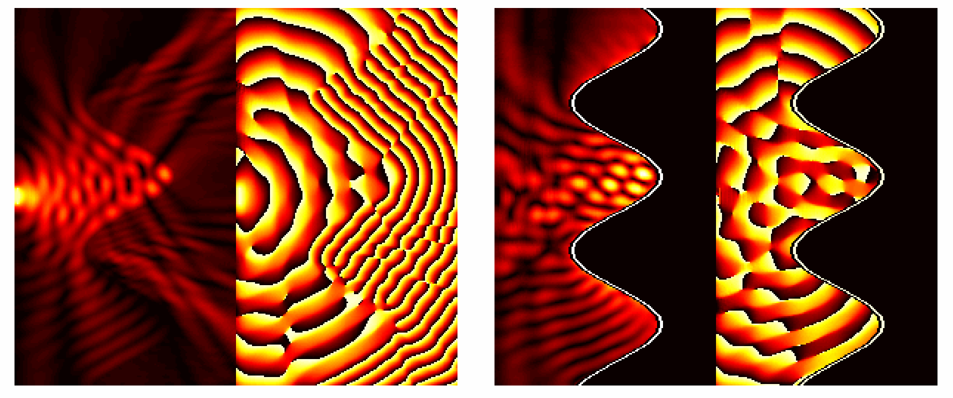

Figure 67. Scalar FDTD simulation of the field distribution of the laser scanning the short-period grating; (left) the amplitude and phase of the total electric field; (right) the amplitude and phase of the reflected electric field. The phase distribution is severely distorted by the grating.

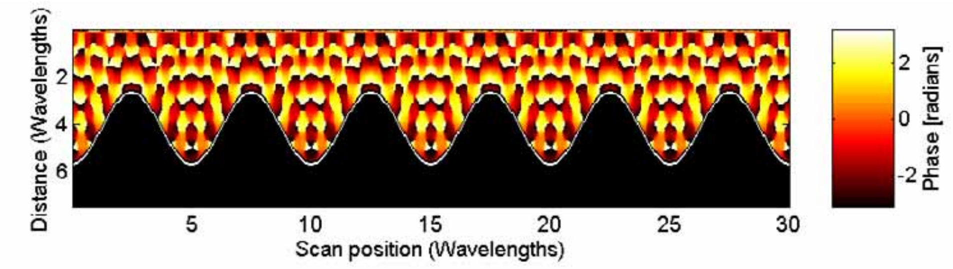

Figure 68. Diagram on the phase profile directly in front of the laser (in the space between the laser and the grating) for the short-period grating as the function of the scan position.

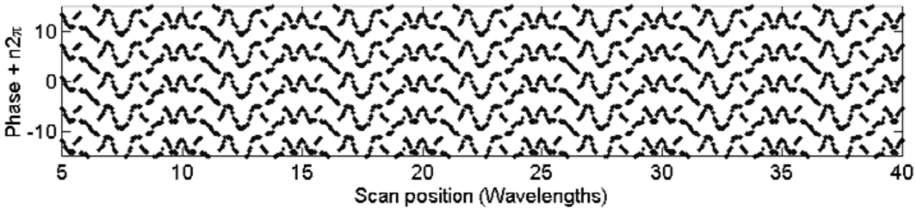

Figure 69. Simulated phase diagram of the reflected field close to the surface of the laser for the short-period grating. The diagram is, again, very similar to the diagram on the phase measured via the wavelength tuning experiment (see Figure 62).

Let us now conclude the results of the experiments and simulations of the wavelength tuning profilometry using the ESEC configuration. The most important result is the proof of the measuring principle. It is possible to measure the surface profile with this method. However, the surface must be smooth enough not to produce cross-waves that will distort the phase signal carried by the reflected light. In addition, the reflectance of the surface must be nearly constant which can be deduced from Figure 30 and Figure 31.

4.5 Direct semiconductor laser readout in optical data storage

Next, let us consider the use of the ESEC laser configuration in the reading and writing of data marks in the optical data storage. We will study an optical read/write system where the front facet of a semiconductor laser is brought very close to the recorded surface of an optical disk (see Figure 70). Some of the light emitted by the laser is reflected back to the laser cavity from the data layer of the disk, i.e. the disk operates as an external reflector in an ESEC configuration. The external reflection is modulated by the recorded data marks when the disk is scanned with the laser. The laser reacts to the changing feedback by changing its operation point, which causes changes in the bias voltage, the optical output power, and the wavelength, as seen in the previous sections. The changes in the laser operation are monitored by analyzing the light emitted from the back facet of the laser. Increasing the power of the laser, the data marks can also be recorded to the optical disk. To implement this read/write system, the laser will be mounted on a slider flying close to the data surface of the disk. We use the term *direct semiconductor laser readout* (DSLR) for this read/write head configuration.

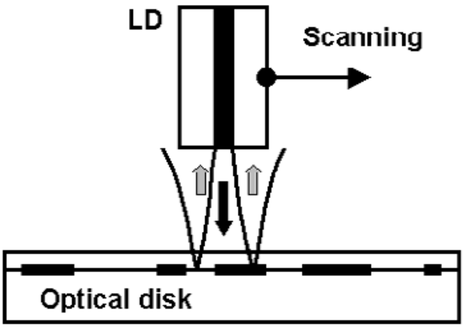

Figure 70. Schematic illustration of the DSLR system.

The EC configuration was first suggested for use in optical data storage by Mitsuhashi et al. [26, 1, 39] in the early 1980's. The first DSLR systems utilizing the ESEC configuration were proposed by Ukita et al. [82] in the late 1980's. After that, DSLR has been studied by several research groups [8, 10, 13, 77, 78, 15, 50, 79, 80, 83, 84, 85]. The introduction of very small aperture lasers (VSAL) has brought the DSLR technique closer to the high data densities achieved with the other storage techniques [8, 13, 86, 87, 15, 88, 89, 90, 92]. The DSLR method has also been used with the vertical cavity surface emitting lasers (VCSELs) [64, 81, 63].

In Section 4.5.1, we will study how we can enhance and optimize the operation of the DSLR system by taking the full advance of the ESEC laser dynamics. Previously only the laser power or the bias voltage has been monitored to produce the playback signal. We will propose some ways to apply the wavelength tuning effects to enhance the playback signal. In Section 4.5.2, we will use the combination of our laser model and the FDTD modeling to simulate and compare the operations of conventional edge emitting semiconductor lasers and very small aperture lasers (VSAL) in the DSLR configuration.

4.5.1 Enhancements in direct semiconductor laser readout

In this section we will review and deepen the work presented in [10].

4.5.1.1 Modeling methods

In this analysis of the DSLR, we modeled the optical disk as a planar reflector that had 'data marks' on it. The data marks were modeled as areas with a different reflectivity than the background. A Gaussian beam was used to model the laser output, and the laser's waveguide mode. The effective reflectance was calculated using the Fourier optics (see Section 3.3.4). The angular spectrum decomposition was used for modeling the beam propagation from the disk surface to the laser facet. The overlap integrals on the laser facet were calculated numerically from the complex-valued matrices containing the sampled field distributions for the reflected field and the waveguide mode. Figure 71 shows an example of the simulation of the fields. The top row shows the amplitude of the reflected field on the disk surface and the bottom row shows the corresponding field on the laser facet. The data mark is seen on the top row as a rectangular high-reflectance area on the low-reflectance background.

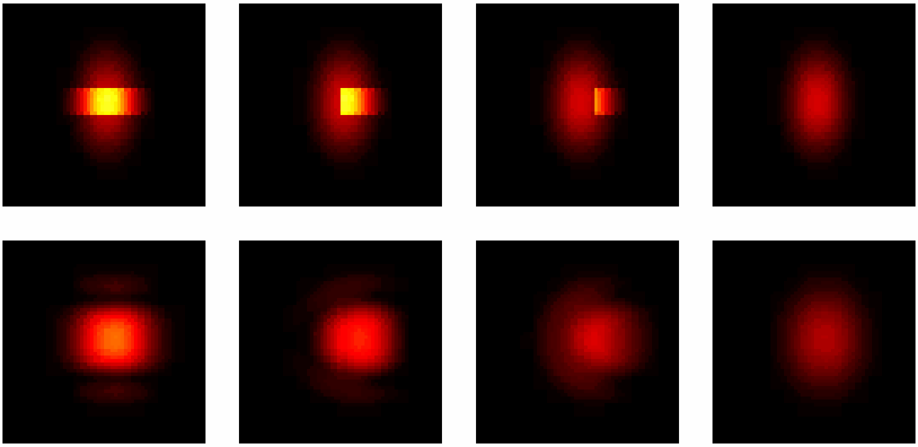

Figure 71. Example of the simulation of the fields reflected from the optical disk with data marks on the surface. The top row shows the amplitude of the reflected field on the disk surface and the bottom row shows the corresponding field on the laser facet.

In some simulations, Babinet’s principle was used to decrease the simulation time. The area of the optical disk was divided into the background and the path for the data mark (see Figure 72). The path of the data mark was divided into small areas A_i, $i = 1 \ldots N$. The data mark was composed by changing the reflectance of some of these areas from the ‘background’ values to the ‘data mark’ values as indicated in Figure 72. The coupling coefficients were calculated individually for the background and each of the areas A_i. The coupling coefficient for the whole reflected field was calculated as the sum of the coupling coefficients for the partial fields (from the partial areas), weighted with the reflectivity of each area.

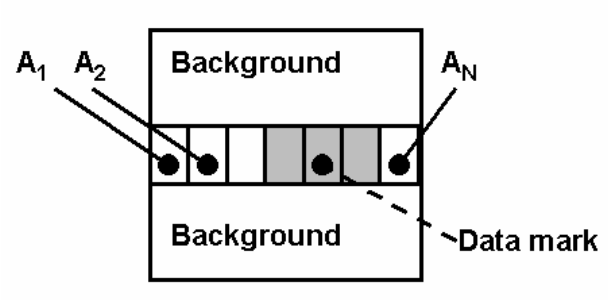

Figure 72. The spatial division of the surface of the optical disk used with Babinet’s principle to calculate the effective reflectances for the passing data marks.

4.5.1.2 Comments on the flying height

Most of the analysis of the external cavity length, presented in Section 4.4.1 for the wavelength tuning profilometry, applies to the DSLR, too. Here we are very interested in the lateral resolution of the scanning system, and therefore we want the external cavity length (the flying height) to be as short as possible. Figure 58 shows the Gaussian beam full width half maximum (FWHM) value as the function of the external cavity length for a 790-nm GaAs laser. To achieve resolutions below the CD track separation, also shown in the figure, the external cavity length should be smaller than 2 µm.

The measured quantity whose sensitivity we want to optimize may be the change in the wavelength, but it may as well be the optical power or the bias voltage, or any combination of these. Traditionally in the DSLR systems, the bias voltage or the optical power has been monitored. The wavelength changes decrease in the smallest ESEC lengths, but the power and the voltage changes, and the overall sensitivity to the changes in the external reflectance will also increase with the decreasing ESEC lengths. Therefore, the lowest flying height i.e. the shortest possible external cavity lengths are usually preferable. The only exception to this is the signal's possible dependence on the interference effects between the internal and the external reflectivities. In that case, the flying height has to be fixed on a defined value giving the best signal. Some examples of this are shown in the following sections.

4.5.1.3 Various types of read signals

Various types of read signals can be formed by changing the design parameters of the ESEC configuration. The physical coding usually used in the optical data storage is so-called modulation coding, where the data is encoded in the lengths of the marks recorded on the disk. The marks are areas on the data layer of the disk that have different reflectance compared to the background. The reflectance difference can be on the amplitude or the phase of the reflectance depending on the media used. As the disk is spinning at a constant speed, the data signal is detected in time frames of length T. The mark lengths usually start from 3T and, depending on the coding, can go e.g. up to 11T or 13T. In the modulation coding, the change from the mark to the background area or vice versa within the time frame means a physical channel bit '1', no change means a channel bit '0'.

Let us study the influence of the various design parameters on the signal using the effective reflectivity of the ESEC. The optical power from the back facet of the ESEC laser is roughly proportional to the amplitude of the effective reflectance of the ESEC (see Figure 20). With the short ESEC lengths the amplitude of the effective reflectance is only weakly dependent on the wavelength, so that we can neglect the spectral effects at this point. Figure 73 introduces a 'mark scan diagram', where the values of the effective reflectance are plotted on the complex plane. When the mark is scanned with the beam, the reflectivity draws a trajectory on the complex plane. That trajectory is shown in the 'scan diagram'. The trajectory starts from the point representing the effective reflectance caused by the background area of the disk. On the opposite end of the trajectory is the effective reflectance on the mark center. As the mark passes the scanning beam the effective reflectivity value moves on the trajectory first towards the mark center value as indicated with an arrow in Figure 73. After the mark center passes the scanning beam, the reflectivity value moves back to the background value along the trajectory. The 'scan diagram' can be used to understand the relationship between the signal produced by the laser and the various design parameters of the DSLR system.

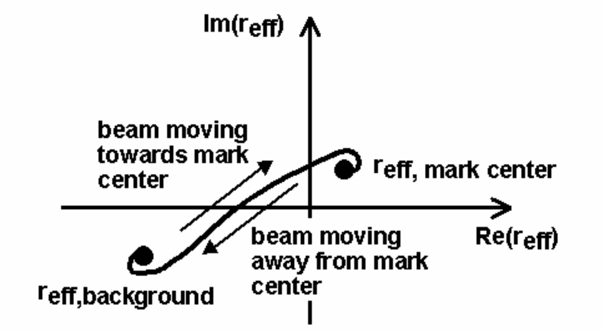

Figure 73. Mark-scan diagram representing the movement of the value of the effective reflectance on the complex plane when a data mark is scanned with the laser.

The background value and the mark-center value of the effective reflectance can be written in a functional form using Babinet's principle. In Figure 74, the optical disk's data surface has been divided into the background area and the data-mark area. The data-mark area is co-centered with the readout beam. Now, we can calculate the partial coupling coefficients for the background area, C_{BG}, and the mark area, C_{mark}, numerically using e.g. the Fourier optics. Applying Babinet's principle, we can write the effective reflectance as the superposition of these partial coupling coefficients multiplied by the corresponding reflectivities, i.e. the reflectivity of the mark-area, r_{mark}, and the reflectivity of the background area r_{BG}. For the mark-center value of the effective reflectance we get:

$$r_{eff,\text{mark center}} = r_{\text{int}} + t_{\text{int}}^2 \left(r_{BG} C_{BG} + r_{mark} C_{mark} \right), \tag{87}$$

and for the background value, setting the reflectivity of the mark area equal to r_{BG}, we get:

$$r_{eff,\mathrm{background}} = r_{\mathrm{int}} + t_{\mathrm{int}}^2 \left(r_{BG} C_{BG} + r_{BG} C_{mark} \right). \tag{88}$$

Note, that

$$r_{eff,\mathrm{mark\ center}} = r_{eff,\mathrm{background}} + t_{\mathrm{int}}^2 \left(r_{mark} - r_{BG} \right) C_{mark} . \tag{89}$$

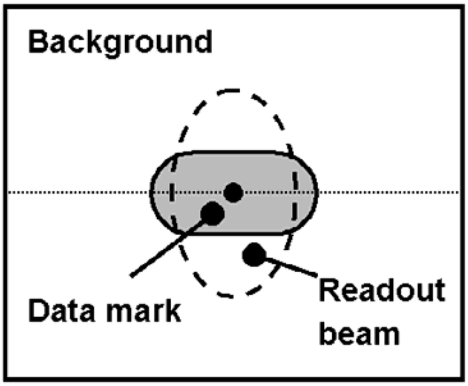

Figure 74. The division of the data surface of the disk into the background area and the mark area for the calculation of the mark-center and the background values for the effective reflectance. The data mark is co-centered with the readout beam.

Figure 75 represents the most important influences of the design parameters on the trajectory on the scan diagram. The mark size (via the coupling coefficient C_{mark}) and the reflectivity difference between the mark and the background ($r_{mark} - r_{BG}$) define the length of the trajectory, i.e. the relative locations of the background reflectivity point and the mark-center reflectivity point on the diagram. Note that here the reflectivity difference takes into account the phase of the reflectivity as well as the amplitude. The largest reflectivity difference between the mark and the background is thus achieved with a unit reflectivity in both the mark area and the background area, but with a phase shift of π between the mark and the background.

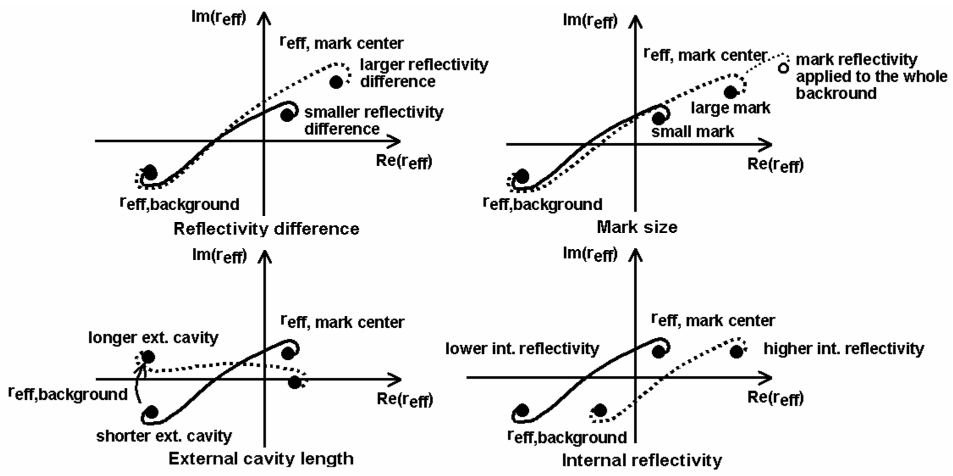

Figure 75. The influence of the various design parameters on the readout signal illustrated using the mark-scan diagrams. The readout signal is roughly proportional to the amplitude of the effective reflectance.

The effective reflectance of the ESEC also depends on the internal reflectance of the laser facet (r_{int}) that adds up with the external reflectance, and the external cavity length that defines the phase of the external reflectance. The change in the amplitude of the internal reflectance moves the reflectance trajectory in the direction defined by the phase of the internal reflectance. Usually the phase of the internal reflectance is either 0 or π. If the amplitude of the internal reflectance is changed, the trajectory in the scan diagram moves in the direction of the real axis. The phase is included in the coupling coefficients C_{mark} and C_{BG}. Taking the phase term out of the coupling coefficients, the effective reflectance can be written in an approximate form: $r_{eff} \approx r_{int} + |r_{ext}|\exp[i\phi_{ER} + i(2\pi/\lambda)\ 2z_{EC}]$. The external cavity length thus affects the phase of the external reflectance and thus rotates the trajectory in the diagram. Large changes in the external cavity length or the internal reflectivity will also affect the scaling (i.e. the length) of the trajectory via the amplitude of the external reflectance $|r_{ext}|$.

To get the largest possible modulation to the signal, one end of the effective reflectance trajectory should be in the origin of the scan diagram. That can be theoretically done by first adjusting the external cavity length so that e.g. the background value of the reflectivity is on the real axis of the diagram. Then the internal reflectivity is changed to move the background value to the origin of the diagram. That will give a signal type similar to the central aperture detection (CAD) used in the conventional optical data storage systems. In CAD, the signal level directly reacts to the reflectivity of the media.

One practical approach to getting a high-modulation CAD signal is to use as low an internal reflectance as possible and design the optical disk so that the background reflectance is as close to zero as possible and the mark reflectance as high as possible (see e.g. [82]). This system is very immune to the changes in the external cavity length, since the interference between the internal and the external reflections is minimal and the amplitude of the external reflectance directly determines the amplitude of the effective reflectance.

Another useful signal type is an edge detection signal, resembling the rectified split detection (RSD) in the conventional data storage systems. In the RSD, the signal level reacts to the change of the reflectivity, i.e. the mark edge region will give higher or lower signal value than either the background or the central area of the mark. The RSD signal can be achieved in the DSLR system by adjusting the external cavity length and the internal reflectivity so that the mid-point of the scan-trajectory goes through the origin. In that case, the background and the mark center will produce the same amplitude for the effective reflectance. Also, a combination of the RSD and the CAD types can be built by fitting the design parameters so that some other part of the scan trajectory than the mid point is at the origin. The scan diagrams for the RSD type edge detection signal and the CAD-signal are shown in Figure 76. Note that in Figure 76, the modulation of the CAD signal is not optimized, i.e. the background reflectivity does not go to zero.

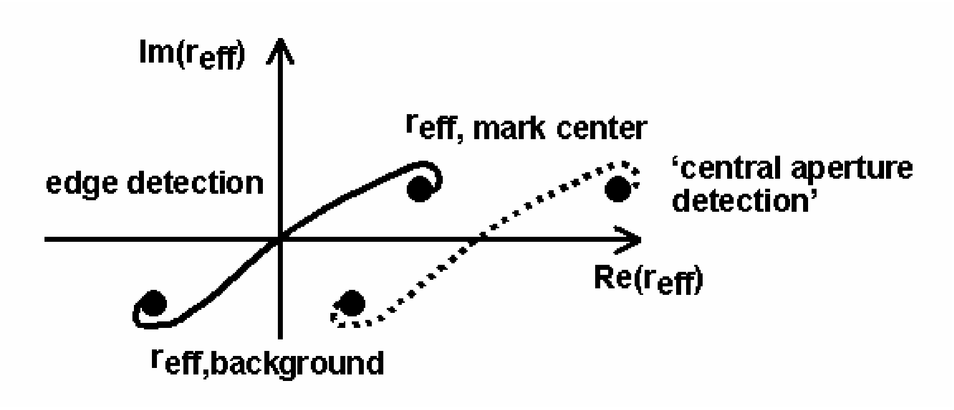

Figure 76. The design of the DSLR for edge detection and central aperture detection signals using the mark-scan diagram.

In Figure 77 we show simulated examples of the various signal types achieved by the change of just one design parameter, the internal reflectance [10]. The simulations were done using the angular spectrum decomposition and applying Babinet's principle as described in Section 4.5.1.1. In these simulations we used an ideal reflectance with unit amplitude and a phase sift of π between the mark and the background. The flying height of the laser (the external cavity length) was half a wavelength and the T (converted to the position on the disk) was approximately one third of the wavelength (λ = 850 nm). The effective reflectances for the marks of the length 3T, 5T, 7T, 9T, and 11T are shown as the function of the scan position. By changing the internal reflectance from R_{int} 0.650 to R_{int} = 0.503 we were able to transform the CAD signal to the RSD signal, these signals are shown in Figure 77a and b, correspondingly. An intermediate reflectance value gives a combined CAD and RSD signal, an example of which is shown in Figure 77 c.

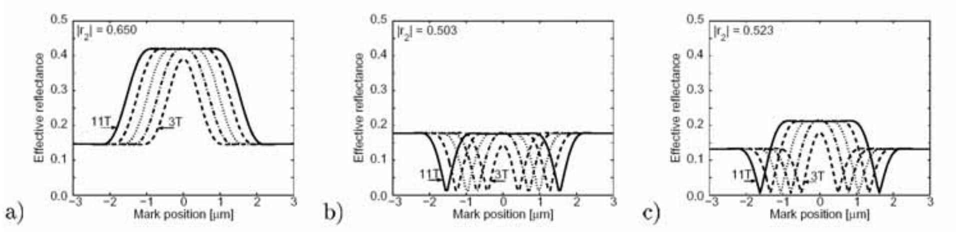

Figure 77. Examples of calculated effective reflectances for different types of DSLR signals; a) CAD signal, b) RSD signal and c) intermediate form. All of these signals are achieved by just changing the internal (laser facet) reflectance.

4.5.1.4 Wavelength tuning enhanced readout

The changes in the effective reflectance will cause changes both in the power and the lasing wavelength. To see if the wavelength tuning effect can be used for enhancing the direct semiconductor laser readout, we made a simulation of the laser's spectral behavior as a data pattern is scanned with the laser. The resulting simulated spectrum is shown in Figure 78 as the function of the position of the data mark. The spectrum shown in the figure is the envelope function of the modal powers. The scanned mark pattern is shown on the lower right side of the image. The mark had a ¾ π phase difference relative to the background. The amplitude of the reflectance was unity. The laser was modeled as a GaAs laser (Laser 3 in Table 1, p. 30) with the internal cavity length 400 µm. Both the back and the front facet reflectances were 0.5 and the driving current was 100 mA. The effective reflectance, shown in Figure 79, was calculated using the angular spectrum decomposition method (but not Babinet's principle because here we wanted to take the rounded shape of the data marks into account) as described in Section 4.5.1.1.

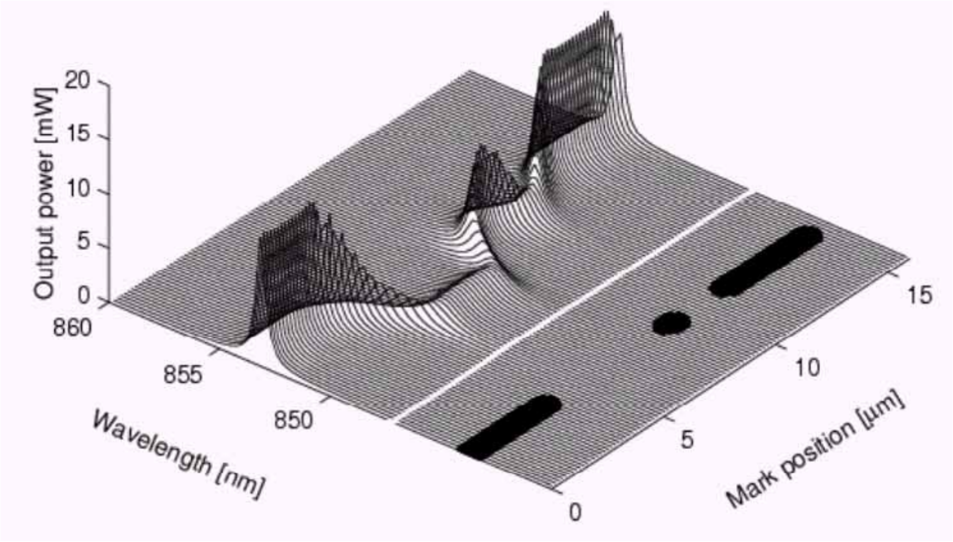

Figure 78. Simulated spectrum of the laser as the function of the mark-scan position in a DSLR configuration. The output power shown in the figure is the envelope function for the modal powers. The scanned data-mark pattern, with a 3/4π phase difference to the background, is shown in the lower right part of the figure.

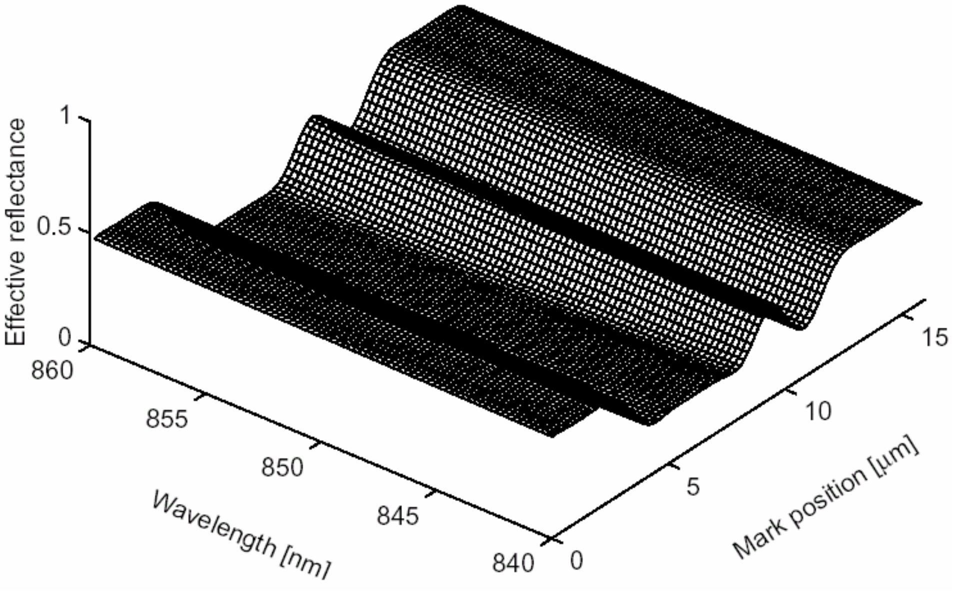

Figure 79. The effective reflectance corresponding to the data-mark-scan shown in Figure 78.

As expected, both the power and the wavelength changes are seen in the simulation as the mark pattern is scanned. The output power of the laser is plotted in Figure 80. The total output power is relatively constant, but the power from the back facet of the laser is clearly modulated by the data mark pattern. Figure 81 shows the principal lasing wavelength of the laser. The lasing wavelength is shifted by about 3 nm for the longer data marks and about 0.6 nm for the shorter marks.

The wavelength shift enables the use of the technique that we call the wavelength tuning enhanced readout (WTER). WTER can be realized e.g. by the spectral filtering of the light before measuring the optical power. An example of the WTER technique is given in Figure 80 and Figure 81. The third power curve in Figure 80, labeled as WTER, is calculated by applying a high-pass filter with the filter-edge at the wavelength 852.5 nm as shown in Figure 81. By applying the WTER, the modulation of the readout signal (the WTER output power) is considerably strengthened.

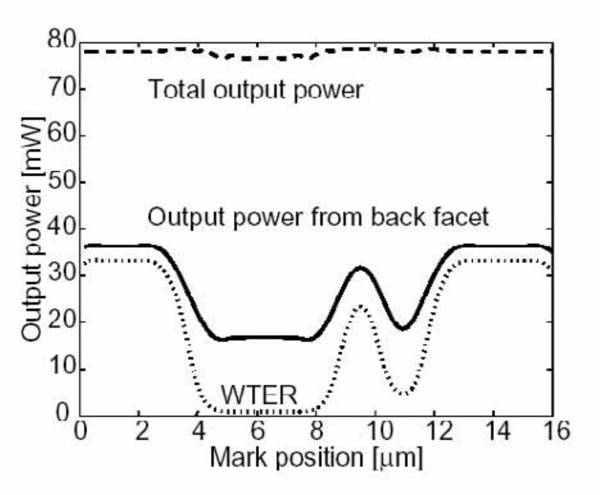

Figure 80. The total optical output power, the output power from the back facet of the laser and the high-pass filtered WTER power as the function of the mark-scan position for the readout in the DSLR configuration corresponding to Figure 78.

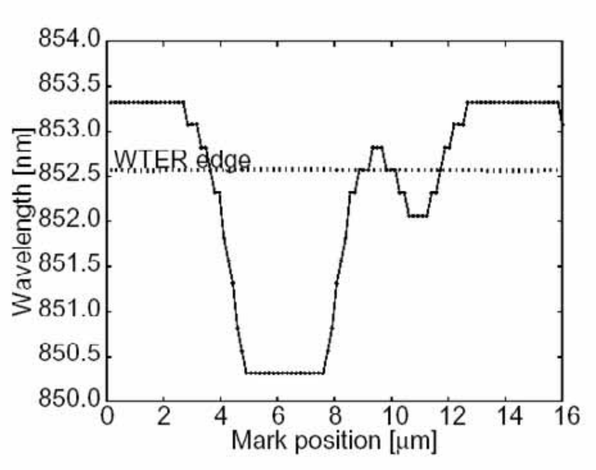

Figure 81. The principal lasing wavelength as the function of the mark-scan position, and the high-pass band edge used in the WTER configuration corresponding to the DSLR system in Figure 78.

4.5.2 Comparison of conventional edge emitting lasers and very small aperture lasers

In this section, we will review the work presented in references [8] and [13].

4.5.2.1 The combined laser-end model

We used a combination of the FDTD and the phenomenological laser model to predict the operation of a direct semiconductor laser read/write system. With the combined model, we calculated the electric fields, the power flow, and the absorption characteristics in/near the extremely short external cavity (ESEC), and also the output power and the optical spectrum of the laser. First, the electromagnetic (EM) fields were calculated with the FDTD in the specified system geometry. The energy flow (the Poynting vector) was calculated from the EM fields, and the absorption density profiles were calculated from the energy flow. The effective reflectance characteristics were extracted from the EM fields as well, as described in Section 3.3.5. The effective reflectance data was inserted into the phenomenological laser model to predict the laser's output power and the operating wavelength.

We used two-dimensional FDTD simulations to reduce the computation time. The model can be expanded to three dimensions without any major changes. Because the actual lasing power was not known when the FDTD code was run, a normalized oscillating EM field source was first used in the FDTD simulations. Thereby, only the absorption power density relative to the power of the normalized EM source was known after the FDTD calculations. After the laser simulation, the output power resulting from the phenomenological laser model was used for re-scaling the EM field strengths to get e.g. the actual absorption power density (see Section 3.2.3).

In the FDTD, the laser geometry was modeled as a simple slab waveguide using only three layers. In the following example, the refractive indices of the waveguide and the cladding were 3.37 and 3.2 respectively. The FDTD simulations were carried on until the steady state was reached. The oscillation wavelength of the laser was set to 1 μm and the width (confining thickness) of the waveguide was also 1 μm. We performed the simulations in 2D space using TM polarized waves. In TM mode, the electric field vector is perpendicular to the calculation grid and three field components exist, namely E_z, H_x and H_y. These assumptions describe the optical fields of an edge-emitting semiconductor laser reasonably well.

The optical disk, functioning as the external reflector, was assumed to be a stacked structure of thin material layers, consisting of a cover glass, a phase change (PC) data layer, and a substrate. The refractive indices of these layers were 1.5, 4.47+1.40i, and 1.5, respectively. The thicknesses of the cover and the PC layers were 100 nm and 20 nm. The substrate extended beyond the calculation boundary, being infinitely long in the simulation point of view. This is a reasonable assumption, because the influence of the reflection from the back surface of the substrate would be insignificant.

A typical ESEC laser geometry used in the FDTD models is shown in Figure 82 (*left*). A small section of the laser waveguide is shown in the left portion of the figure. The waveguide is followed (towards the right) by the airgap and the three material layers of the optical disk. The light is initialized to the zeroth order transverse waveguide mode from the far-left end of the waveguide (see Figure 82). The disk structure and the airgap between the disk and the laser form the external cavity.

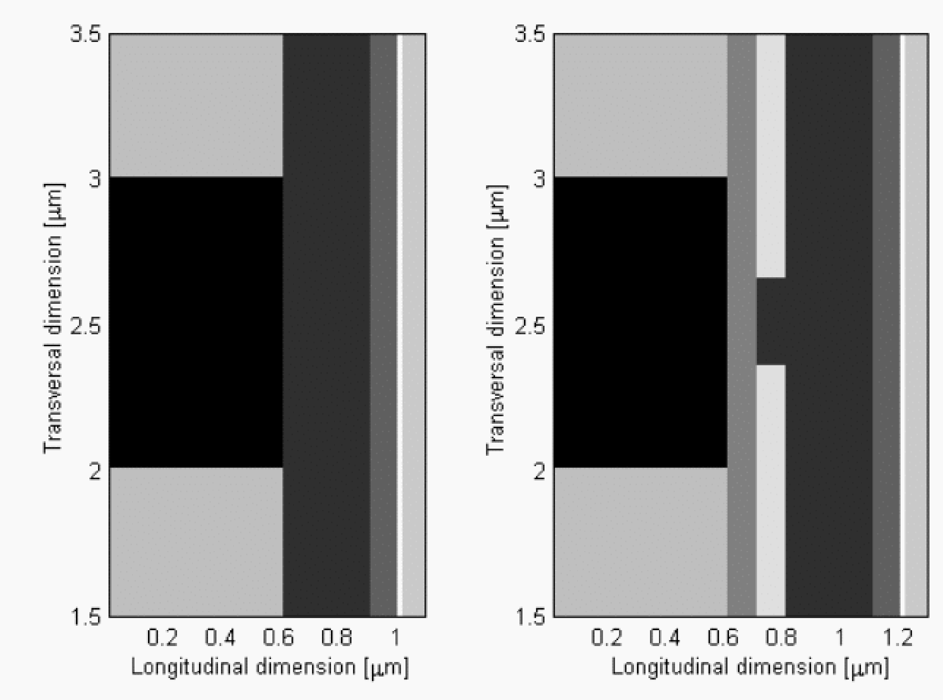

Figure 82. System geometries for the conventional FP-laser end (left) and the VSAL configuration (right). The laser waveguide is shown as the dark part in the center of the left-hand side of both of the figures, confined by the lighter-colored cladding layers. The layers on the right-hand side of each of the figures are (starting from the left) the air gap, the cover layer of the disk, the PC layer, and the substrate. In the VSAL configuration (right) there are two additional layers between the laser waveguide and the airgap: the insulating layer and the metallic layer with the aperture.

4.5.2.2 Comparison of VSAL and conventional edge emitter

We used the laser model to compare the spot sizes and the power variation of a conventional edge emitting laser and a very small aperture laser (VSAL). The model for the conventional laser is shown in Figure 82 (*left*). This geometry was explained in the previous section. Figure 82 (*right*) shows the VSAL configuration. In the VSAL configuration, two layers have been added to the laser geometry, an insulating layer and the metallic aperture. (In the 2D case, the aperture is actually a narrow slit). Both of these added layers are 100 nm thick.

The width of the aperture in the metallic layer is 300 nm. The refractive index of the insulating layer was 1.5 and the metal layer was modeled as a material with a very high permeability, which corresponds well to a good conductor such as aluminum. In the following, we will study how the variations of the ESEC affect the optical characteristics of the two lasers.

The next few figures show some data obtained with the ESEC laser model. Figure 83 (*left*) shows the electric field (E_z) amplitude in the steady state for the conventional edge emitter system. Material boundaries are not shown, but the dimensions are the same as in Figure 82 (*left*). The four peaks with the lower amplitude are located inside the laser cavity and the higher peak is located in the airgap. The minimum of the electric field amplitude (near the 1-µm mark in the longitudinal dimension) is located just before the lossy PC layer. Figure 83 (*right*) shows the electric field amplitude for the VSAL. The scattering due to the aperture (i.e. excitation of the radiative modes) is seen in the waveguide as an irregular shape of the standing wave. The aperture is clearly seen close to the 0.8-micron tick of the longitudinal axis. The electric field amplitude in the external cavity is much smaller in the VSAL system than for the conventional edge emitter.

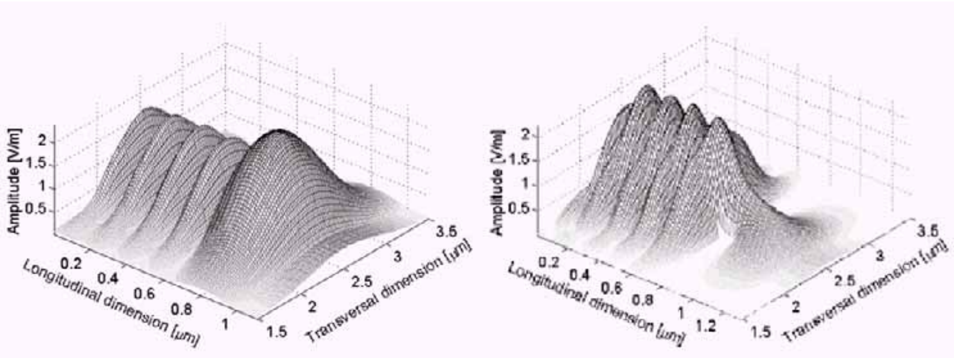

Figure 83. The amplitude of the electric field for the conventional FP-laser (left) and the VSAL (right). (The geometry is shown in Figure 82.)

The energy flow and the absorption distributions are shown in Figure 84 and Figure 85 for the conventional edge emitter system (*left*) and the VSAL system (*right*). Figure 84 shows the magnitude of the energy flow in each of the FDTD grid points (i.e. the modulus of the Poynting vector). If needed, the direction of the energy flow can also be calculated from the data. In Figure 84 (*left*) describing the conventional edge emitter, there is a steep drop in the energy flow at 1 µm in the longitudinal dimension. This is due to the absorption in the PC layer. A similar slope also exists in Figure 84 (*right*) at 1.2 µm, but due to the vertical scale it is not clearly visible.

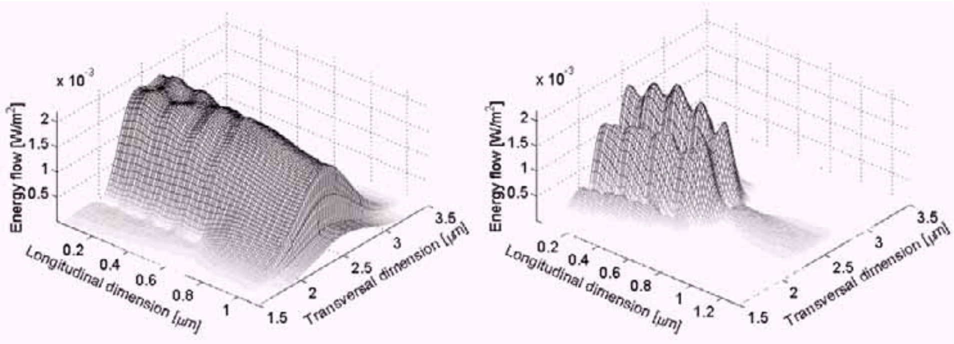

Figure 84. The energy flow (the amplitude of the Poynting vector) for the conventional FP-laser (left) and the VSAL (right). (The geometry is shown in Figure 82.)

The absorption in the phase change layer is shown in detail in Figure 85. Note that the vertical scales for the conventional edge emitting system (*left*) and the VSAL system (*right*) are different, showing that the absorbed power from the VSAL would be an order of magnitude lower than from the conventional laser.

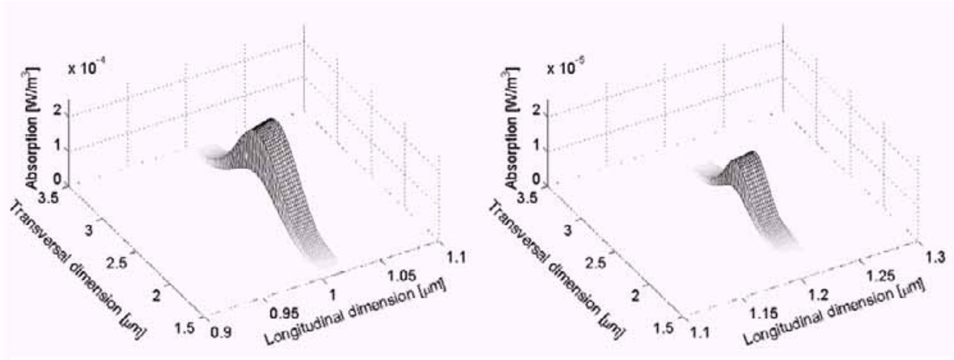

Figure 85. The absorption in the PC-layer for the conventional FP-laser (left) and the VSAL (right). Note the different vertical scales. (The geometry is shown in Figure 82.)

The absorption data allows us to compare the spot size and the absorbed power of the two laser systems. Figure 86 shows the transverse absorption profiles of the conventional (*left*) and the VSAL (*right*) system as a function of the external cavity length. The absorption profiles are taken from the middle of the PC layer. Figure 86 shows a clear spreading of the spot size in both of the systems. For the VSAL system the spot sizes are much smaller at the short ESEC lengths than for the conventional system. Another noticeable feature of these figures is that in both of the systems, there is a maximum in the absorbed power at a certain distance from the front facet of the laser, i.e., at a certain ESEC length. As seen also in Figure 85, the maximum absorption is about one order of magnitude lower in the VSAL configuration than in the conventional system. However, the existence of the maxima can be misleading. In these simulations, the intensity of the initial light within the laser cavity is kept constant. In reality, the laser reacts to the changes in the effective reflectivity. The real system optimization requires full exploitation of the laser's behavior, which will be considered later.

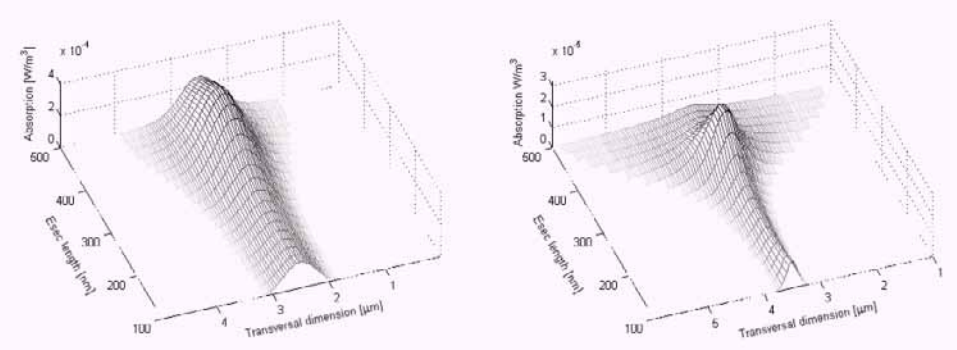

Figure 86. Absorption profiles in the center of the PC layer as the function of the EC length (the airgap thickness) for the conventional FP-laser (left) and the VSAL (right).

In Figure 87, the Full Width Half Maximum (FWHM) spot sizes are compared as a function of the ESEC length. At short ESEC lengths, the spot size in the VSAL system is approximately the same as the metallic aperture size i.e. about one third of the spot size of the conventional system. This can also be noticed in Figure 86. After a short 'collimation region' the spot size of the VSAL starts to increase more rapidly versus the ESEC length than the spot size of the conventional system. At the ESEC length of 400 nm, the spot sizes are equal for both of the systems. Beyond this point, the advantage of the small spot size achieved by the VSAL does not exist anymore.

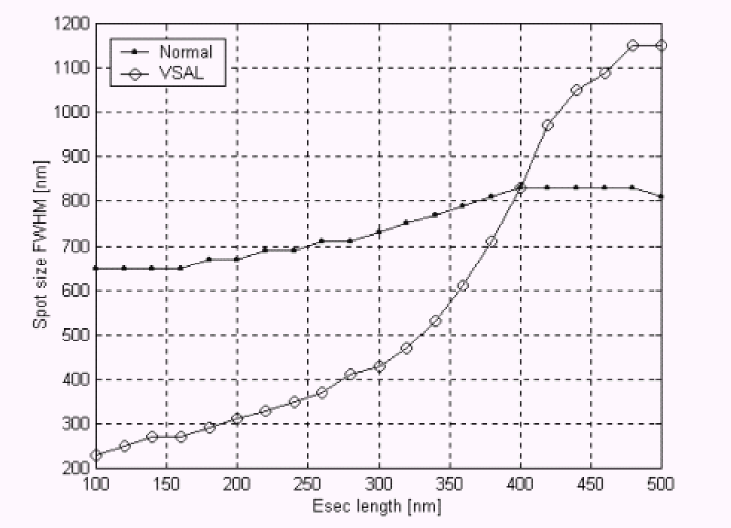

Figure 87. The FWHM spot size calculated from the absorption profiles in the center of the PC layer as the function of the EC length (the airgap thickness) for the conventional FP-laser ('Normal') and the VSAL.

To connect the FDTD simulation to the phenomenological laser model, the effective reflectances of the ESEC must be considered. Figure 88 shows the effective reflectance for both the conventional and the VSAL system as a function of the ESEC length. The amplitude of the effective reflectance affects the power emitted by the laser and the phase determines the longitudinal oscillation modes in the laser cavity. Comparison of the conventional system (*left*) and the VSAL system (*right*) shows that both the amplitude and the phase variation are much smaller in the VSAL system. This can be explained by noting that, in the VSAL system, most of the reflection is due to the metallic aperture and only a very small proportion of the reflection is due to the external reflector. Thereby the variations in the ESEC are hardly seen by the laser. For the conventional edge emitter the amplitudes of the internal and the external reflectivities are close to an equal magnitude.

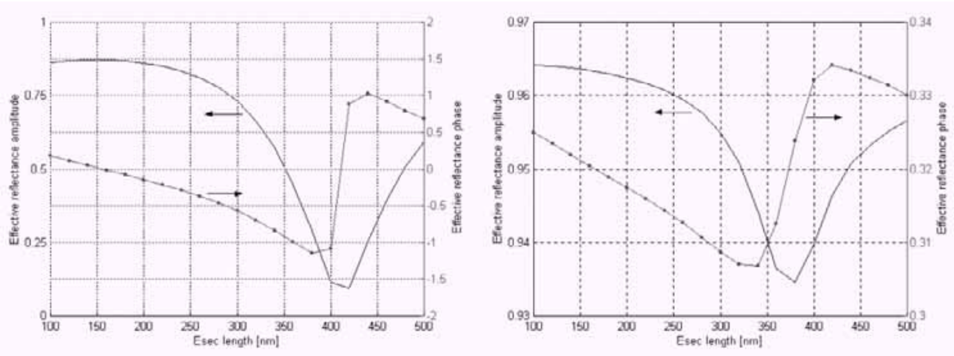

Figure 88. The amplitude and the phase (in radians) of the effective reflectance as the function of the EC length (the airgap thickness) for the conventional FP-laser (left) and the VSAL (right). Note the different vertical scales.

Sometimes it is important to take into account the influence of the ESEC on the optical spectrum emitted by the laser. In such a situation, the wavelength dependence of the effective reflectance must be calculated. Figure 89 shows the effective reflectance as a function of the wavelength for the conventional edge emitter system with a 300-nm ESEC length. The figure indicates some wavelength dependency in the effective reflectivity. This wavelength dependency increases as the ESEC length increases, and it is the origin of the wavelength tuning effects in the ESEC lasers.

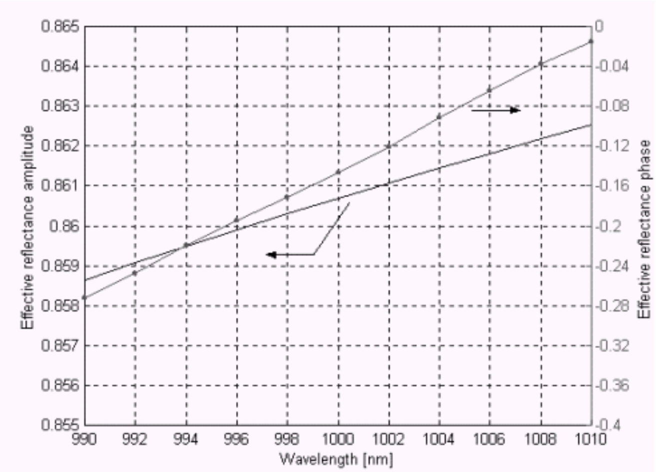

Figure 89. The effective reflectance spectrum for the conventional FP-laser.

Now let us see how the effective reflectance affects the laser's performance. The optical output powers of the two laser configurations as a function of the ESEC length are shown in Figure 90. In addition to the total optical power emitted by the laser, Figure 90 also shows its constituents. As shown in Section 3.2.3, the total optical power is a sum of the power radiated through the back facet of the laser (the back facet is the laser facet not facing the ESEC), the power absorbed to the optical disc, and the power scattered away in the ESEC. The playback signal in the direct semiconductor laser readout is often acquired by monitoring the power radiated through the back facet of the laser. In this simulation, the driving current and other laser parameters are kept constant.

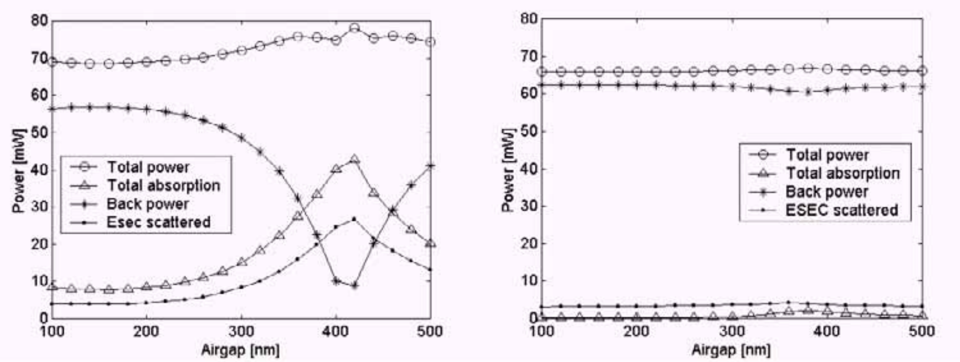

Figure 90. The components of the optical output power as the function of the EC length (the airgap thickness) for the conventional FP-laser (left) and the VSAL (right). The total optical power equals the sum of the powers a) radiating through the back facet of the laser ('Back power'), b) absorbed by the optical disk structure ('Total absorption') and c) scattered away from the system in the ESEC ('ESEC scattered').

An interesting feature in the laser behavior is that the laser power increases when the effective reflectance decreases. This is seen, for example, by comparing the power and the reflectance values (see Figure 88) of the VSAL with those of the conventional edge emitter. This behavior can be explained by considering the balance between the mirror losses and the internal losses in the laser cavity. The behavior suggests very high internal losses in the laser. The reduction of the cavity mirror reflectance allows the light to come out of the laser cavity before it is absorbed due to the internal losses (cf. Section 4.1.1.1). Thereby the total optical output power increases when the reflectance decreases.

The ESEC length giving the absorption maximum (and the reflectivity minimum) is different in the two cases. One reason for this is that the airgap in the conventional system is measured from the front facet of the laser to the cover glass, and in the VSAL system, from the metal surface to the cover glass. That means that in the VSAL system, there is an additional insulating layer and the metal aperture layer inside the external cavity, which increase the actual cavity length. The lasing power simulations shown in Figure 90 have been done without taking into account the wavelength dependency of the effective reflectance. To obtain more accurate output power and wavelength data, the FDTD simulations that yield the effective reflectance terms should be performed with several wavelengths.

The variation of the back facet power versus the ESEC length in the VSAL system is much smaller than in the conventional edge emitter. Also, nominally, the absorbed power varies more in the conventional system, but the relative change in the absorption is on the same order in both of the systems, as can also be deduced from Figure 86. Although in this case the resulting absorption behavior resembles that shown by the absorption curves in Figure 86, this is not always true. For a somewhat different laser configuration, the laser power could have dropped drastically due to the decreasing effective reflectivity in the conventional system. Instead of the absorption maximum at around 400-nm ESEC length, we could have had a minimum as well. The simple absorption analysis shown in Figure 86 is not enough.

This concludes the analysis of the DSLR systems and, simultaneously, the examples of the use of the ESEC lasers. In this Section we have presented theoretical discussion on enhancing the performance of the DSLR systems. We showed a way to design the DSLR for various types of read-out signals. We introduced the wavelength tuning enhanced readout and showed examples of the advanced modeling of the DSLR systems by comparing the performance of the conventional ESEC configuration and a VSAL system.

5. Summary

In this thesis, we have developed ways to model and use extremely short external cavity (ESEC) lasers. A brief overview was presented on the physics related to the semiconductor lasers. A simple phenomenological laser model was developed for efficient calculation of the multi-mode output spectrum of a Fabry–Perot semiconductor laser. The phenomenological model was used to predict the oscillating wavelength and the optical output power of ESEC lasers. Measured gain spectrum of the laser was used in the modeling. The effective reflectance model was used to simulate the influence of the ESEC on the laser operation.

Several ways to calculate the effective reflectance from various kinds of ESEC structures were presented and used. These included the Gaussian beam method, the Fourier optics methods, and the finite-difference time-domain (FDTD) method. Babinet's principle and the Fourier-space methods were introduced for use in the calculation of the coupling coefficients needed in the effective reflectance calculation. A novel laser-end model was presented for calculation of the effective reflectance using the FDTD modeling. This method is applicable for complex laser-end structures and the ESEC structures and enables the detailed analysis of the optical fields in the ESEC.

An overview of the ESEC laser sensors and other devices was given providing a general picture of the possibilities for the use of various ESEC configurations. Several devices based on the ESEC laser configuration were analyzed by modeling and experiments. The wavelength tuning and the optical power characteristics of the planar-mirror (PM) ESEC laser were analyzed and compared to the measurements. Three tuning regions as the function of the external cavity length were introduced. The influence of the different design parameters for the tuning range was studied by modeling.

The wavelength tuning of a laser using a micromachined tunable Fabry–Perot etalon in the ESEC configuration was analyzed. Two tuning methods, 'conventional mirror tuning' and 'rapid tuning' were introduced and the tuning characteristics were analyzed for different design parameters.

A method of wavelength tuning profilometry using the ESEC laser configuration was introduced. The proof-of-principle experiments were done, and the results were explained by using a scalar FDTD model of the optical fields close to the surface.

The direct semiconductor laser readout systems for the optical data storage were analyzed via modeling. The basic relations between the various design parameters and the playback signal were presented in the simple form of a ‘scan diagram’ of the effective reflectance. Based on this analysis, different types of playback signals were constructed. A wavelength tuning enhanced readout method was introduced for use in the direct semiconductor laser readout systems.

Finally, the performance of a conventional Fabry–Perot laser and a very small aperture laser in the direct semiconductor laser readout system were modeled and compared using the novel FDTD laser-end model. Absorption of the light into the data layer of a customized optical disk structure was modeled to estimate the mark sizes and the absorbed power as the function of the cavity length. Power changes in the laser due to the changing feedback were included in the analysis.

References

1. Eliseev, P. G., Ismailov, I., Fedorov, Yu. F. Injection lasers for multichannel optical communication. IEEE Journal of Quantum Electronics, v. QE-6. 1970. Pp. 38–41.

2. Bogatov, A. P., Eliseev, P. G., Ivanov, L. P., Logginov, A. S., Manko, M. A., Senatorov, K.Ya. Study of the single-mode injection laser. IEEE Journal of Quantum Electronics, v. 9. 1973. Pp. 392–394.

3. Voumard, C., Salathe, R., Weber, H. Resonance amplifier model describing diode lasers coupled to short external resonators. Applied Physics, v. 12. 1977. Pp. 369–378.

4. Velichanskii, V. L., Zibrov, A. S., Nikitin, V. V., Sautenkov, V. A., Malyshev, V. K., Kharisov, G. G. Semiconductor laser with ^{133}Cs vapor external selective mirror. Soviet Journal of Quantum Electronics (English translation of Kvantovaya Elektronika), v. 8. 1978. Pp. 836–839.

5. Lang, R., Kobayashi, K., External optical feedback effects on semiconductor injection laser properties. IEEE Journal of Quantum Electronics, v. QE-16. 1980. Pp. 347–355.

6. Tkach, R. W., Chraplyvy, A. R. Regimes of feedback effects in 1.5 μm distributed feedback lasers. Journal of Lightwave Technology, v. LT-4. 1986. Pp. 1655–1661.

7. Aikio, J. K., Kataja, K. J., Alajoki, T., Karioja, P., Howe, D. G. Extremely short external cavity lasers: The use of wavelength tuning effects in near field sensing. Proceedings of SPIE – The International Society for Optical Engineering, v. 4640. 2002. Pp. 235–245.

8. Aikio, J. K., Kataja, K. J., Olkkonen, J., Howe, D. G. Two dimensional FDTD modeling of direct semiconductor laser read/write systems. Proceedings of SPIE – The International Society for Optical Engineering, v. 4647. 2002. Pp. 43–51.

9. Aikio, J., Howe, D. Extremely short external cavity semiconductor laser: Profilometry via wavelength tuning. Conference on Lasers and Electro-Optics Europe – Technical Digest. 2001. Pp. 484–485.

10. Aikio, J., Howe, D. G. Direct semiconductor laser readout in optical data storage. Proceedings of SPIE – The International Society for Optical Engineering, v. 4090. 2000. Pp. 56–65.

11. Aikio, J., Karioja, P. Wavelength tuning of a laser diode by using a micromechanical Fabry–Perot interferometer. IEEE Photonics Technology Letters, v. 11. 1999. Pp. 1220–1222.

12. Aikio, J., Sidorin, Y., Blomberg, M., Karioja, P. Wavelength tunable hybrid laser diode realized by using an electrostatically tuned silicon micromachined Fabry–Perot interferometer. Proceedings of SPIE – The International Society for Optical Engineering, v. 3625. 1999. Pp. 588–597.

13. Aikio, J. K., Kataja, K. J., Howe, D. G. Extremely short external cavity lasers: Direct semiconductor laser readout modeling by using finite difference time domain calculations. Proceedings of SPIE – The International Society for Optical Engineering, v. 4595. 2001. Pp. 163–173.

14. Heikkinen, V., Aikio, J., Alajoki, T., Hiltunen, J., Mattila, A.-J., Ollila, J., Karioja, P. Single-mode tuning of a 1540-nm diode laser using a Fabry–Perot interferometer. IEEE Photonics Technology Letters, Accepted for publication. 2004.

15. Kataja, K., Aikio, J., Howe, D. G. Numerical study of near-field writing on a phase-change optical disk, Applied optics, v. 41. 2002. Pp. 4181–4187.

16. Wartak, M. S., Weetman, P., Alajoki, T., Aikio, J., Heikkinen, V. Extraction of rate-equation parameters from optical modal gain measurements for multiple-quantum-well semiconductor lasers. Microwave and Optical Technology Letters, v. 35. 2002. Pp. 55–56.

17. Coldren, L. A., Corzine S. W. Diode lasers and Photonic Integrated Circuits. John Wiley & Sons, New York, 1995.

18. Svelto, O. Principles of Lasers. Plenum Press, New York and London 1998.

19. Chuang, S.L. Physics of Optoelectronic Devices. Wiley-Interscience, New York, 1995.

20. Ahn, D. Optical gain of a quantum-well laser with non-Markovian relaxation and many-body effects. IEEE Journal of Quantum Electronics, v. 32. 1996. Pp. 960–965.

21. Hakki, B. W, Paoli, T. L Gain spectra in GaAs double-heterostructure injection lasers. Journal of Applied Physics, v. 46. 1975. Pp. 1299–1306.

22. Tsukada, T. GaAs-$Ga_{1-X}Al_XAs$ buried-heterostructure injection lasers. Journal of Applied Physics, v. 45. 1974. Pp. 4899–4906.

23. Bogdankevich, O. V., Vasil'ev, B. I., Nasibov, A. S., Obidin, A. Z., Pechenov, A. N., Zverev, M. M. Investigation of the dynamics of emission from “radiating mirror” semiconductor laser with an external resonator. Soviet Journal of Quantum Electronics (English translation of Kvantovaya Elektronika), v. 4. 1974. Pp. 84–85.

24. Darznek, S. A., Zverev, M. M., Ushakhin, V. A. Investigation of a multielement electron-beam-pumped semiconductor laser with an external mirror. Soviet Journal of Quantum Electronics (English translation of Kvantovaya Elektronika), v. 4. 1975. Pp. 1272–1274.

25. Kanada, T., Nawata, K. Injection laser characteristics due to reflected optical power. IEEE Journal of Quantum Electronics, vol. QE-15. 1979. Pp. 559–565.

26. Mitsuhashi, Y., Shimada, J., Mitsutsuka, S. Voltage change across the self-coupled semiconductor laser. IEEE Journal of Quantum Electronics, v. QE-17. 1981. Pp. 1216–1225.

27. Coldren, L. A., Koch, T. L. Analysis and design of coupled-cavity lasers – Part I: Threshold gain analysis and design guidelines. IEEE Journal of Quantum Electronics, v. QE-20. 1984. Pp. 659–670.

28. Coldren, L. A., Koch, T. L. External-cavity laser design. Journal of Lightwave Technology, v. LT-2. 1984. Pp. 1045–1051.

29. Hammer, J. M. Closed form theory of multicavity reflectors and the output power of external cavity diode lasers. IEEE Journal of Quantum Electronics, v. QE-20. 1984. Pp. 1252–1259.

30. Hirota, O., Suematsu, Y. Noise properties of injection lasers due to reflected waves. IEEE Journal of Quantum Electronics, v. QE-15. 1979. Pp. 142–149.

31. Hui, R.-Q., Tao, S.-P. Improved rate equations for external cavity semiconductor lasers. IEEE Journal of Quantum Electronics, v. 25. 1989. Pp. 1580–1584.

32. Hjelme, D. R., Mickelson, A. R., Beausoleil, R. G. Semiconductor laser stabilization by external optical feedback. IEEE Journal of Quantum Electronics, v. 27. 1991. Pp. 352–371.

33. Talvitie, H. External cavity diode lasers and their applications in optical metrology. Thesis for the degree of Doctor of Technology. Helsinki University of Technology, Espoo 1998. ISBN 951-22-4221-4.

34. Mørk, J., Tromborg, B., Mark, J. Chaos in semiconductor laser with optical feedback: Theory and experiment. IEEE Journal of Quantum Electronics, v. 28. 1992. Pp. 93–107.

35. Merimaa, M., Talvitie, H., Laakkonen, P., Kuittinen, M., Tittonen, I., Ikonen, E. Compact external-cavity diode laser with a novel transmission geometry. Optics Communications, v. 174. 2000. Pp. 175–180.

36. Chuang, Z. M., Cohen, D. A., Coldren, L. A. Tuning characteristics of a tunable-single-frequency external-cavity laser. IEEE Journal of Quantum Electronics, v. 26. 1990. Pp. 1200–1205.

37. Tager, A. A., Petermann, K. High-frequency oscillations and self-mode locking in short external cavity laser diodes. IEEE Journal of Quantum Electronics, v. 30. 1994. Pp. 1553–1561.

38. Addy, R. C., Palmer, A. W., Grattan, K. T. V. Effects of external reflector alignment in sensing applications of optical feedback in laser diodes. Journal of Lightwave Technology, v. 14. 1996. Pp. 2672–2676.

39. Mitsuhashi, Y., Shimada, J. Self-coupled optical pickup. Proceedings of SPIE – The International Society for Optical Engineering, v. 382. 1983. Pp. 217–224.

40. Miles, R. O., Dandridge, A., Tveten, A. B., Giallorenzi, T. G. An external cavity diode laser sensor. Journal of Lightwave Technology, v. LT-1. 1983. Pp. 81–93.

41. Wang, W. M., Grattan, K. T. V., Palmer, A. W., Boyle, W. J. O. Self-mixing interference inside a single-mode diode laser for optical sensing applications. Journal of Lightwave Technology, v. 12. 1994. Pp. 1577–1587.

42. Daza, M. R., Tarun, A., Fujita, K., Saloma, C. Temporal coherence behavior of a semiconductor laser under strong optical feedback. Optics Communications, v. 161. 1999. Pp. 123–131.

43. Wills, A. P., Ferguson, A. I., Kane, D. M. External cavity laser diodes with frequency shifted feedback. Optics communications, v. 116. 1995. Pp. 87–93.

44. Champagne, Y. Mailhot, S., McCarthy, N. Numerical procedure for the lateral-mode analysis of broad-area semiconductor lasers with an external cavity. IEEE Journal of Quantum Electronics, v. 31. 1995. Pp. 795–810.

45. Lawrence, J. S., Kane, D. M. Determination of external cavity coupling-coefficient for diode laser with phase-conjugate feedback. Electronics Letters, v. 36. 2000. Pp. 535–537.

46. Henry C. H. Theory of the linewidth of semiconductor lasers. IEEE Journal of Quantum Electronics, v. QE-18. 1982. Pp. 259–264.

47. Heil, T., Fischer, I., Elsässer, W. Influence of amplitude-phase coupling on the dynamics of semiconductor lasers subject to optical feedback. Physical Review A, v. 60. 1999. Pp. 634–641.

48. Sarid, D., Pax, P., Yi, L., Howells, S., Gallagher, M., Chen, T., Elings, V., Bocek, D. Improved atomic force microscope using a laser diode interferometer. Rev. Sci. Instrum., v. 63. 1992. Pp. 3905–3908.

49. van der Ziel, J. P., Mikulyak, R. M. Single-mode operation of 1.3 mm InGaAs/InP buried crescent lasers using a short external optical cavity. IEEE Journal of Quantum Electronics, v. QE-20. 1984. Pp. 223–229.

50. Kim, J.-Y., Hsieh, H. C. An open-resonator model for the analysis of a short external-cavity laser diode and its application to the optical disk head. Journal of Lightwave Technology, v. 10. 1992. Pp. 439–447.

51. Wang, J., Zhang, H., Wu, Q., Zhou, B. Single-mode characteristics of short coupled-cavity semiconductor lasers. IEEE Journal of Quantum Electronics, v. QE-23. 1987. Pp. 1005–1009.

52. Andrekson, P. A., Alping, A. Optoelectronic properties of semiconductor lasers butt-coupled to optical fibers. IEEE Journal of Quantum Electronics, v. 24. 1988. Pp. 2039–2045.

53. Karioja, P., Howe, D. Diode-laser-to-waveguide butt coupling. Applied Optics, v. 35. 1996. Pp. 404–415.

54. Sidorin, Y., Howe, D. Diode-laser-to-waveguide butt coupling: extremely short external cavity. Applied optics, v. 36. 1997. Pp. 4273–4277.

55. Yariv, A. Quantum Electronics. Third Edition. Wiley, New York, 1989.

56. Goodman, J. W. Introduction to Fourier Optics, Second edition. McGraw–Hill, New York, 1996.

57. Taflove, A., Hagness, S. C. Computational Electrodynamics: The Finite-Difference Time-Domain Method. Artech House, Boston, 2000.

58. Golub, G. H., van Loan, C. F. Matrix Computations. The Johns Hopkins University Press, Baltimore, Maryland, 1983.

59. Ikegami, T. Reflectivity of mode at facet and esillation mode in double-heterostructure injection lasers. IEEE Journal of Quantum Electronics, v. QE-8. 1972. Pp. 450–476.

60. Kendall, P. C., Roberts, D. A., Robson, P. N., Adams, M. J., Robertson, M. J. New formula for semiconductor laser facet reflectivity. IEEE Photonics Technology Letters, v. 5. 1993. Pp. 148–150.

61. Herzinger, C. M., Lu, C. C., Chew, C. The semiconductor waveguide facet reflectivity problem, IEEE Journal of Quantum Electronics, v. QE-29.1993. Pp. 2273–2281.

62. Li, M. Y., Li, G. S., Chang-Hasnain, C. J. Top-emitting michromechanical VCSEL with a 31.6-nm tuning range. IEEE Photonics Technology Letters, v. 10. 1998. Pp. 18–20.

63. Ye, S.-Y., Mitsugi, S., Kim, Y.-J., Goto, K. Numerical simulation of readout using optical feedback in the integrated vertical cavity surface emithing laser microprobe head. Japanese Journal of Applied Physics, Part 1: Regular Papers and Short Notes and Review Papers, v. 41. 2002. Pp. 1636–1637.

64. Goto, K., Kim, Y.-J., Mitsugi, S., Suzuki, K., Kurihara, K., Horibe, T. Microoptical two-dimensional devices for the optical memory head of an ultrahigh data transfer rate and density system using a vertical cavity surface emitting laser (VCSEL) array. Japanese Journal of Applied Physics, Part 1: Regular Papers and Short Notes and Review Papers, v. 41. 2002. Pp. 4835–4840.

65. Densmore, A., Jessop, P. A quantum-well waveguide photodetector for high-precision wavelength monitoring about 1.55 μm. IEEE Photonics Technology Letters, v. 11. 1999. Pp. 1653–1655.

66. Baidus, N. V., Salakhutdinov, I. F., Hoekstra, H. J. W. M., Zvonkov, B. N., Nekorkin, S. M., Sychugov, V. A. A compact tunable narrow-band LD based on emission through the substrate and an external abnormal-reflection mirror. IEEE Photonics Technology Letters, v. 13. 2001. Pp. 1155–1157.

67. Kiang, M.-H., Solgaard, O. M., Muller, R. S., Lau, K. Y. Silicon-micromachined micromirrors with integrated high-precision actuators for external-cavity semiconductor lasers. IEEE Photonics Technology Letters, v. 8. 1996. Pp. 95–97.

68. Uenishi, Y., Honma, K., Nagaoka, S. Tunable laser diode using a nickel micromachined external mirror. Electronics Letters, v. 32. 1996. Pp. 1207–1208.

69. Uenishi, Y., Tsugai, M., Mehregany, M. Hybrid-integrated laser-diode micro-external mirror fabricated by (110) silicon micromachining. Electronics Letters, v. 31. 1995. Pp. 965–966.

70. Sidorin, Y., Blomberg, M., Karioja, P. Demonstration of a tunable hybrid laser diode using an electrostatically tunable silicon micromachined Fabry–Perot interferometer device. IEEE Photonics Technology Letters, v. 11. 1999. Pp. 18–20.

71. Sidorin, Y., Howe, D. Butt-coupled laser diode: Wavelength tuning and optical noise. Proceedings of SPIE – The International Society for Optical Engineering, v. 3109. 1997. Pp. 133–141.

72. Sidorin, Y., Howe, D. Some characteristics of an extremely-short-external-cavity laser diode realized by butt coupling a Fabry–Perot laser diode to a single-mode optical fiber. Applied Optics, v. 37. 1998. Pp. 3256–3263.

73. Dandridge, A., Miles, R. O., Giallorenzi, T. G. Diode laser sensor. Electronics Letters, v. 16. 1980. Pp. 948–949.

74. Sarid, D., Iams, D., Weissenberger, V. Compact scanning-force microscope using a laser diode. Optics Letters, v. 13. 1988. Pp. 1057–1059.

75. Ukita, H., Uenishi, Y., Katagiri, Y. Applications of an extremely short strong-feedback configuration of an external-cavity laser diode system fabricated with GaAs-based integration technology. Applied Optics, v. 33. 1994. Pp. 5557–5563.

76. Ukita, H., Uenishi, Y., Tanaka, H. Photomicrodynamic system with a mechanical resonator monolithically integrated with laser diodes on gallium arsenide. Science, v. 260. 1993. Pp. 786–789.

77. Goto, K., Kim, Y.-J., Hasegawa, Y. Experiments of noble optical floppy disk drive using phase change optical medium and quasi-near field optical head. Proceedings of SPIE – The International Society for Optical Engineering, v. 3864. 1999. Pp. 62–64.

78. Goto, K., Sato, T., Mita, S. Proposal of optical floppy disk head and preliminary spacing experiment between lensless head and disk. Japanese Journal of Applied Physics, Part 1: Regular Papers & Short Notes & Review Papers, v. 32. 1993. Pp. 5459–5460.

79. Kim, Y.-J., Hasegawa, Y., Goto, K. Development of a novel optical floppy disk drive using a phase change optical medium and a quasi-near-field optical head. Japanese Journal of Applied Physics, Part 1: Regular Papers and Short Notes and Review Papers, v. 39. 2000. Pp. 929–932.

80. Kim, Y.-J., Tateno, R., Ikura, T., Matsuda, K., Kawai, H., Suzuki, M., Goto, K. Electron cyclotron resonance (ECR) sputtered antireflection coatings on laser facets for optical memory applications. Japanese Journal of Applied Physics, Part 1: Regular Papers & Short Notes & Review Papers, v. 37. 1998. Pp. 2201–2202.

81. Koyama, F., Shinada, S., Goto, Ke., Iga, K. Surface emitting lasers for optical near-field data storage. Proceedings of SPIE – The International Society for Optical Engineering, v. 3899. 1999. Pp. 344–350.

82. Ukita H., Katagiri Y., Fujimoro, S. Supersmall flying optical head for phase change recording media. Applied Optics, v. 28. 1989. Pp. 4360–4365.

83. Ukita, H., Katagiri, Y. Optimum reflectivity design of laser diode facets and recording medium for an integrated flying optical head. Japanese Journal of Applied Physics, Part 1: Regular Papers & Short Notes & Review Papers, v. 32. 1993. Pp. 5292–5300.

84. Ukita, H., Katagiri, Y., Nakada, H. Flying head read/write characteristics using a monolithically integrated laser diode/photodiode at a wavelength of 1.3 um (Invited Paper). Proceedings of SPIE – The International Society for Optical Engineering, v. 1499. 1991. Pp. 248–262.

85. Ukita, H., Nakada, H., Abe, T. Improvement in lasing properties of an integrated flying optical head with a diamond-film-coated slider. Japanese Journal of Applied Physics, Part 1: Regular Papers & Short Notes, v. 31. 1992. Pp. 524–528.

86. Chen, F., Stancil, D. D., Schlesinger, T. E. Aperture shape effect on the performance of very small aperture lasers. Journal of Applied Physics, v. 93. 2003. Pp. 5871–5874.

87. Chen, F., Zhai, J., Stancil, D. D., Schlesinger, T. E. Fabrication of very small aperture laser (VSAL) from a commercial edge emitting laser. Japanese Journal of Applied Physics, Part 1: Regular Papers and Short Notes and Review Papers, v. 40. 2001, Pp. 1794–1795.

88. Partovi, A. Optical near-field aperture storage technique (ONFAST) for high density, high performance data storage applications. Proceedings of SPIE – The International Society for Optical Engineering, v. 3864. 1999. Pp. 352–354.

89. Partovi, A., Peale, D., Murray, C. A., Zydzik, G., Hopkins, L., Yeh, J. H.-J., Wuttig, M., Chichester, R., Dhar, L., Vakhshoori, D., Hobson, W. S., Wynn, J., Lopata, J. Ultrahigh density near-field optical storage. Pacific Rim Conference on Lasers and Electro-Optics, CLEO – Technical Digest. 1996. Pp. 195–196.

90. Partovi, A., Peale, D., Wuttig, M., Murray, C. A., Zydzik, G., Hopkins, L., Baldwin, K., Hobson, W. S., Wynn, J., Lopata, J., Dhar, L., Chichester, R., Yeh, J. H.-J. High-power laser light source for near-field optics and its application to high-density optical data storage. Applied Physics Letters, v. 75. 1999. Pp. 1515–1517.

91. Shi, X., Hesselink, L. Mechanisms for enchancing power throughput from planar nano-apertures for near-field optical data storage. Japanese Journal of Applied Physics, v. 41. 2002. Pp. 1632–1635.

92. Yamada, M., Kawasaki, D., Awabayashi, H., Ahmed, M. Theoretical proposal of an optical detection system using DFB laser with a very small aperture. IEICE Transactions on Electronics, v. E85-C. 2002. Pp. 831–838.

93. Sidorin, Y., Howe, D. Laser-diode wavelength tuning based on butt-coupling into an optical fiber. Optics Letters, v. 22. 1997. Pp. 802–804.

94. McIlroy, P. W. A. Calculation of the mode suppression ratio in Fabry–Perot, DBR, and external cavity lasers. IEEE Journal of Quantum Electronics, v. 26. 1990. Pp. 991–997.

95. Sidorin, Y., Karioja, P., Blomberg, M. Novel tunable laser diode arrangement with a micromachined silicon filter. Optics Communications, v. 164. 1999. Pp. 121–126.

96. Heikkinen, V. Tunable laser module for fibre optic telecommunication. Doctoral thesis. Espoo: VTT Publications 528. 2004. 171 p. + app. 11 p.

97. Blomberg, M., Orpana, M., Lehto, A. Electrically tunable Fabry–Perot interferometer produced by surface micromechanical techniques for use in optical material analysis. US patent #5561523. 1996.

98. Blomberg, M., Torkkeli, A., Lehto, A., Helenelund, C., Viitasalo, M. Electrically tunable micromachined Fabry–Perot interferometer in gas analysis. Physica Scripta T, v. 69. 1997. Pp. 119–121.

99. Huang, W. P., Chu, S. T., Goss, A., Chaudhuri, S. K. A scalar finite-difference time-domain approach to guided-wave optics. IEEE Photonics Technology Letters, v. 3. 1991. Pp. 524–526.

100. Mitsuhashi, Y., Shimada, J., Kogure, S., Sakai, Y. Self-coupled optical pickup (ii) and its application. Proceedings of SPIE – The International Society for Optical Engineering, v. 490. 1984. Pp. 102–109.

Published by

Series title, number and report code of publication

VTT Publications 529
VTT–PUBS–529

Author(s)
Aikio, Janne K.

Title

Extremely short external cavity (ESEC) laser devices
Wavelength tuning and related optical characteristics

Abstract

In this work, we have developed ways to model and use extremely short external cavity (ESEC) semiconductor lasers. We have used modeling and experiments to analyze the wavelength tuning and other related optical characteristics of various ESEC laser devices. A brief overview is given on the physics related to semiconductor lasers. A simple phenomenological laser model is presented for the efficient calculation of the multi-mode output spectrum of a Fabry–Perot semiconductor laser. The effective reflectance model is used to simulate the influence of the ESEC on the laser operation. Several ways to calculate the effective reflectance from various kinds of ESEC structures are presented, including the Gaussian beam method, Fourier optics methods, and finite-difference time-domain (FDTD) method. We give an overview of the ESEC laser devices. The wavelength tuning and optical power characteristics of the planar-mirror (PM) ESEC laser are analyzed and compared to the measurements. The wavelength tuning of a laser using a micromachined tunable Fabry–Perot etalon in the ESEC configuration is analyzed. A method of wavelength tuning profilometry in the ESEC laser configuration is introduced, and the proof-of-principle experiments are presented and analyzed. The direct semiconductor laser readout systems for optical data storage are analyzed via modeling. Various types of playback signals are constructed, and a wavelength tuning enhanced readout method is introduced. The performance of a conventional Fabry–Perot laser and a very small aperture laser (VSAL) in the direct semiconductor laser readout system are modeled and compared using the novel FDTD laser-end model.

Keywords
external cavity lasers, effective reflectance, semiconductor lasers

Activity unit
VTT Electronics, Kaitoväylä 1, P.O.Box 1100, FIN–90571 OULU, Finland

ISBN 951–38–6377–8 (soft back ed.) 951–38–6378–6 (URL:http://www.inf.vtt.fi/pdf/)	Project number

Date May 2004	Language English	Pages 162 p.	Price D

Name of project	Commissioned by
Series title and ISSN VTT Publications 1235–0621 (soft back ed.) 1455–0849 (URL: http://www.vtt.fi/inf/pdf/)	Sold by VTT Information Service P.O.Box 2000, FIN–02044 VTT, Finland Phone internat. +358 9 456 4404 Fax +358 9 456 4374

VTT PUBLICATIONS 529 Extremely short external cavity (ESEC) laser devices

Janne K. Aikio

Extremely short external cavity (ESEC) provides a simple way of controlling the operation point of a semiconductor laser. A change in the external cavity configuration will change the laser's output power and wavelength spectrum as well as the bias voltage. In this work, the ways to model and use extremely short external cavity semiconductor lasers have been developed. Modeling and experiments have been used to analyze the wavelength tuning and other related optical characteristics of various ESEC laser devices. A brief overview is given on the physics related to semiconductor lasers. A simple phenomenological laser model is presented for the efficient calculation of the multi-mode output spectrum of a Fabry-Perot semiconductor laser. The effective reflectance model is used to simulate the influence of the ESEC on the laser operation. Several ways to calculate the effective reflectance from various kinds of ESEC structures are presented, including the Gaussian beam method, Fourier optics methods, and finite-difference time-domain (FDTD) method. An overview of the ESEC laser devices is given. The wavelength tuning and optical power characteristics of the planar-mirror (PM) ESEC laser are analyzed and compared to the measurements. The wavelength tuning of a laser using a micromachined tunable Fabry-Perot etalon in the ESEC configuration is analyzed. A method of wavelength tuning profilometry in the ESEC laser configuration is introduced, and the proof-of-principle experiments are presented and analyzed. The direct semiconductor laser readout systems for optical data storage are analyzed via modeling. Various types of playback signals are constructed, and a wavelength tuning enhanced readout method is introduced. The performance of a conventional Fabry-Perot laser and a very small aperture laser (VSAL) in the direct semiconductor laser readout system are modeled and compared using the novel FDTD laser-end model.

Tätä julkaisua myy	Denna publikation säljs av	This publication is available from
VTT TIETOPALVELU PL 2000 02044 VTT Puh. (09) 456 4404 Faksi (09) 456 4374	VTT INFORMATIONSTJÄNST PB 2000 02044 VTT Tel. (09) 456 4404 Fax (09) 456 4374	VTT INFORMATION SERVICE P.O.Box 2000 FIN–02044 VTT, Finland Phone internat. +358 9 456 4404 Fax +358 9 456 4374

ISBN 951–38–6377–8 (soft back ed.)
ISSN 1235–0621 (soft back ed.)

ISBN 951–38–6378–6 (URL: http://www.vtt.fi/inf/pdf/)
ISSN 1455–0849 (URL: http://www.vtt.fi/inf/pdf/)